



## 저작자표시-비영리-변경금지 2.0 대한민국

이용자는 아래의 조건을 따르는 경우에 한하여 자유롭게

- 이 저작물을 복제, 배포, 전송, 전시, 공연 및 방송할 수 있습니다.

다음과 같은 조건을 따라야 합니다:



저작자표시. 귀하는 원저작자를 표시하여야 합니다.



비영리. 귀하는 이 저작물을 영리 목적으로 이용할 수 없습니다.



변경금지. 귀하는 이 저작물을 개작, 변형 또는 가공할 수 없습니다.

- 귀하는, 이 저작물의 재이용이나 배포의 경우, 이 저작물에 적용된 이용허락조건을 명확하게 나타내어야 합니다.
- 저작권자로부터 별도의 허가를 받으면 이러한 조건들은 적용되지 않습니다.

저작권법에 따른 이용자의 권리는 위의 내용에 의하여 영향을 받지 않습니다.

이것은 [이용허락규약\(Legal Code\)](#)을 이해하기 쉽게 요약한 것입니다.

[Disclaimer](#)

약학박사학위논문

Functional details of the toxin-antitoxin systems  
based on a structural study

구조 연구에 기반한 독소-항독소 시스템의  
기능 연구 결과

2018년 2월

서울대학교 대학원  
약학과 약제과학전공  
강성민



Functional details of the toxin-antitoxin systems  
based on a structural study

구조 연구에 기반한 독소-항독소 시스템의  
기능적 세부사항들

지도교수 이봉진

이 논문을 약학박사 학위 논문으로 제출 함

2018년 2월

서울대학교 대학원  
약학과 약제과학 전공  
강성민

강성민의 박사학위논문을 인준함

2018년 2월

위 원 장

변영로

(인)

부위원장

안희철

(인)

위 원

이봉진

(인)

위 원

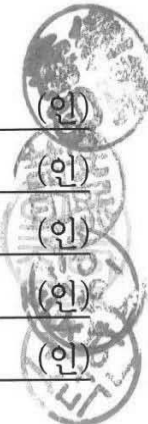
박성진

(인)

위 원

서민덕

(인)





# **Abstract**

## **Functional details of the toxin-antitoxin systems based on a structural study**

**Sung-Min Kang**

**Physical Pharmacy Major**

**College of Pharmacy**

**The Graduate School**

**Seoul National University**

Toxin-antitoxin (TA) systems are essential for bacterial persistence under stressful conditions. In particular, *M. tuberculosis* express VapBC TA genes that encode the stable VapC toxin and the labile VapB antitoxin. Under normal conditions, these proteins interact to form a non-toxic TA complex, but the toxin is activated by release from the antitoxin in response to unfavorable conditions. Here, we present the crystal structure of the *M. tuberculosis* VapBC26 complex and show that the VapC26 toxin contains a pilus retraction protein (PilT) N-terminal (PIN) domain that is essential for ribonuclease activity and that, the VapB26 antitoxin folds into a ribbon-helix-helix DNA-binding motif at the N-terminus. The active site of VapC26 is sterically blocked by the flexible C-terminal region of VapB26. The C-terminal region of free VapB26 adopts an unfolded conformation but forms a helix upon binding to VapC26. The results of RNase activity assays show that  $Mg^{2+}$  and  $Mn^{2+}$  are essential for the ribonuclease activity of VapC26. As shown in the nuclear magnetic resonance (NMR) spectra, several residues of VapB26 participate in the specific binding to the promoter region of the VapBC26 operon. In addition, toxin-mimicking peptides were designed that inhibit TA complex formation and

thereby increase toxin activity, providing a novel approach to the development of new antibiotics

Pneumoniae, an inflammatory human lung disease, is caused by *Streptococcus pneumoniae*, which has received growing attention for its resistance to existing antibiotics. *S. pneumoniae* TIGR4 contains six toxin-antitoxin (TA) pairs of type II TA systems that are essential for bacterial persistence against stressful conditions such as nutrient deprivation, antibiotic treatment, and immune system attacks. In particular, *S.pneumoniae* express HicBA TA gene that encode the stable HicA toxin and labile HicB antitoxin. These proteins interact to form a non-toxic TA complex under normal conditions, but the toxin is activated by release from the antitoxin in response to unfavorable growth conditions. Here, we present the first crystal structure showing entire conformation of the HicBA complex from *S.pneumoniae*, revealing that the HicA toxin contains a double-stranded RNA binding domain (dsRBD) that is essential for RNA recognition, whereas the HicB antitoxin folds into a ribbon-helix-helix (RHH) DNA-binding motif at the C-terminus. The active site of HicA is sterically blocked by the N-terminal region of HicB. According to the RNase activity assays, His36 is essential for the ribonuclease activity of HicA. As shown in the NMR spectra, several residues of HicB participate in the specific binding to the promotor DNA of the HicBA operon. In addition, toxin-mimicking peptide was designed to inhibit TA complex formation and thereby increase toxin activity, providing a novel approach for the development of new antibiotics.

Keywords: toxin-antitoxin system, VapBC, HicBA, NMR, X-ray crystallography

Student number: 2012-21557

# Contents

Abstract.....	iii
Contents.....	v
List of Tables.....	ix
List of Figures.....	x

<b>General Introduction.....</b>	<b>1</b>
----------------------------------	----------

## **Chapter1. Functional details of the *Mycobacterium tuberculosis* VapBC26 toxin-antitoxin system**

1.1 Introduction.....	3
1.2 Experimental procedures.....	6
1.2.1 Cloning and transformation.....	6
1.2.2 Protein expression and purification.....	6
1.2.3 Crystallization, data collection and processing .....	8
1.2.4 Multi-angle light scattering coupled with size exclusion chromatography .....	13
1.2.5 Inductively coupled plasma mass spectrometry.....	13
1.2.6 Isothermal titration calorimetry (ITC) measurements.....	14
1.2.7 Electrophoretic mobility shift assay.....	14
1.2.8 <i>In vitro</i> ribonuclease assay for the addition of metals or peptides mimicking the binding region.....	15
1.2.9 NMR study of full-length VapB26 antitoxin and DNA titration .....	17



## 1.3 Results

1.3.1 Overall structure of the VapBC26 complex.....	19
1.3.2 Structure of the VapC26 toxin.....	23
1.3.3 Structure of the VapB26 antitoxin.....	27
1.3.4 Unique aspects of the formation of the VapBC26 complex.....	29
1.3.5 Characterization of the interaction between VapB26 and promoter DNA .....	35
1.3.6 Metal-dependent ribonuclease activity of VapC26.....	39
1.3.7 Influence of peptides on the RNase activity of VapC26.....	44
1.3.8 DNA-binding site of VapB26.....	50

## 1.4 Discussion.....60

1.4.1 Insights into the unique structure of the VapBC26 complex.....	60
1.4.2 DNA-binding mechanism of VapB26 and the ensuing conformational change .....	61
1.4.3 Mechanism of the <i>in vitro</i> ribonuclease activity of VapC26.....	63
1.4.4 Importance of the VapBC26 system as an antibiotic target.....	65
1.4.5 Artificial toxin activation by inhibition of the TA complex.....	65

## 1.5 Conclusion.....68

## **Chapter2. Functional details of the *Streptococcus pneumonia* HicBA toxin-antitoxin system**

2.1 Introduction.....	70
2.2 Experimental procedures.....	72
2.2.1 Cloning and transformation.....	72
2.2.2 Protein expression and purification.....	74
2.2.3 Crystallization, data collection and processing .....	75
2.2.4 Size exclusion chromatography coupled with multi-angle light scattering	

(SEC-MALS).....	80
2.2.5 Electrophoretic mobility shift assay .....	80
2.2.6 Isothermal titration calorimetry (ITC) measurements.....	81
2.2.7 NMR study on HicB <sup>109-150</sup> and DNA titration.....	81
2.2.8 <i>In silico</i> HicBA-DNA docking.....	82
2.2.9 <i>In vitro</i> ribonuclease assay for the addition of peptide mimicking binding region.....	83
2.2.10 <i>In vivo</i> cell growth assay .....	84
2.2.11 <i>In vivo</i> HicB neutralization assay.....	85
2.2.12 Circular dichroism (CD) spectroscopy.....	85
2.2.13 Antimicrobial activity test.....	85
 2.3 Results	
2.3.1 Overall structure of the HicBA complex.....	87
2.3.2 The structural distinctions of HicB antitoxin.....	92
2.3.3 Characterization of the interaction with promoter DNA.....	95
2.3.4 DNA-binding domain of HicB.....	97
2.3.5 The active site of the HicA and ribonuclease activity dependent on His36.....	103
2.3.6 Intermolecular interactions between HicB and HicA related to toxicity.....	108
2.3.7 Artificial toxin activation and cell growth inhibition by HicA...110	
 2.4 Discussion.....	114
2.4.1 Structural uniqueness of the HicBA complex.....	114
2.4.2 Insights into the DNA binding mechanism of the HicB.....	114
2.4.3 New opinions engaged in active site of HicA.....	116
2.4.4 Artificial activation of the HicA by mimicking peptide as an antibacterial strategy.....	119

2.5 Conclusion.....	120
References.....	121
국문초록.....	139

## List of Tables

**Table 1.** Data-collection and refinement statistics for the SeMet and native structures.

**Table 2.** Primers used for mutation.

**Table 3.** Structural comparisons with many parameters

**Table 4.** Residues used to create mimicking peptides

**Table 5.** Predicted secondary structures with confidence scores offered by Talos based on the backbone-assigned amino acid sequence of VapB26

**Table 6.** Primers used in experiment.

**Table 7.** Data-collection and refinement statistics for SeMet and native structures.

**Table 8.** Residues used to create mimicking peptides

**Table 9.** Predicted secondary structures with confidence scores offered by Talos based on the backbone-assigned amino acid sequence of HicB<sup>109-150</sup>

## List of Figures

Figure 1. Purification and crystallization of VapBC26 from *M. tuberculosis*

Figure 2. Size-exclusion chromatography (SEC)-MALS chromatograms showing the oligomeric states of VapBC26 and VapB26 in solution.

Figure 3. Overall structures of VapBC26 and its subunits.

Figure 4. Diverse point of view and 90° rotated diagrams

Figure 5. Heterodimeric interface between VapB26 and VapC26.

Figure 6. Hydrophobic interface of the VapC26 homodimer.

Figure 7. Overlay of four toxin chains.

Figure 8. Interfaces of the VapB26 dimer. More than 30 residues of each VapB26 N-terminal RHH DNA-binding domain participate in dimerization.

Figure 9. Comparison of the structures of the VapBC complexes.

Figure 10. Sequence alignment of VapC proteins from *M. tuberculosis*, *S. flexneri* and *R. felis*.

Figure 11. Predicted conformation of VapB26-DNA interaction, showing the electrostatic potential surface.

Figure 12. ITC assay and EMSA of VapB26 and the promoter DNA.

Figure 13. ITC assay of VapB26 with control DNA and of VapBC26 with promoter DNA.

Figure 14. *In vitro* ribonuclease activity of *M. tuberculosis* VapC26 and comparison of active sites with homologs.

Figure 15. Purity and structural integrity of VapC26 and ribonuclease activity of *M. tuberculosis* VapBC26.

Figure 16. Ribonuclease activity of *M. tuberculosis* VapC26 measured using a VapC26  $\alpha$ 4-mimicking peptide and experiments using mutants.

Figure 17. Initial test of the RNase activity of *M. tuberculosis* VapBC26 in the presence of toxin-mimicking peptides.

Figure 18. NMR titration of VapB26 and its promoter DNA.

Figure 19. NMR titration experiment of VapB26 and control DNA 'X'.

Figure 20. Schematic representation and surface representation of VapB26 mapped with CSP values (red) and intensity-related values (blue).

Figure 21. Purification and crystallization of HicBA from *S. pneumoniae*

Figure 22. Overall structures of HicBA.

Figure 23. Size-exclusion chromatography (SEC)-MALS chromatograms showing the oligomeric states of HicBA and HicB in solution.

Figure 24. Overall structures of HicBA and HicB.

Figure 25. Secondary structure topologies of *Y. pestis* HicBA and *S. pneumoniae* HicBA.

Figure 26. Structural features of the HicB dimer.

Figure 27. DNA binding properties determined from EMSA and ITC assay.

Figure 28. 2D  $^1\text{H}$ - $^{15}\text{N}$  HSQC spectrum of full-length HicB and DNA titration spectra of HicB<sup>109-150</sup> used to calculate *K<sub>d</sub>*.

Figure 29. NMR titration of HicB<sup>109-150</sup> and its promoter DNA.

Figure 30. Sequence alignment of the *S. pneumoniae* HicA with sequence homologs.

Figure 31. The superposition of HicA homologs.

Figure 32. Active site structure of *S. pneumoniae* HicA and *in vitro* ribonuclease activity assay.

Figure 33. Heterodimeric interface of HicB and HicA, and mutations affecting toxicity.

Figure 34. Several initial tests of peptides.

Figure 35. Ribonuclease activity of *S. pneumoniae* HicBA measured using a HicA  $\alpha$ 2-mimicking peptide and Cell growth inhibition activity of HicA toxin and mimicking peptide.

Figure 36. *In silico* docking model of the HicBA-DNA complex, showing the electrostatic potential surface.

Figure 37. Surfaces of active sites of various toxins.

Figure 38. Catalytic triads of *Y. pestis* HicBA

## General Introduction

There is increasing evidence that TA systems are strongly correlated with bacterial physiology and that they interact with cellular processes involved in gene regulation, growth arrest, survival, and apoptosis (1-5). TA loci were first discovered in 1983 on the mini-F plasmid of *Escherichia coli*, a plasmid addiction module that is responsible for the maintenance of extrachromosomal genetic elements (6). TA systems located on plasmids are transferred to daughter cells and are involved in plasmid stabilization and cell viability (7,8). If the daughter cell primarily inherits plasmids that lack TA genes, it cannot produce antitoxins but still produces residual TA complexes (9). In this situation, a toxin becomes highly activated upon dissociation from the corresponding antitoxin, which is then degraded by cellular proteases, resulting in cell death (10). In contrast, chromosomal TA systems are commonly related to growth arrest, biofilm formation (11) and multidrug tolerance (12,13), all of which facilitate the development of persister or dormant cells (14). These toxins damage host cells by inducing RNA degradation or by binding to topoisomerase to or ribosomes (15-17). In contrast, an antitoxin is an important cellular components for cell maintenance and viability because it neutralizes the detrimental activity of its cognate toxin (18).

TA systems are classified into five groups: type I-V TA systems. In the type I TA system, antitoxins are antisense RNAs that bind to toxins, which are mRNAs. Antitoxins inhibit the translation of toxin and make it be degraded. In the type II TA system, both toxins and antitoxins are proteins that interact with each other to form a non-toxic protein complex. In the type III TA system, antitoxins act as



RNAs that bind directly to toxin protein. They make non-toxic RNA-protein complex. In the type IV TA systems, toxins and antitoxins do not bind directly but they compete to take same cellular target. In the type V TA system, antitoxins are proteins that degrade toxins to be unexpressed (19-23). VapBC and HicBA belongs to type II TA system. In the type II TA system, the toxin is thermodynamically stable, whereas the antitoxin is unstable and cleaved by cellular proteases because of its locally flexible conformation that is susceptible to proteolysis. According to the proteolysis of antitoxin, free toxin is released from TA complex and binds to host cell components. Toxin causes growth arrest or even death of host cell (10,24,25).

# **Chapter 1. Functional details of the *Mycobacterium tuberculosis* VapBC26 toxin-antitoxin system**

## **1. 1 Introduction**

*Mycobacterium tuberculosis* has co-existed with humans for at least 15,000 years (26). This bacterium is aerobic, non-spore forming, non-motile, and may be either gram-negative or gram-positive (27-29). *M. tuberculosis* causes tuberculosis, which claims approximately 2 million lives per year worldwide (30). Notably, multi-drug resistant tuberculosis (MDR-TB) has emerged as a global concern over the past few decades, and approximately 350,000 new MDR-TB cases occur annually worldwide (31). Extensively drug-resistant tuberculosis strains (MDR-TB and XDR-TB, which are resistant to fluoroquinolones and second-line injectables) have been reported in 72% of countries studied (32). Therefore, the development of new antibiotics that can be used to eradicate *M. tuberculosis* by exploiting new therapeutic strategies is urgently needed.

Pathogenic bacteria, such as *M. tuberculosis* utilize many toxin-antitoxin (TA) systems to survive, but non-pathogenic bacteria, such as *Mycobacterium smegmatis*, are reported to use only five TA systems (33). *M. tuberculosis* has a very low growth rate and a long incubation period, whereas *M. smegmatis* is a free-living bacterium that grows rapidly. Thus, the growth, survival and pathogenicity of these bacterial species are closely related to the number of TA loci. Furthermore, TA loci do not exist in humans but specifically exist in bacteria. Therefore, TA systems

represent potential antibiotic targets (34).

Eighty-eight type II TA operons have been identified in *M. tuberculosis*; of these, 45 belong to the VapBC family (35,36). The VapBC TA family is one of the most widely distributed type II TA families throughout bacterial species. However, crystal structures have been determined for only six VapBC TA complexes to date: four from *M. tuberculosis*, Protein Data Bank (PDB) code 3H87 (VapBC3), PDB code 3DBO (VapBC5), PDB code 4CHG (VapBC15), and PDB code 4XGQ (VapBC30) (37-40); one from *Rickettsia felis* (PDB code 3ZVK); and one from *Shigella flexneri* (PDB code 3TND) (41,42). However, the physiological roles of these complexes have not yet been clearly elucidated (38).

VapC toxins commonly contain a PilT N-terminal (PIN) domain that exhibits ribonuclease activity toward cellular mRNAs (43,44). The active sites of VapC toxins consist of three conserved acidic residues that coordinate divalent metal ions such as  $Mg^{2+}$  (45-48), suggesting an acid-base catalysis mechanism for the nucleolytic activity of VapC toxins. VapC26 targets the 23S rRNA in the sarcin-ricin-loop, which is crucial for translation and ribosomal activity (49,50). Only two sarcin-ricin-loop endoribonucleases, VapC20 and VapC26, have been reported in *M. tuberculosis*, (47,49). VapB antitoxins consist of the following two functional motifs: an N-terminal region that binds to the promoter DNA of the TA operon and a C-terminal region that binds to the toxin and thereby abolishes its toxicity (51). The antitoxin alone or in complex with the cognate toxin acts as a repressor that auto-regulates the transcription of the TA operon in a negative feedback loop (52).

Here, we present the crystal structure of the VapBC26 complex from *M. tuberculosis* at a resolution of 2.653 Å. The structure reveals the important residues involved in binding to the promoter DNA and in the formation of the VapBC26 complex. The VapC26 toxin forms an overall  $\alpha/\beta/\alpha$  structure with four parallel  $\beta$  strands, and VapB26 adopts a ribbon-helix-helix (RHH) DNA-binding motif. The core residues in VapB26 that bind to DNA and the structural changes in VapB26 resulting that result from toxin binding were clarified by nuclear magnetic resonance (NMR). The catalytic site of VapC26 is composed of three conserved acidic residues; two of these, Asp4 and Asp97, interact directly with  $Mg^{2+}$ . The ribonuclease activity of VapC26 was confirmed in this study. Several peptides were designed as antibiotic candidates to mimic the binding interface of the VapBC26 complex and thereby suppressing the TA interaction. This approach may contribute to the development of novel, potent antibiotics that can be used to effectively treat antibiotic-resistant *M. tuberculosis*.

## 1.2 Experimental procedure

### 1.2.1 Cloning and transformation

The VapC26 (Rv0582) and VapB26 (Rv0581) genes were amplified by the polymerase chain reaction (PCR). The primers used in PCR were as follows: for VapB26, forward, 5'-G GAA TTC CAT ATG GAC AAG ACG ACG GTC-3'; reverse, 5'-TTA CCG CTC GAG CCG CTC ACC GAA GCC AGC CAG-3'; for VapC26, forward, 5'-G GAA TTC CAT ATG ATC ATC GAC ACG AGT GCG; and reverse, 5'-CCG CTC GAG TTA CGG AAT GAC GGT GAA CGC CCC. DNA was purchased from Bioneer Innovation (Republic of Korea). The restriction enzymes used for cloning were *NdeI* and *XhoI*; the enzyme cutting sites are underlined above. Restriction enzymes were purchased from New England Biolabs (<http://www.neb.com/>). The PCR products of VapB26 and VapC26 were double-cut by *NdeI* and *XhoI* and ligated to vectors that had been cut by the same enzymes. For structure determination and biological assays, VapB26 and VapC26 were ligated to pET21a without a tag and to pET28b, respectively. The pET28b N-terminal tag (MGSSHHHHHHSSGLVPRGSH) was added to VapC26 as an additional residual tag. For NMR experiments, VapB26 was ligated to pET28b resulting in an N-terminal additional residual tag (MGSSHHHHHHSSGLVPRGSH). Each plasmid was then transformed into *E. coli* DH5 $\alpha$  competent cells.

### 1.2.2 Protein expression and purification

For crystallization, the cloned plasmids of VapB26 and VapC26 were co-transformed into *E. coli* Rosetta2 (DE3) pLyss competent cells. The transformed

cells were grown at 37°C in Luria broth (LB) until the OD<sub>600</sub> of the culture reached 0.8. Protein overexpression was induced by the addition of 0.5 mM isopropyl 1-thio-β-D-galactopyranoside (IPTG), and the culture was further incubated at 37°C for 4 h. The cultured cells were harvested by centrifugation at 11,355 x g at 4 °C and stored at -80°C. The harvested cells were then suspended in buffer A (20 mM Tris-HCl, pH 7.9, and 500 mM NaCl) and lysed by ultrasonication. After centrifugation for 1 h at 28,306 x g, the supernatant containing soluble proteins was loaded on a Ni<sup>2+</sup> affinity column (Bio-Rad) equilibrated with buffer A and washed with buffer A containing 100 mM imidazole. The protein bound to the Ni<sup>2+</sup> column was eluted using an imidazole gradient (150–800 mM), and the TA complex present in the elution fractions was identified by sodium dodecyl sulfate polyacrylamide gel electrophoresis (SDS–PAGE). Finally, the buffer in fractions containing the TA complex was exchanged for buffer consisting of 50 mM Tris-HCl, pH 7.9, 500 mM NaCl and 250 mM imidazole using an Amicon Ultra centrifugal filter unit (Millipore), and the sample was concentrated to 5 mg/ml. The purity of the TA complex protein was verified by SDS-PAGE. The VapBC26 complex displaced by selenomethionine (SeMet) (Calbiochem, USA) was expressed and purified by the same procedure except that the cells, containing the complex displaced by SeMet were grown in M9 medium containing extra essential amino acids. Because there are only three methionine residues in the VapB26/VapC26 complex, we mutated Leu50 of VapB26 to Met50 to obtain sufficient phasing power. The primers used for mutation of VapB26 were as follows: forward, 5'–GGCGGGGCCTGGGAGATGGCCAACTGCGGTGCC–3' and reverse, 5'–GGCACCGCAGTTGGCCATCTCCCAGGCCCCGCC–3'. Mutation was conducted using the EZchange™ Site-Directed Mutagenesis Kit

(Enzynomics, Korea) according to the protocol provided by the manufacturer. For NMR experiments, the N-terminal (His)<sub>6</sub>-tagged VapB26 protein was expressed in *E. coli* strain BL21(DE3) using M9 medium containing 1.0 g/l [U-<sup>13</sup>C] glucose and 1.0 g/l [<sup>15</sup>N] NH<sub>4</sub>Cl (Cambridge Isotopes Laboratory) as the sole carbon and nitrogen sources, respectively. The procedure for the initial purification of VapB26 was the same as that used for the TA complex; further purification was conducted by size-exclusion chromatography on a HiLoad 16/60 Superdex 75 preparatory-grade column (GE Healthcare) in a buffer consisting of 20 mM MES, pH 6, and 50 mM NaCl. Expression of VapC26 was difficult because of its toxicity to *E. coli* (53). Therefore, as an alternative method of obtaining the VapC26 protein, limited proteolysis of the VapBC26 complex using pig pepsin protease (Sigma-Aldrich) was performed (54). Pepsin was added to the VapBC26 protein in proportion to its mass, and an adequate number of units which were used in accordance with the manufacturer's instructions. An appropriate amount of pepsin was added to the purified VapBC26, and the mixture was incubated for three hours at 37°C. The proteolyzed VapBC26 was further purified by size-exclusion chromatography on a HiLoad 16/60 Superdex 75 preparatory-grade column (GE Healthcare) under the same buffer condition as used in VapBC26 purification.

### **1.2.3 Crystallization, data collection and processing**

Initial crystal screening of purified VapBC26 complex protein was conducted using the crystal screening 1, 2 and Index 1, 2 kit (Hamton Research) by mixing 1 µl of protein solution at 5 mg/ml in 50 mM Tris-HCl, pH 7.9, 500 mM NaCl and 250 mM Imidazole with 1 µl of reservoir solution. Crystals of the VapBC26 complex were grown using the sitting-drop vapor diffusion method at 4°C. The

crystallization solution for VapBC26 was 25% Tacsimate (pH 7.0). The crystals were directly moved to the liquid nitrogen proton beam because the crystals underwent extensive cracking damage when they came into contact with cryo-protectants containing glycerol. Data were collected using the ADSC Quantum Q270 CCD detector at beamline 7A of the Pohang Light Source, Republic of Korea. Crystals of the VapBC26 complex belong to the *tetragonal* space group P41, with unit cell parameters of  $a = 64.35 \text{ \AA}$ ,  $b = 64.35 \text{ \AA}$ ,  $c = 216.96 \text{ \AA}$ ,  $\alpha = \beta = \gamma = 90.00^\circ$  for the native VapBC26 crystal and  $a = 64.22 \text{ \AA}$ ,  $b = 64.22 \text{ \AA}$ ,  $c = 216.13 \text{ \AA}$ ,  $\alpha = \beta = \gamma = 90.00^\circ$  for the SeMet-labeled VapBC26 crystal. The calculated total mass of the protein complex, including the N-terminal (His)<sub>6</sub> tag, was 24,116.3 Da. All raw data were scaled and processed using the HKL2000 (55). The structure of the VapBC26 complex from *M. tuberculosis* was determined at 2.653 Å resolution by single-wavelength anomalous dispersion using SeMet (2.545 Å for the native complex). Despite the slightly better resolution of the native complex, the structure of the SeMet crystal was as well refined as that of the native complex and the crystallization conditions and the space groups were equal. Therefore, further analysis was conducted using the SeMet data. The Met50 mutation did not affect protein folding. The two structures were almost identical, and the protein-protein interaction patterns were also equal. Detailed statistical information is presented in Table 1. We determined the positions of 12 selenium sites in the total asymmetric unit. First, *PHENIX* (56) was used to automatically build the total residues; the remaining residues were built by *Coot* (57) to provide the final model, which was refined to  $R_{work}$  and  $R_{free}$  (58) of 20.8 and 23.9%, respectively, using *REFMAC* (59). The overall geometry of the structure was validated using *Molprobability* (60); 96.2% of the residues were in the favored region of the Ramachandran plot, and



99.9% were in the allowed region. PyMOL (61) was used to generate all figures. The electrostatic potential surfaces were calculated using Adaptive Poisson-Boltzmann solver (APBS) method (62). Secondary structure analysis was conducted using the 2Struc server (63). The interface area was calculated using the PISA server (64). Sequence alignment was performed using Clustal Omega 1.2.2 (65) and visualized using ESPrpt 3.0 (66). The quality of protein purification and manufactured crystals were described in Figure 1.

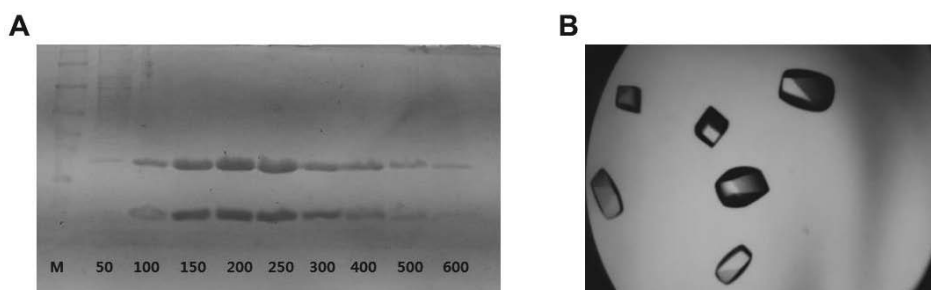


**Figure 1.** Purification and crystallization of VapBC26 from *M. tuberculosis*. **(A)** Column elution using engineered histidine tags. Concentration gradient is plotted at the bottom. **(B)** Generated crystals of VapBC26 from *M. tuberculosis*.

**Table 1.** Data-collection and refinement statistics for the SeMet and native structures.

(a) Data collection details. Values in parentheses are for the highest-resolution shell.

Data set	SeMet	Native
X-ray source	7A beamline of PLS, Korea	7A beamline of PLS, Korea
X-ray wavelength (Å)	0.9794	0.9795
Space group	P4 <sub>1</sub>	P4 <sub>1</sub>
Unit cell parameters		
a, b, c (Å)	64.22, 64.22, 216.13	64.35, 64.35, 216.96
$\alpha$ , $\beta$ , $\gamma$ (°)	90.0, 90.0, 90.0	90.0, 90.0, 90.0
Resolution range (Å)	30-2.65	50-2.55
Molecules per ASU	4 VapBC26 heterodimers	4 VapBC26 heterodimers
Observed reflections ( $>1\sigma$ )	619653	105433
Unique reflections	25229	27340
$\langle I/\sigma(I) \rangle$	70.20 (10.87) <sup>e</sup>	34.98 (3.93) <sup>e</sup>
Completeness (%)	99.8 (100) <sup>e</sup>	94.9 (99.1) <sup>e</sup>
Multiplicity <sup>a</sup>	24.6 (25.4) <sup>e</sup>	3.9 (4.2) <sup>e</sup>
$R_{\text{merge}}$ (%) <sup>b</sup>	11.3 (54.3) <sup>e</sup>	7.8 (67) <sup>e</sup>

(b) Refinement statistics

Data set	SeMet	Native
----------	-------	--------

$R_{\text{work}}^{\text{c}}$ (%)	20.8	22.8
$R_{\text{free}}^{\text{d}}$ (%)	23.9	28.4
No. of atoms / average $B$ factor ( $\text{\AA}^2$ )		
Protein	6170 / 61.0	5978 / 79.8
Water oxygen	65 / 47.9	54 / 83.1
RMSD <sup>f</sup> from ideal geometry		
Bond distance ( $\text{\AA}$ )	0.006	0.007
Bond angle ( $^{\circ}$ )	1.25	1.27
Ramachandran statistics		
Most favoured regions (%)	96.2	95.5
Additional allowed regions (%)	3.7	4.4
Residues in disallowed regions (%)	0.1	0.1
MolProbity score	1.97	1.82
	(98 <sup>th</sup> percentile)	(98 <sup>th</sup> percentile)
PDB accession code	5X3T	

<sup>a</sup>  $N_{\text{obs}}/N_{\text{unique}}$

<sup>b</sup>  $R_{\text{merge}} = \Sigma (I - \langle I \rangle) / \Sigma \langle I \rangle$

<sup>c</sup>  $R_{\text{work}} = \Sigma_{hkl} ||F_{\text{obs}}| - k |F_{\text{calc}}|| / \Sigma_{hkl} |F_{\text{obs}}|$

<sup>d</sup>  $R_{\text{free}}$  was calculated in the same manner as  $R_{\text{work}}$ , but with 5% of the reflections excluded from the refinement.

<sup>e</sup> The values in parentheses indicate the highest resolution shell.

<sup>f</sup> Root mean square deviation (RMSD) was calculated using REFMAC.

#### **1.2.4 Multi-angle light scattering coupled with size exclusion chromatography**

We performed multi-angle light scattering (MALS) to determine the oligomeric states of VapB26 and VapBC26. Size-exclusion chromatography was conducted on a BioSep SEC-s3000 column (Phenomenex) on 1260 Infinity HPLC system (Agilent Technologies). The scattering data were obtained in a miniDAWN-TREOS line for emission at 657.4 nm (Wyatt Technology) and analyzed by ASTRA 6.0.1.10 software (Wyatt Technology). VapB26 and VapBC26 were used at 100  $\mu$ M in the experiment. VapB26 was run in 20 mM MES pH6, and 50 mM NaCl as the condition of NMR spectroscopy, and VapBC26 was run in 50 mM Tris-HCl, pH 7.9, 500 mM NaCl and 250 mM Imidazole, the same conditions as those used for crystallization. All experiments were performed at room temperature.

#### **1.2.5 Inductively coupled plasma mass spectrometry**

Inductively coupled plasma mass spectrometry was conducted to confirm whether  $Mg^{2+}$  co-purified and co-crystallized with the VapBC26 complex. The crystals of VapBC26 used in this measurement were prepared in the same buffer as was used in crystallization (50 mM Tris-HCl, pH 7.9, 500 mM NaCl and 250 mM imidazole). An aliquot of the same buffer was used as a control. ELAN 6100, NexION 350D (Perkin-Elmer, USA) and argon plasma (6,000 K) were used for detection. The radio frequency power was 1,100 W and the sample injection flow rate was 1 ml/min.

### 1.2.6 Isothermal titration calorimetry (ITC) measurements

ITC experiments were performed using a MicroCal 200 (GE Healthcare) at 25°C. The proteins and promoter dsDNAs were prepared in a buffer consisting of 20 mM MES, pH 6 and 50 mM NaCl for VapB26 and in a buffer containing 50 mM Tris-HCl, pH 7.9, 500 mM NaCl and 250 mM Imidazole for VapBC26. The promoter region of VapB26 was selected as [forward – TTCGCGGCTACGCCGACAA; reverse – TTGTCGGCGTAGCCGCGAA], and the annealed dsDNA was purchased from Bioneer Innovation. A control experiment was performed with DNA ‘X’ [forward – GATTTTTTTTGATTTTTTTT; reverse – AAAAAAATCAAAAAAATC], purchased from Bioneer Innovation. DNA ‘X’ was annealed to form double-stranded DNA (dsDNA) by heating to 94°C for 5 min and then cooling to 4°C. Affinity experiments were conducted with the protein solution (10 µM, 320µl) in the cell and the promoter dsDNA solution (600 µM) as the injected titrant. A total of 19 injections made at 150-s intervals were used for data collection. The MicroCal Origin software was used for curve fitting to calculate the binding affinity ( $K_d$ ), the enthalpy of binding ( $\Delta H$ ), the entropy of binding ( $\Delta S$ ) and the stoichiometry ( $n$ ). The raw data were fitted using one-site binding. The Gibbs free energies ( $\Delta G$ ) were calculated using the standard equation  $\Delta G = \Delta H - T\Delta S$ .

### 1.2.7 Electrophoretic mobility shift assay

To distinguish the binding uniqueness of VapB26 and its promoter DNA, electrophoretic mobility shift assays (EMSA) were conducted for the own palindrome promoter sequence of the VapB26 [forward –

TTCGCGGCTACGCCGACAA; reverse –TTGTCGGCGTAGCCGCGAA], and two other palindromic sequences: ‘a’ [forward – TATTTTAATAACTTAAAAGT; reverse – ACTTTTAAGTTATTAAAATA], and ‘b’ [forward – TAATAGAATAATAAGTATCACTCCTTA; reverse – TAAAGGAGTGATACTTATTATTCTATTA]. The DNAs were annealed to form double-stranded DNA (dsDNA) by heating to 94°C for 5 min and then cooling to 4°C. dsDNAs and protein were prepared in a binding buffer pH 6 consisting of 20 mM MES and 50 mM NaCl. Varying amounts of VapB26 protein was mixed with each DNA to give a final volume of 10 µl and incubated for 20 min at 4°C. The samples were loaded onto 0.8% agarose gels in 0.5 x TBE (45 mM Tris-borate, 1 mM EDTA) buffer. The results were visualized using a Printgraph 2M (ATTO).

### **1.2.8 *In vitro* ribonuclease assay for the addition of metals or peptides mimicking the binding region**

We confirmed the ribonuclease activity of VapC26 using an RNase Alert kit (IDT). We conducted the fluorescence quenching assay according to the protocol provided by the manufacturer. In this system, a fluorophore is covalently attached to one end of a synthetic RNA strand and is quenched by a quencher group at the other end of the RNA strand. If synthetic RNA containing a fluorophore-quencher pair interacts with ribonuclease, the synthetic RNA is digested and the quencher is released. The released fluorophore emits fluorescence at 520 nm upon excitation at 490 nm. The resulting fluorescence (RFU) was observed on a SPECTRAmax GEMINI XS spectrofluorometer. Using concentrations of VapC26 and VapBC26 of 2.5 µM, several metals, including  $Mg^{2+}$ ,  $Mn^{2+}$ , and  $Zn^{2+}$  as well as peptides mimicking the

binding region, were examined to determine the influence of metal and peptide binding on the ribonuclease activity of VapC26. We first investigated the metal-dependent ribonuclease activity of VapC26 using  $Mg^{2+}$ ,  $Mn^{2+}$  and  $Zn^{2+}$ . VapC26 was pretreated with 50mM EDTA to remove metals that may have been bound during purification. Its metal binding ability was then regenerated by serial dialysis against a buffer consisting of 50 mM Tris-HCl, pH 7.9, 500 mM NaCl and 250 mM Imidazole. The concentration of metal ions in the buffer was gradually increased to 0.5  $\mu$ M, 5  $\mu$ M, 50  $\mu$ M, 500  $\mu$ M, 5 mM and 50 mM. We also designed seven short peptides that mimic the binding regions of VapB26 and VapC26; two of these mimicked the binding region of VapB26, and the other five peptides mimicked the binding region of VapC26. Theoretically, these peptides should compete with the original protein for binding to the complex (67); if the peptides are bound, the toxin is released from the complex, a process that can be monitored by fluorescence quenching. The peptides used in these experiments were purchased from AnyGen (Korea, [www.anygen.com](http://www.anygen.com)).

For the mutational study of the key binding residues of VapB26 and VapC26, Pro46 and Tyr51 of VapB26 and Leu46 of VapC26 were mutated to alanine and glutamate, to diminish or remove the hydrophobic tendency. The resulting mutant proteins were designated P46A, P46E, Y51A, Y51E, L46A and L46E. Mutation was conducted using the EZchange<sup>TM</sup> Site-Directed Mutagenesis Kit (Enzynomics, Korea) according to the manufacturer's protocol. Mutated VapBC26 complexes were expressed and purified using the same procedures as was used for the native VapBC26 complex and were used in fluorescence quenching assay. The primers used to create these mutations are described in Table 2.

**Table 2.** Primers used for mutation.

Primer	Sequence
P46A-F <sup>a</sup>	5'- GGCGGCGCCAAGCCGCCGGCGCGGGGGTCTATATGCG-3'
P46A-R <sup>b</sup>	5'- CGCATATAGACCCCCGCGCGCCGGCGGGCTTGGCGCCGCC-3'
P46E-F <sup>a</sup>	5'- GGCGGCGCCAAGCCGCCGGAGCGCGGGGGTCTATATGCG-3'
P46E-R <sup>b</sup>	5'- CGCATATAGACCCCCGCGCTCCGGCGGGCTTGGCGCCGCC-3'
Y51A-F <sup>a</sup>	5'- CCGCCGCGCGGGGGTCTAGCTGCGGGTTCGGAGCCCATC-3'
Y51A-R <sup>b</sup>	5'- GATGGGCTCCGAACCCGCAGCTAGACCCCCGCGCGGGCGG-3'
Y51E-F <sup>a</sup>	5'- CCGCCGCGCGGGGGTCTAGAGGCGGGTTCGGAGCCCATC-3'
Y51E-R <sup>b</sup>	5'- GATGGGCTCCGAACCCGCCTCTAGACCCCCGCGCGGGCGG-3'
L46A-F <sup>a</sup>	5'- GTAGCGGAACCTCGACTATGCCGTCGCCACCCGGGTAGGT-3'
L46A-R <sup>b</sup>	5'- ACCTACCCGGGTGGCGACGGCATAGTCGAGTTCCGCTAC-3'
L46E-F <sup>a</sup>	5'- GTAGCGGAACCTCGACTATGAGGTCGCCACCCGGGTAGGT-3'
L46E-R <sup>b</sup>	5'- ACCTACCCGGGTGGCGACCTCATAGTCGAGTTCCGCTAC-3'

<sup>a,b</sup> F and R indicate forward and reverse respectively. Enzyme sites are underlined above.

### 1.2.9 NMR study of full-length VapB26 antitoxin and DNA titration

The NMR spectrum of antitoxin VapB26 was measured on a Bruker AVANCE DRX 800 spectrometer. All the experiments were performed at 25°C. The samples were prepared in a buffer containing 20 mM MES pH 6, and 50 mM NaCl containing 10% (v/v) D<sub>2</sub>O. The data were processed using NMRPipe / nmrDraw (68) and further analyzed by NMRviewJ (69). The data for carbonyl carbon were obtained through spectrum HNCO and HNCACO, and those of  $\alpha/\beta$  carbon were acquired through the spectrum HNCA, HNCOCA, HNCACB and CBCACONH. Additionally, to understand the structural transition that occurs in the specific RHH



domain on VapB26 binding to DNA, a 19-base-pair DNA fragment from the upstream region (promoter DNA) of VapB26 was added to the VapBC26 complex as a palindromic form. The palindromic region of VapB26 was selected as [forward – TTCGCGGCTACGCCGACAA, reverse – TTGTCGGCGTAGCCGCGAA]; the annealed dsDNA was purchased from Bioneer Innovation. DNA titration was conducted three times during the measurement of the HSQC spectrum. The concentration of VapB26 was 0.4 mM in a total of three <sup>1</sup>H, <sup>15</sup>N-HSQC spectra, and the DNA concentration was varied from 0 to a maximum of 0.08mM, which was 20% of the protein concentration. Titration of VapB26 and the control DNA ‘X’ was conducted in the same manner. The intensity of the chemical shift perturbation (CSP) was calculated by nmrViewJ. The average CSP values of <sup>15</sup>N and <sup>1</sup>H were calculated from Equation 1, where  $\Delta\delta_N$  and  $\Delta\delta_H$  represent the CSP values of the amide nitrogen and protons.

$$\Delta\delta_{\text{avg}} = [(0.2 \times \Delta\delta_N^2 + \Delta\delta_H^2) / 2]^{1/2} \quad (1)$$

## 1.3 Results

### 1.3.1 Overall structure of the VapBC26 complex

The crystal structure of the VapBC26 complex from *M. tuberculosis* was determined at a resolution of 2.653 Å. The asymmetric unit of the crystal of the VapBC26 complex contains four VapB26 antitoxins and four VapC26 toxins in a hetero-octameric assembly. The calculated molecular weight of VapBC26 was  $97.5 \pm 1.6$  kDa, which matched the theoretical molecular weight of the hetero-octamer model of VapBC26 (97.0 kDa) (Figure 2). Four of the heterodimeric VapBC26 complexes are included in the asymmetric unit. The VapB26 dimer binds two VapC26 monomers, and two of the VapB<sub>2</sub>C<sub>2</sub> complexes are related to each other by a dyad axis. The flexible hinge loop of the antitoxin wraps the toxin as a hook, known as a looped arm (Figure 3A-D and Supplementary Figure 4).

In the structure of the VapBC26 heterodimer, VapB26 binds to VapC26 via a deep valley formed by four  $\alpha$ -helices ( $\alpha 1$ -  $\alpha 4$ ) of VapC26 (Figure 5). Two C-terminal segments of VapB26, Arg59-Val61 and Phe68-Glu70, adopt turns at the binding interface, and the Asp62, Glu63, and Leu64 residues form a  $3_{10}$ -helix. The long loop between the  $\alpha 2$  and  $\alpha 3$  helices of VapB26 mainly contributes to the binding to VapC26 through hydrophobic interactions (Figure 5) involving the following VapB26 residues: Pro44, Pro46, Tyr51, Ala52, Pro56, Ile57, and Ala58 in a loop between the  $\alpha 2$  and  $\alpha 3$  helices; Val61, Leu64 and Leu65 in the  $\alpha 3$  helix; and Phe68. The following residues in VapC26 are important for binding: Leu9, Ala10, Tyr11, and Phe12 in the  $\alpha 1$  helix; Tyr45, Leu46, Val47, Val51, Ala58, and Val59 in the  $\alpha 3$  and  $\alpha 4$  helices; and Ala15, Pro17, Ile26, Leu33, Ala41, Ala67, Trp68, and Leu115 in the loop between the  $\alpha 4$  and  $\alpha 5$  helices. The aromatic residues may be

involved in the arrangement of the catalytic site of VapC26 and in the formation of the VapB26 and VapC26 dimer (Figure 5). The interfaces of the VapBC26 complex consist of areas of 1,174.1 Å<sup>2</sup> (chains A and B), 1,246 Å<sup>2</sup> (chains C and D), 998.9 Å<sup>2</sup> (chains E and F), and 1,080.1 Å<sup>2</sup> (chains G and H) (64). The interface areas between chains E and F and between chains G and H are relatively underestimated because the electron density of the VapB26 antitoxin (chains E and G) is only shown for Val61.

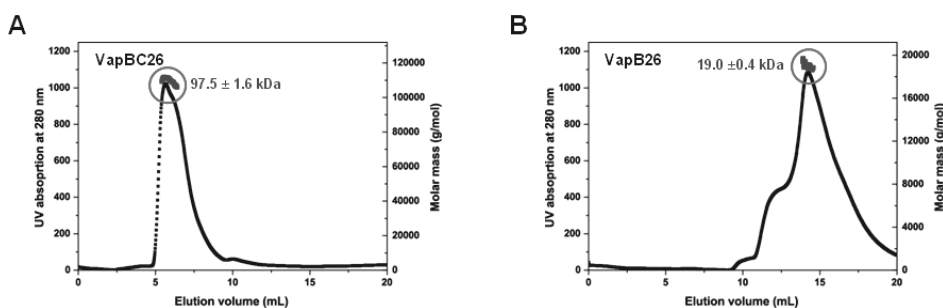


**Figure 2.** Size-exclusion chromatography (SEC)-MALS chromatograms showing the oligomeric states of VapBC26 and VapB26 in solution. **(A)** VapBC26 was anticipated to form a hetero-octamer in solution, similar to its form in the asymmetric unit of the crystal structure. The UV absorption at 280 nm (left axis, black dotted line) and the calculated molecular weight (right axis, blue dotted line) are plotted as a function of the elution volume. The numbers next to the red circled peak indicate the average molecular weight obtained using MALS. **(B)** VapB26 was anticipated to exist as a dimer, similar to its oligomeric form in the VapBC26 complex.

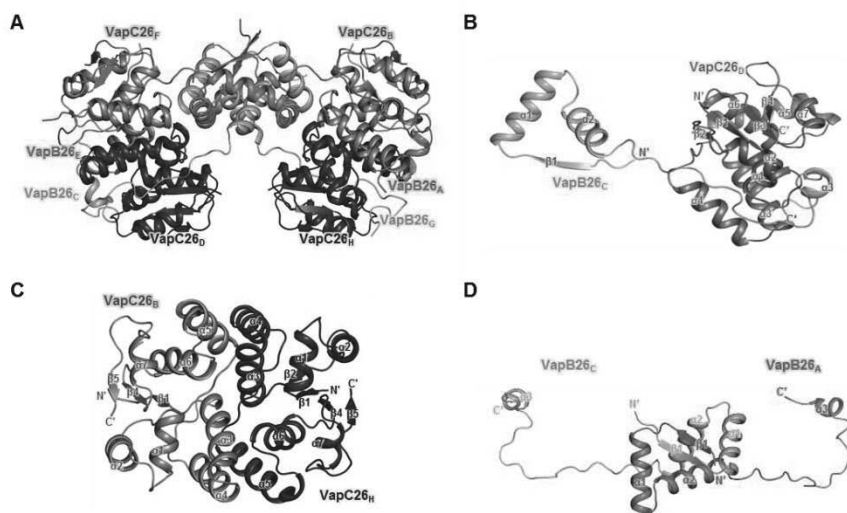


**Figure 3.** Overall structures of VapBC26 and its subunits. **(A)** Ribbon representation of the VapBC26 hetero-octamer. Chains A and E are shown in red and chains C and G of VapB26 are shown in salmon. Chains B and F and chains D and H of VapC26 are shown in slate and blue, respectively. **(B)** Structure of the VapBC26 heterodimer. An arm of VapB26 covers VapC26. **(C and D)** Structure of **(C)** the VapC26 and **(D)** VapB26 dimer detached from the VapBC26 assembly. VapC26 displays cross-contacts between the  $\alpha 5$  helix of one toxin monomer and the  $\alpha 3$  and  $\alpha 4$  helices of another proximal toxin monomer.



**Figure 4.** Diverse point of view and 90° rotated diagrams of (A) VapBC26 heterooctamer, (B) VapC26 dimer, (C) VapB26 dimer, and (D) VapBC26 heterodimer.

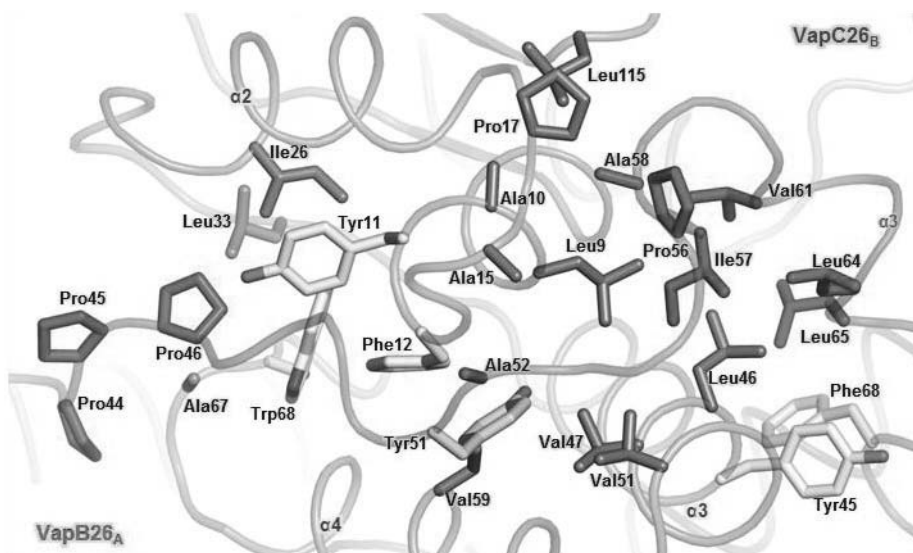


**Figure 5.** Heterodimeric interface between VapB26 and VapC26. **(A)** The residues participating in hydrophobic interactions are shown as stick models. The same colors as those used in **Figure 3** are employed. The aromatic residues that exhibit substantial contributions to the hydrophobic interactions in VapB26 and VapC26 are shown in pink and light green, respectively. The driving force required to generate the heterodimer is derived from hydrophobic interactions.

### 1.3.2 Structure of the VapC26 toxin

The *M. tuberculosis* VapC26 toxin contains seven  $\alpha$ -helices and five  $\beta$ -strands. The structure of the VapC26 toxin adopts an  $\alpha/\beta/\alpha$  sandwich fold composed of five  $\beta$ -strands and seven  $\alpha$ -helices in the following order:  $\beta$ 1 (residues 1–4),  $\alpha$ 1 (residues 5–13),  $\alpha$ 2 (residues 18–27),  $\beta$ 2 (residues 33–36),  $\alpha$ 3 (residues 37–52),  $\alpha$ 4 (residues 54–65),  $\beta$ 3 (residues 68–71),  $\alpha$ 5 (residues 74–92),  $\alpha$ 6 (residues 94–108),  $\beta$ 4 (residues 110–114),  $\alpha$ 7 (residues 116–124), and  $\beta$ 5 (residues 129–134) (Figure

4). Four-stranded parallel  $\beta$ -sheets ( $\beta 2$ - $\beta 1$ - $\beta 4$ - $\beta 5$ ) are surrounded by five  $\alpha$ -helices, with the two remaining  $\alpha$ -helices ( $\alpha 3$  and  $\alpha 4$ ) positioned toward the outside of the structure.

VapC26 forms a homodimer such that the  $\alpha 5$  helix of one monomer contacts the  $\alpha 3$  and  $\alpha 4$  helices of the other proximal monomer and the  $\alpha 3$  helices partially interact with each other in the middle of the interface. This binding is primarily achieved through hydrophobic interactions. Specifically, the Pro37, Tyr38, Val40, and Ala41 residues participate in the  $\alpha 3$ - $\alpha 3$  contact, and the Leu57, Leu60, and Ala64 residues in the  $\alpha 4$  helix interact with Ala75, Ile78, Ala82, and Val85 in the  $\alpha 5$  helix (Figure 6A). Among these residues, Ile78 is a key residue that is required for dimerization of the toxin, as it participates in hydrophobic interactions with Val40, Leu60, Ala64 and Leu70. Ile95 in the  $\alpha 6$  helix is also involved in dimerization, participating in hydrophobic interactions with Val40, Ala41, and Leu60 (Figure 6B). Overall, more than 30 residues are involved in the formation of the dimer (Figure 6A). The interface of the VapC26 homodimer has an average area of 1,085 Å<sup>2</sup> (1,065.1 Å<sup>2</sup> between chains B and H and 1,104.8 Å<sup>2</sup> between chains D and F).

The active site of VapC26 is formed by the  $\beta 1$ - $\alpha 1$  loop,  $\alpha 3$ ,  $\alpha 6$ , the  $\beta 3$  loop and the  $\alpha 7$  loop. The metal coordination site of VapC26 is surrounded by carboxylate oxygen atoms of the following four well-conserved residues: Asp4 (the N-terminus of the  $\alpha 1$  helix), Glu42 ( $\alpha 3$  helix), Asp97 ( $\alpha 6$  helix), and Asp116 ( $\alpha 7$  helix) (Figure 4C). These four acidic residues comprise a negatively charged pocket at the active site (Figure 6D). APBS method (62) was used to calculate the electrostatic surface potential. Among the four VapC26 chains in the asymmetric unit, chain H clearly participates in metal coordination. Heterodimers consisting of chain A-chain B,

chain C-chain D, and chain A-chain C of VapB26 display an electron density map at Glu70. However, for the chain E-chain H heterodimer, chain E only displays an electron density map at Val61. Therefore, due to the lack of a C-terminus in chain E, a spatial constraint is not present in chain H, thus allowing a definite metal ion site to be identified. The presence of metal ions in the VapBC26 complex was confirmed using inductively coupled plasma mass spectrometry (ICP-MS), which showed that 1.73  $\mu\text{M}$   $\text{Mg}^{2+}$  bound to 5.0  $\mu\text{M}$  of VapBC26 complex. The control buffer contained  $\text{Mg}^{2+}$  at less than 0.1 ppb ( $\mu\text{g/kg}$ ). In addition, the ribonuclease activity of VapC26 largely depends on the  $\text{Mg}^{2+}$  concentration. Thus,  $\text{Mg}^{2+}$  is likely coordinated within the active site of VapC26.  $\text{Mg}^{2+}$  coordination may be mediated by hydrogen bonding with the  $\text{O}\delta_1$  atom of Asp4 or Asp97 (Figure 6C). We identified several conserved residues, including Thr5, Ser6, Asn100, and His119, that support the structural integrity of the active site. The  $\text{O}\gamma_1$  atom of Thr5 forms a hydrogen bond with the  $\text{O}\epsilon_2$  atom of Glu42, and the  $\text{O}\gamma$  atom of Ser6 and the  $\text{N}\delta_2$  atom of Asn100 form hydrogen bonds with the  $\text{O}\delta_1$  and  $\text{O}\delta_2$  atoms of Asp4. The  $\text{N}\epsilon_2$  atom of His119 forms a hydrogen bond with the  $\text{O}\delta_2$  atom of Asp97. To illustrate the active site, a figure comparing the active sites of the four toxin chains is included in Figure 7.



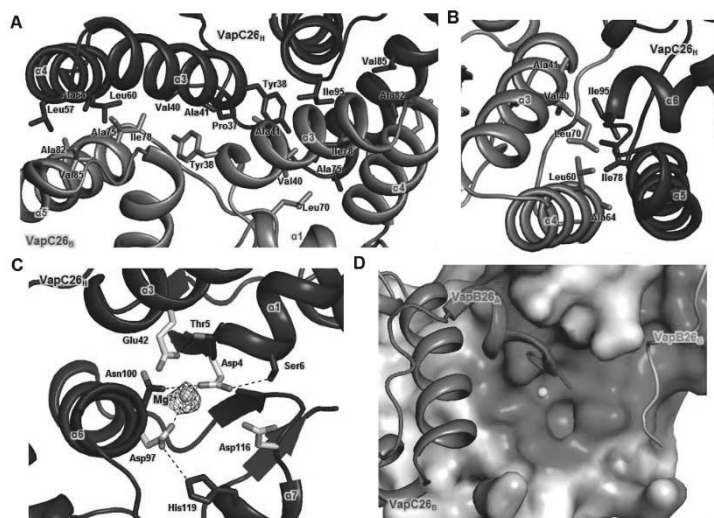


**Figure 6. (A and B)** Hydrophobic interface of the VapC26 homodimer. The residues participating in hydrophobic interactions are shown as stick models. **(A)** Close-up view of the binding interface between two VapC26 monomers. More than 30 residues participate in cross-contacts between the  $\alpha 5$  helix of one toxin monomer and the  $\alpha 3$  and  $\alpha 4$  helices of a neighboring toxin monomer. **(B)** Range of hydrophobic forces from Ile78 and Ile98. **(C and D)** Analysis of the active site.  $Mg^{2+}$  is shown in yellow. **(C)** *Fo-Fc* composite omit map of  $Mg^{2+}$  site contours at  $3\sigma$  [calculated with PHENIX (52)]. Hydrogen bonds are shown as black dotted lines. Asp4, Glu42, Asp97, Asp116 and  $Mg^{2+}$  organize the active site. **(D)** The electrostatic surface potential of VapC26.

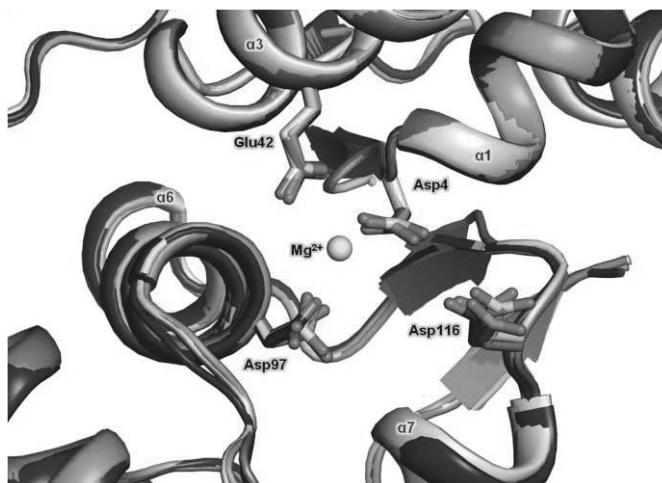


**Figure 7.** Overlay of four toxin chains. The four active sites are composed of the same elements, but  $\text{Mg}^{2+}$  is observed only in chain H.

### 1.3.3 Structure of the VapB26 antitoxin

The *M. tuberculosis* VapB26 antitoxin contains three  $\alpha$ -helices and one  $\beta$ -strand with a topology of  $\beta 1$ - $\alpha 1$ - $\alpha 2$ - $\alpha 3$ . The four secondary structure elements correspond to residues 3–6 ( $\beta 1$ ), residues 10–23 ( $\alpha 1$ ), residues 27–39 ( $\alpha 2$ ), and residues 60–65 ( $\alpha 3$ ) in chain A and residues 4–7 ( $\beta 1$ ), residues 10–23 ( $\alpha 1$ ), residues 27–39 ( $\alpha 2$ ), and residues 60–65 ( $\alpha 3$ ) in chain C. The structure features an N-terminal  $\beta$ -sheet, two adjacent  $\alpha$ -helices and a small C-terminal  $\alpha$ -helix (Figure 4) with a long hinge loop between the  $\alpha 2$  and  $\alpha 3$  helices. Three consecutive prolines (Pro44, Pro45 and Pro46) are located between the  $\alpha 2$  helix and the long loop. Gly24, which is located in the short loop region between the  $\alpha 1$  and  $\alpha 2$  helices, forms a hydrogen bond with nearby residues, thereby creating a turn conformation. The C-terminal  $\alpha 3$  helix is visible in chains A and C but not in chains E or G due to the lack of an electron

density map.

The structure of the VapB26 antitoxin shows a clear electron density map for all residues in chains A and C. According to the analysis of the structure performed using the 2Struc server (63), chain A of VapB26 exhibits the most ordered structure. VapB26 consists of the following two domains: an N-terminal DNA-binding domain and a C-terminal toxin-binding domain.

The two antitoxins interact with each other through their N-terminal  $\beta$ -strands to form a homodimer. The calculated molecular weight of VapB26 is  $19.0 \pm 0.4$  kDa, consistent with the theoretical molecular weight of the VapB26 dimer (19.2 kDa) (Figure 2). The N-terminal domain of the dimer adopts an RHH motif. The average area of the dimeric interfaces is  $1,372.3 \text{ \AA}^2$  ( $1,332.2 \text{ \AA}^2$  between chains E and G; and  $1,412.4 \text{ \AA}^2$  between chains A and C). More than 30 residues of each antitoxin participate in dimerization. The most notable difference between the two antitoxin structures was observed in the N-terminal domain. The N-terminal domains of chains A and C are structurally well ordered, whereas the N-terminal domains of chains E and G are not well folded.

The paired residues on the two  $\beta 1$  strands of the VapB26 dimer, including Asp2-Leu8 and Thr4-Val6, form hydrogen bonds through their backbone atoms (Figure 8A), resulting in the formation of antiparallel  $\beta$ -sheets. The main chain O atom of Tyr7 acts as an acceptor for hydrogen bonding with the  $\text{N}\epsilon$  and  $\text{NH}_2$  atoms of Arg32 in the  $\alpha 2$  helix. Glu11 in the  $\alpha 1$  helix and Arg36 in the  $\alpha 2$  helix play important roles in the cross stabilization between the  $\alpha 1$  and  $\alpha 2$  helices by participating in hydrogen bonds via their side chain NH and  $\text{O}\epsilon$  atoms, which support dimerization (Figure 8B). In addition to the hydrogen bonds, nonpolar residues also contribute to formation of the dimerization interface. Residues in the

$\alpha 2$  helix, including Val30, Ile31, Ile35, and Val39, cross-interact with equivalent residues in the  $\alpha 2$  helix of the proximal antitoxin (Figure 8C). In addition, Ile35 and Val39 play important roles in the interactions with Leu12, Ala15, Val16, and Ala19 in the  $\alpha 1$  helix of the adjacent antitoxin monomer. Ala28, Ile31, and Ile35 provide additional hydrophobic interactions to Val6 in  $\beta 1$ . Leu8 in the  $\beta 1$ - $\alpha 1$  loop also interacts with Ile31 and Ile35 in the antitoxin (Figure 8D).

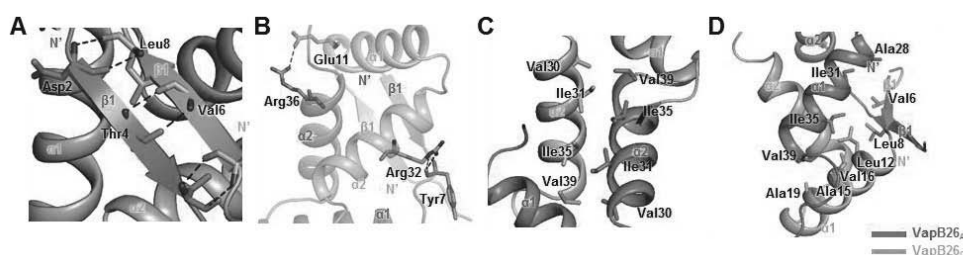


**Figure 8.** Interfaces of the VapB26 dimer. More than 30 residues of each VapB26 N-terminal RHH DNA-binding domain participate in dimerization. Hydrogen bonds are shown as black dotted lines, and residues participating in hydrophobic interactions are shown as stick models. **(A)** Hydrogen bonding networks of antiparallel  $\beta$ -sheets. **(B)** Hydrogen bonds in the  $\alpha 1$  and  $\alpha 2$  helices. **(C)** Hydrophobic interaction in the  $\alpha 2$  helices. **(D)** Range of hydrophobic forces from Ile35, Val39, Val6, and Leu8.

#### 1.3.4 Unique aspects of the formation of the VapBC26 complex

A search for structural homologues of VapBC26 using the DALI server (70) was conducted to analyze their structural similarities, and obvious structural differences between the VapBC26 complex and its structural homologues were observed.

In the structural homologues, the toxin binding region of the antitoxin consists primarily of one or two  $\alpha$ -helices. The antitoxin-binding region of the toxin consists of  $\alpha$ -helices and four antiparallel  $\beta$  sheets. The structures of VapB5, VapB15 and VapB30 include only one  $\alpha$ -helix (VapB30) or two  $\alpha$ -helices (VapB5 and VapB15). VapBs from *R. felis* and *S. flexneri* have one  $\alpha$ -helix ( $\alpha_2$ ) in the toxin-binding region. VapB3 from *M. tuberculosis* displays a complete electron density map at the N-terminus due to the presence of a long  $\alpha$ -helix ( $\alpha_3$ ). However, VapB26 does not contain a specific helix in the binding region, with the exception of a short  $\alpha$ -helix in the C-terminus ( $\alpha_3$ ) of chains A and C. VapB26 forms a flexible hinge loop without any secondary structure at the binding groove, which is formed by the  $\alpha$ -helices of VapC26 (Figure 9A).

Interestingly, VapB26 does not share significant structural similarity with other VapB proteins, with the exception of VapB3 (37). VapB proteins do not share the same DNA-binding domain and the complete structures have only been resolved for a few VapB proteins, which are similar to VapB26. As mentioned above, VapB26 contains an RHH domain in its N-terminal region. The DNA-binding domains of other VapB proteins are normally located in the N-terminal region. However, VapB5, VapB15 and VapB30 from *M. tuberculosis* lack an N-terminal structure. Thus, the structures of the DNA-binding regions of these proteins are not available. The VapB proteins from *R. felis* and *S. flexneri* show clear electron density maps for the DNA-binding domain region. However, these VapB proteins possess a different motif, namely, a  $\beta$ -barrel hairpin. Among the VapB proteins with determined structures, only VapB3 from *M. tuberculosis* shares the same RHH DNA-binding motif as VapB26. Nonetheless, VapBC3 from *M. tuberculosis* does not show the highest structural similarity to VapBC26. Structural similarity is only

observed between antitoxin VapB proteins (Figure 9B).

Like VapB26, VapB3 and FitA (71) contain a RHH DNA-binding motif in their N-terminal domains. For a detailed comparison with VapB26, the structural similarity of VapB3 and FitA was analyzed using DALI (70). The results indicated that VapB3 from *M. tuberculosis* (37) [PDB code 3H87 (chains C and D) with root mean square (r.m.s.) deviations of 5.4 (chain D) and 12.7 (chain C) Å, Z-scores of 4.1-4.2 and a sequence identity of 16%] and the DNA-bound structure of antitoxin FitA from *Neisseria gonorrhoeae* (71) [PDB code 2BSQ and 2H1O (both show chains E, F, G, and H) with r.m.s. deviations of 6.5 (chain G of 2BSQ) and 9.2 (chain F of 2H1O) Å, Z-scores of 4.1-4.2 and sequence identities of 15-17%] had low similarity (Table 3A).

*M. tuberculosis* VapC26 shares structural features similar to a PIN domain motif, as described above. Despite the low level of sequence similarity (16–25%), the secondary structures of VapC proteins resemble one another to a considerable extent (Figure 10). The structural homologues include (i) the VapC30 toxin from *M. tuberculosis* (40) [PDB code 4XGR (chains A, C, E and G) with a r.m.s. deviation of 2.3 Å, Z-scores of 15.8-16.2 and a sequence identity of 22%], (ii) the VapC toxin from *S. flexneri* (42) [PDB code 3TND (chains A, C, E and G) with r.m.s. deviations of 2.4-2.5 Å, Z-scores of 14.2-14.3 and a sequence identity of 16%], (iii) the VapC15 toxin from *M. tuberculosis* (39) [PDB code 4CHG (chains A, B, C, D, E and F) with r.m.s. deviations of 2.4-2.5 Å, Z-scores of 13.7-14.1 and sequence identities of 24-25%], (iv) the VapC toxin from *R. felis* (41) [PDB code 3ZVK (chains A, B, C and D) with r.m.s. deviations of 2.4-2.5 Å, Z-scores of 13.7-14.1 and sequence identity of 16%], (v) the VapC3 toxin from *M. tuberculosis* (37) [PDB code 3H87 (chains A and B) with a r.m.s. deviation of 2.5 Å, Z-scores of

12.1-12.3 and a sequence identity of 18%], and (vi) the VapC5 toxin from *M. tuberculosis* (38) [PDB code 3DBO (chain B) with a r.m.s. deviation of 2.7 Å, a Z-score of 11.3 and a sequence identity of 23%]. Among these VapC structures, VapC3, VapC15 and VapC30 contain Mg<sup>2+</sup>, whereas VapC15 also contains Mn<sup>2+</sup> (Table 3B).

VapC contains not only conserved acidic residues but also other conserved residues that support the active site, as shown in Figure 10. Unlike *S. flexneri* and *R. felis*, each *M. tuberculosis* VapC contains Ser6. However, the Tyr45 of *M. tuberculosis* VapC26 is only conserved in the VapCs of *S. flexneri* and *R. felis*. Other *M. tuberculosis* VapCs have phenylalanine or another amino acid residue at the same position. Phe120 is conserved in every VapC in the figure except the VapC15 of *M. tuberculosis*. In addition, the fourth conserved acidic residue, Asp117, shows slight flexibility, and may be glutamate or aspartate. This flexibility can be applied to Glu54, which does not constitute part of the active site.



**Figure 9.** Comparison of the structures of the VapBC complexes **(A)** and VapB antitoxins **(B)** with their homologues. **(A)** The complete structures of *M. tuberculosis* VapBC3 and VapBC from *R. felis* and *S. flexneri* are shown; other known complexes lack a considerable moiety of the antitoxin. **(B)** VapB from *R. felis* and *S. flexneri* forms a  $\beta$ -barrel hairpin motif. VapB3 from *M. tuberculosis* forms an RHH N-terminal domain similar to that of VapB26, but the toxin-binding domain contains more  $\alpha$ -helices than that of VapB26.



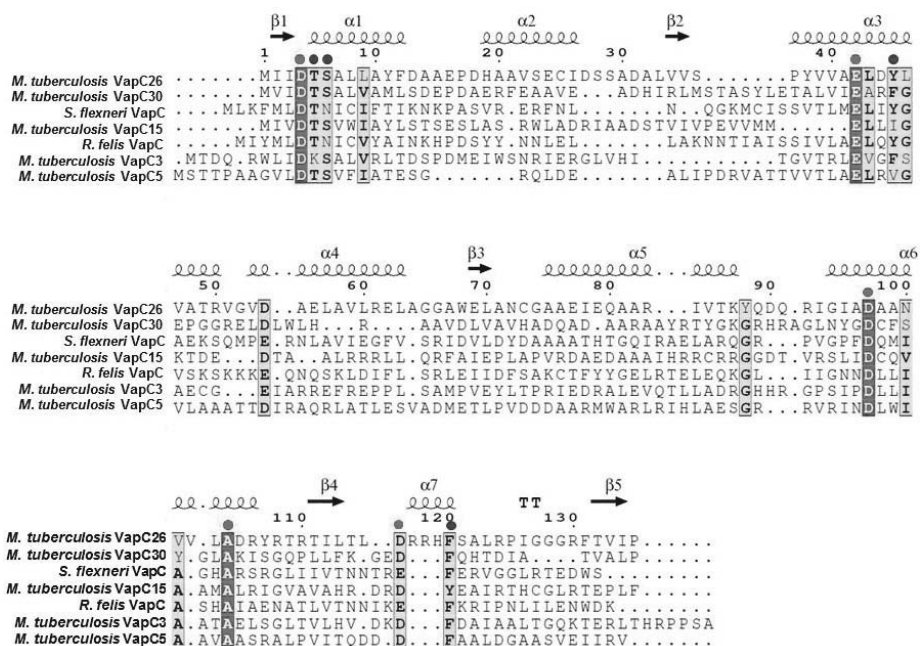


**Figure 10.** Sequence alignment of VapC proteins from *M. tuberculosis*, *S. flexneri* and *R. felis*. The known secondary structure elements of the proteins are shown above the alignment. Identical and similar residues are highlighted in red and yellow, respectively. Conserved residues are indicated by red circles, and the residues participating in the stabilization of active sites are indicated by blue circles. VapC proteins are listed in order of their structural homology with VapC26. The alignments were conducted with ESPript (<http://esprict.ibcp.fr>).

**Table 3.** Structural comparisons with many parameters**A.** Structural homologs of VapB26

Name	PDB code	r.m.s.d	Z- score	Sequence identity
VapB3 ( <i>M. tuberculosis</i> )	3H87	5.4	4.1	16%
FitA ( <i>N. gonorrhoeae</i> )	2BSQ	6.5	4.1	15%

**B.** Structural homologs of VapB26

Name	PDB code	r.m.s.d	Z-score	Sequence identity
VapC30 ( <i>M. tuberculosis</i> )	4XGR	2.3	15.8	22%
VapC ( <i>S. flexneri</i> )	3TND	2.4	14.2	16%
VapC15 ( <i>M. tuberculosis</i> )	4CHG	2.4	13.7	24%
VapC ( <i>R. felis</i> )	3ZVK	2.4	13.7	16%
VapC3 ( <i>M. tuberculosis</i> )	3H87	2.5	12.1	18%
VapC5 ( <i>M. tuberculosis</i> )	3DBO	2.7	11.3	23%

### 1.3.5 Characterization of the interaction between VapB26 and promoter DNA

DNA-binding motifs in proteins are largely categorized into the following four groups: helix-turn-helix (HTH) (72), RHH (73), AbrB-type looped-hinge-helix (74), and the YefM type of three antiparallel  $\beta$ -strands and two helices (75). Structural studies have revealed that VapB26 contains an RHH DNA-binding motif. The functional unit of VapB26 consists of a tight, stable antiparallel  $\beta$ -sheet dimer that binds to DNA. The  $\beta$ -strand and the two subsequent helices (the first and second  $\alpha$ -helices) are the basic components of the RHH superfamily. In the structure of DNA bound CopG, which has RHH domain (PDB code 1B01) (76), the electrostatically

positive portion of the two  $\alpha$ -helices faces the phosphates of the DNA backbone (Figure 11). Antiparallel  $\beta$ -sheet dimer binds to the major groove of the DNA and the two helices anchor the RHH domain to the DNA, allowing the protein to interact optimally with the DNA (73). N-terminus of  $\alpha 2$  contacts with DNA phosphate backbone and the loop between  $\alpha 1$  and  $\alpha 2$  allows the correct positioning of  $\alpha 2$ . VapB26 is predicted to have dimer functional unit as RHH<sub>2</sub> (73).

Isothermal titration calorimetry (ITC) was used to estimate the binding affinity of VapB26 to promoter DNA. As shown in Figure 12A, the binding titration curve displays a typical hyperbolic form. The promoter DNA-binding reaction of VapB26 is exothermic and enthalpically driven, with thermodynamic parameters of  $-51.8 \pm 6.3 \text{ kcal mol}^{-1}$  ( $\Delta H$ ) and  $-146 \text{ cal mol}^{-1} \text{ deg}^{-1}$  ( $\Delta S$ ). The equilibrium dissociation constant ( $K_d$ ) for the binding of VapB26 to DNA was measured as  $4.69 \pm 0.81 \text{ }\mu\text{M}$ . The calculated stoichiometry ( $n$ ) measured in the experiment was  $1.1 \pm 0.1$ , indicating that the VapB26 homodimer interacts with DNA.

VapB26 is capable of binding to its upstream promoter DNA. Experimentally obtained values show a hydrophilic effect derived from the formation of hydrogen bonds between VapB26 and the promoter DNA (77). In our study, calorimetric trials were also performed in the absence of VapB26 under the same experimental conditions. No thermal changes were observed in the injections during the entire experiment. In addition, an ITC experiment using control DNA 'X' showed no affinity of VapB26 for this DNA (Figure 13A).

To confirm the binding specificity of VapB26, an EMSA experiment was conducted using the palindromic DNA of VapB26 and two other palindromic sequences. The DNA concentration was fixed at  $0.01 \text{ mM}$ , and the protein concentration was increased from  $0$  to  $0.8 \text{ mM}$ . As the amount of added protein

increased, the shifted band corresponding to the DNA-protein complex increased noticeably in the samples containing VapB26 promoter DNA (Figure 12B). No band shifts were observed in the other samples.

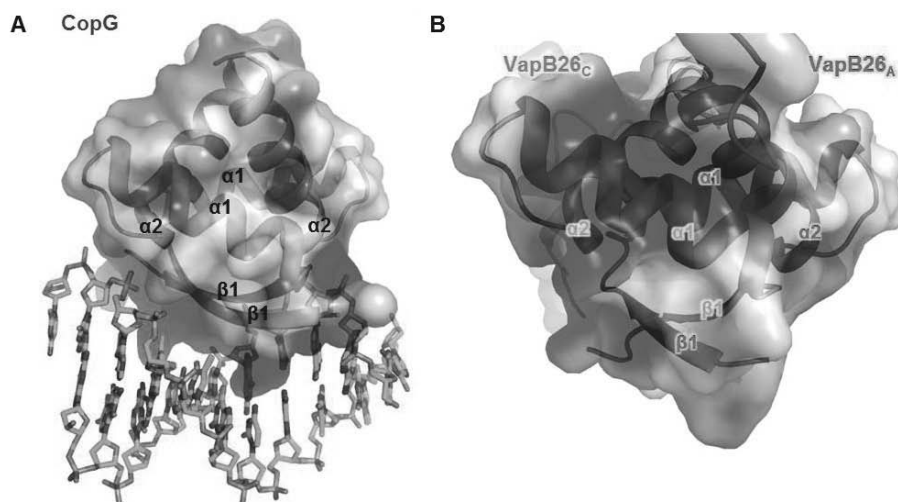


**Figure 11.** Predicted conformation of VapB26-DNA interaction, showing the electrostatic potential surface. APBS method was used to calculate the electrostatic potential. **(A)** The structure of DNA bound CopG and its electrostatic potential surface. **(B)** The electrostatic potential of RHH domain of VapB26.

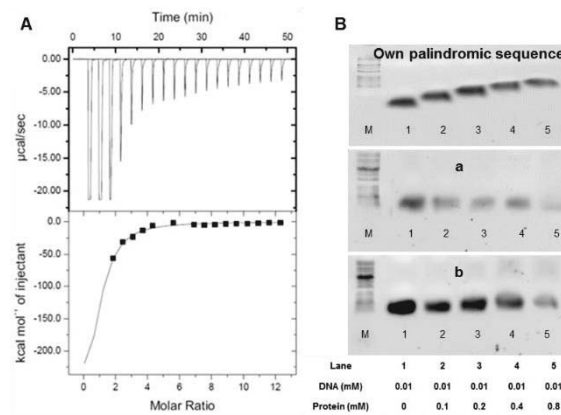


**Figure 12.** ITC assay and EMSA of VapB26 and the promoter DNA. **(A)** The binding curve of titration indicates that VapB26 is capable of binding to its upstream promoter DNA. **(B)** Upper: EMSA experiment testing the binding of VapB26 to its own promoter DNA. Middle: EMSA experiment testing the binding of VapB26 to another palindromic DNA ‘a’. Lower: EMSA experiment involving VapB26 and one more different palindromic DNA ‘b’. The concentrations of protein and DNA in each lane are indicated. The results indicate the gradual formation of DNA-protein complexes only between VapB26 and its own promoter DNA as the ratio of protein to DNA is increased. As DNA binds to a large amount of protein, the bands corresponding to the DNA-protein complex move upward.

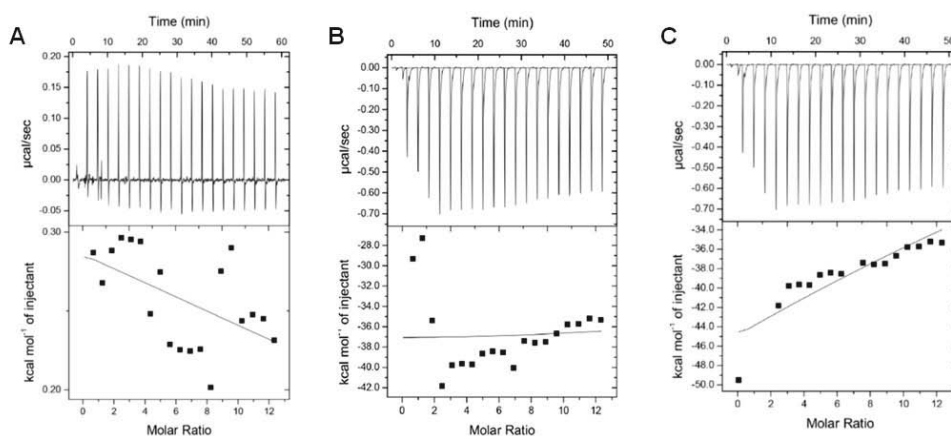


**Figure 13.** ITC assay of VapB26 with control DNA and of VapBC26 with promoter DNA. The parameters could not be calculated. **(A)** ITC assay of VapB26 and control DNA, showing no interaction. **(B)** ITC assay of VapBC26 and promoter DNA in a buffer containing 500 mM NaCl and 250mM imidazole. **(C)** ITC assay of VapBC26 and promoter DNA in a buffer containing 400 mM NaCl.

### 1.3.6 Metal-dependent ribonuclease activity of VapC26

We performed assays of the RNase activity of VapC26 using fluorescent RNA substrates. When these substrates are cleaved, they emit fluorescence in proportion to the amount of the substrate cleaved by VapC26. The fluorescence data are shown in Figures 14A and B, and the data showing the structural integrity of VapC26 are shown in Figure 15A.  $Mg^{2+}$  and  $Mn^{2+}$  significantly increase the enzymatic activity of VapC26 as the metal concentration was increased up to 5 mM, whereas the influence of  $Zn^{2+}$  on the cleavage of the RNA molecules was negligible. The RNase activity decreased at metal ion concentrations greater than 5 mM. At 50 mM  $Mg^{2+}$  and  $Mn^{2+}$ , VapC26 activity was relatively well maintained in the presence of

Mg<sup>2+</sup>, but approximately half of the VapC26 activity was lost in the presence of 50 mM Mn<sup>2+</sup>. Thus, VapC26 activity is saturated in the presence of approximately 5 mM Mg<sup>2+</sup>, but Mn<sup>2+</sup> concentrations greater than 5 mM destroy the VapC26 structure.

The ribonuclease activities of PIN domain proteins, such as VapC toxins, are strongly dependent on the presence of divalent metal ions. VapC proteins commonly bind Mg<sup>2+</sup> or Mn<sup>2+</sup> as cofactors in their catalytic sites, which consist of three or four conserved acidic residues, including Asp or Glu. However, as shown by structural and experimental studies, only three VapBC complexes obtained from *M. tuberculosis* exhibit metal-dependent ribonuclease activity. VapC3 and VapC30 from *M. tuberculosis* contain Mg<sup>2+</sup> in their active sites, and VapC15 from *M. tuberculosis* contains both Mg<sup>2+</sup> and Mn<sup>2+</sup> in its active site (37,39,40). Based on our results, we concluded that Mg<sup>2+</sup> or Mn<sup>2+</sup> is required for optimal catalytic activity of VapBC26. Moreover, Mn<sup>2+</sup> tends to destroy the structure of the protein, resulting in the preferential presence of Mg<sup>2+</sup> in VapBC26 protein.

In order to understand the structural and functional implications of the active site, we superimposed the four conserved active site residues of VapC15 toxin from *M. tuberculosis* (PDB code 4CHG), VapC26 toxin from *M. tuberculosis* (PDB code 5X3T), VapC30 toxin from *M. tuberculosis* (PDB code 4XGR), and VapC toxin from *S. flexneri* (of PDB code 3TND), which are indicated by red circles in Figure 9 (Figure 14C). The superposition shows a good fit of three conserved residues, but the location of fourth conserved residue Asp116 from VapBC26 is remote from corresponding residues of other structures. First metal ions are observed in three VapC toxin from *M. tuberculosis* but second metal ions are only observed in VapC15 toxin from *M. tuberculosis*.

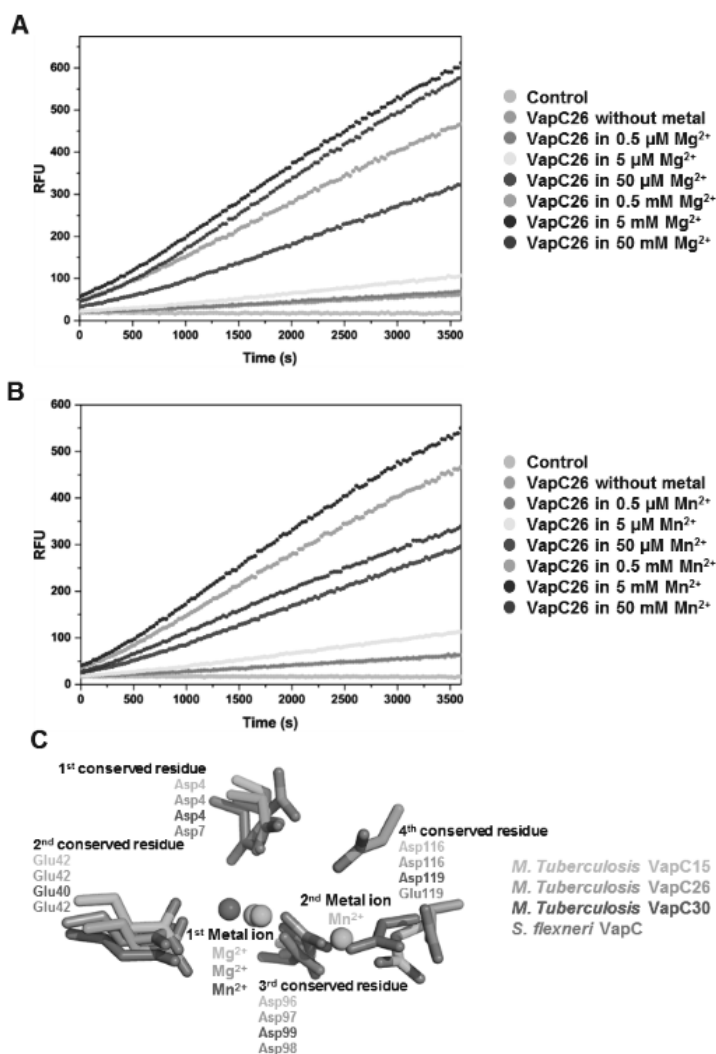


**Figure 14.** *In vitro* ribonuclease activity of *M. tuberculosis* VapC26 and comparison of active sites with homologs. When a synthetic RNA containing a fluorophore-quencher pair binds to VapC26, the RNA is digested and the quencher is removed. The released fluorophore generates fluorescence (**A and B**)



Fluorescence measurements, as a function of time, following the addition of  $Mg^{2+}$  and  $Mn^{2+}$ . Based on the results,  $Mg^{2+}$  and  $Mn^{2+}$  are essential for catalytic activity. VapC26 was treated with EDTA prior to the assay to remove metal ions. Various concentrations of  $Mg^{2+}$  and  $Mn^{2+}$  were prepared, and 40 units of RiboLock™ (Thermo Scientific) RNase inhibitor was used to prevent contamination. The control contained 50 mM  $MgCl_2$  (or 50 mM  $MnCl_2$ ), 50 mM Tris-HCl (pH 7.9), 500 mM NaCl, 250 mM Imidazole, and 40 units of RiboLock™ (Thermo Scientific) RNase inhibitor. Each experiment was performed in triplicate. **(C)** Superposition of conserved residues in active sites of VapC26 and its homologs. Residues and metal ions are marked with different colors depending on the family they belonged to.

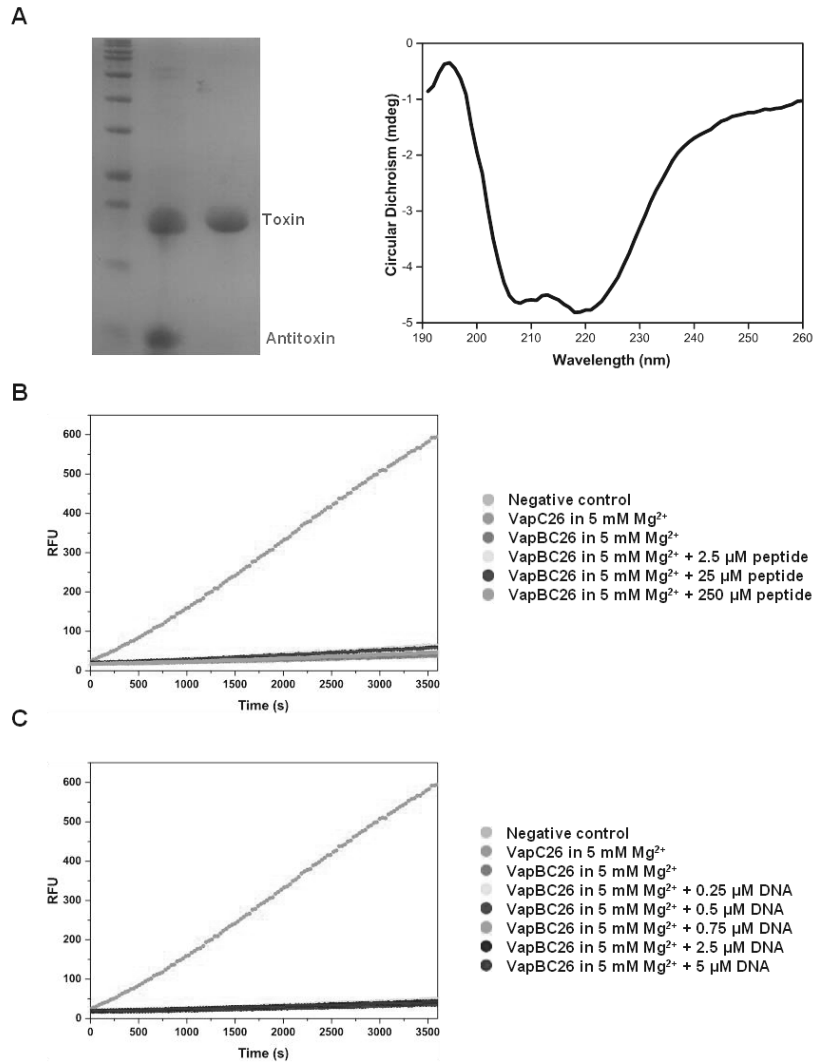


**Figure 15.** Purity and structural integrity of VapC26 and ribonuclease activity of *M. tuberculosis* VapBC26. **(A)** Left: SDS-PAGE of the TA complex of VapBC26 (left) and purified VapC26 (right). Right : Circular dichroism (CD) data of VapC26, showing the maintenance of structural integrity. **(B), (C)** Ribonuclease activity of *M. tuberculosis* VapBC26 measured using the promoter DNA and the VapB26

mimic peptide 'PPPRGGLYAGSEPIA'. Fluorescence measurements, as a function of time, for VapBC26 in the presence of peptides and DNA. Forty units of RiboLock™ (Thermo Scientific) RNase inhibitor were used to prevent contamination. VapC26 was treated with EDTA prior to the assay to remove metal ions. The negative control contained 50 mM Tris-HCl, pH 7.9, 500 mM NaCl, 250 mM imidazole, and 40 units of RiboLock™ (Thermo Scientific) RNase inhibitor. VapC26 in a solution containing 5 mM Mg<sup>2+</sup> was used as a positive control. Each experiment was performed in triplicate. Neither peptides nor DNA contributed to increases in fluorescence. Other VapB26-mimicking peptides also did not have an impact on fluorescence.

### **1.3.7 Influence of peptides on the RNase activity of VapC26**

We designed seven peptides as potential inhibitors of the interaction between VapB26 and VapC26. These peptides mimic the binding interface of VapB26 and VapC26. The sequences of peptides two and five correspond to those of portions of the binding regions of VapB26 and VapC26, respectively. Theoretically, these mimicking peptides could compete with their binding partners VapB26 and VapC26 and thereby preventing the formation of the TA complex (67). If the peptides bind with high affinity, free VapC26 would be more predominant, resulting in increased RNase activity. The sequences of the seven peptides are presented in Table 4.

As expected, the ribonuclease activity of the *M. tuberculosis* VapBC26 complex is weak compared to that of VapC26. As a result of competition with the peptide, the ribonuclease activity of VapBC26 at 2.5 μM increases. We did not observe an

increase in the fluorescence of VapBC26 following the addition of VapB26-mimicking peptides at peptide-to-protein ratios of 1:1, 10:1, or 100:1 (Figure 15). However, we confirmed that VapC26-mimicking peptides act as inhibitors (Figure 16A and Figure 17). VapBC26 showed increased activity following the addition of the  $\alpha$ 4-mimicking peptide compared to the addition of the  $\alpha$ 3-mimicking peptide and of peptides corresponding to both helices.

We conducted an additional experiment in which we fixed the concentration of the  $\alpha$ 4-mimicking peptide at 2.5  $\mu$ M and increased the concentration of VapBC26 from 0.625  $\mu$ M to 20  $\mu$ M. The plot of the relative fluorescence units (RFU) for concentrations of VapBC26 greater than 10  $\mu$ M was not markedly different from the graph for 10  $\mu$ M VapBC26 (Figure 16B).

Based on our ITC data, VapB26 showed affinity for DNA. In our NMR titration experiments, which are presented in the next section, the promoter DNA of VapB26 caused a chemical shift in the  $\alpha$ 3 helix residues of VapB26 that are involved in VapC26 binding. Therefore, we titrated VapBC26 with an increasing amount of promoter DNA to examine whether DNA weakens the interaction between VapB26 and VapC26. However, we did not observe increased fluorescence with the addition of the promoter DNA at DNA-to-protein ratio of 1:10, 2:10, 3:10, 5:10 or 20:10 (Figure 15C).

To verify that the key binding residues are necessary for the interaction between VapB26 and VapC26, an additional mutational experiment was conducted. Based on the interface, Pro46 and Tyr51 of VapB26 and Leu46 of VapC26, which occupy hydrophobic networks with multiple counterparts, were selected. The selected key residues were mutated to alanine and glutamate to diminish or remove the hydrophobic tendency. Then, 10  $\mu$ M of the  $\alpha$ 4-mimicking peptide was added to the

mutated complexes. The results show that Tyr51 of VapB26 had the greatest influence on interaction between VapB26 and VapC26, resulting in the emission of more fluorescence (Figure 16C). To confirm the statistical validity of this result, t-test was performed for Y51A and wild type, Y51E and wild type. The p-values were calculated as 0.004 for Y51A and wild type, and 0.003 for Y51E and wild type. Thus it was confirmed that the distribution of variance of each data was different. To support these results, VapB26 antitoxin, VapC26 toxin, native VapBC26 complex, Y51E complex, which is expected to have the greatest impact on interaction, and  $\alpha$ 4-mimicking peptide added each complexes were loaded into Superdex 75 10/300 preppacked column (GE Healthcare) and chromatograms were collected. The peptide added VapBC26 complexes showed peaks at different positions from the original peak corresponding VapB26 and VapC26, and the peptide added Y51E complex contained more disassembled proteins than the peptide added native complex (Figure 16D). Calculated area corresponding to VapC26 of  $\alpha$ 4-mimicking peptide added Y51E complex was 15.42 % higher than that of  $\alpha$ 4-mimicking peptide added native complex, which is well consistent with 15.07 % increased fluorescence of Y51E in Figure 16C. The volume of injected protein was 100  $\mu$ l and the concentration of proteins and  $\alpha$ 4-mimicking peptide concentration was 200  $\mu$ M and 1 mM, respectively.

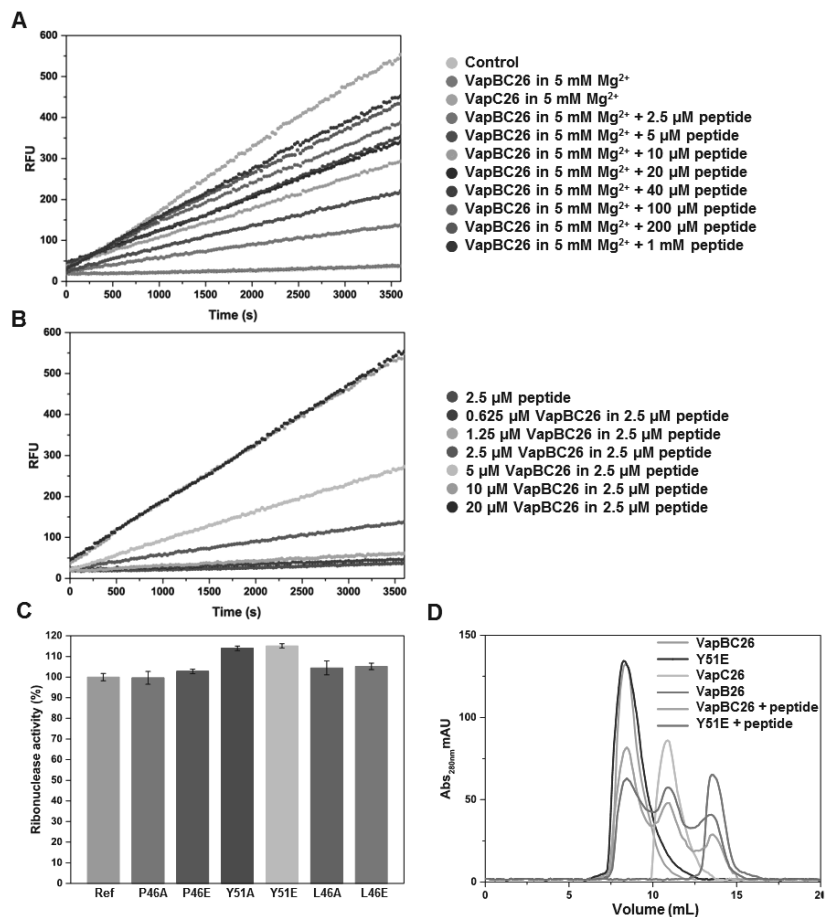


**Figure 16.** Ribonuclease activity of *M. tuberculosis* VapC26 measured using a VapC26  $\alpha$ 4-mimicking peptide and experiments using mutants. **(A and B)** The pretreatment was performed as described in **Figure 14**, and 5 mM  $Mg^{2+}$  was added to each well for optimal activity. **(A)** The concentration of VapBC26 was fixed at 2.5  $\mu$ M, and the concentration of peptide was increased from 2.5  $\mu$ M to 1 mM. The peptide inhibited the binding of VapB26 to VapC26 by approximately 50% at 10  $\mu$ M and by 80% at 200  $\mu$ M. **(B)** The concentration of the  $\alpha$ 4-mimicking peptide

was fixed at 2.5  $\mu$ M, and the concentration of VapBC26 was increased from 0.625 to 20  $\mu$ M. Based on the data, 2.5  $\mu$ M peptide interacts with approximately 10  $\mu$ M VapBC26. The experiment was performed in triplicate. **(C and D)** Comparison of the ribonuclease activity of native VapBC26 and mutated VapBC26. Pretreatment was performed as described in the legend to **Figure 14A and B**. **(C)** 10  $\mu$ M of the  $\alpha$ 4-mimicking peptide was added to the mutated complex (P46A, P46E, Y51A, Y51E, L46A and L46E). Native VapBC26, which shows approximately half the activity of VapC26 in the presence of 10  $\mu$ M of the  $\alpha$ 4-mimicking peptide, was used as a reference for comparison. The concentration of each VapBC26 mutant 2.5  $\mu$ M was the same as that of the native VapBC26 complex. RFU obtained with the reference was taken as 100%. Tyr51 of VapB26 showed the largest effect on the binding of VapB26 and VapC26. Error bars represent the standard deviation of three replicate reactions. **(D)** Size exclusion chromatography of various proteins. The UV absorption at 280 nm is plotted as a function of the elution volume.

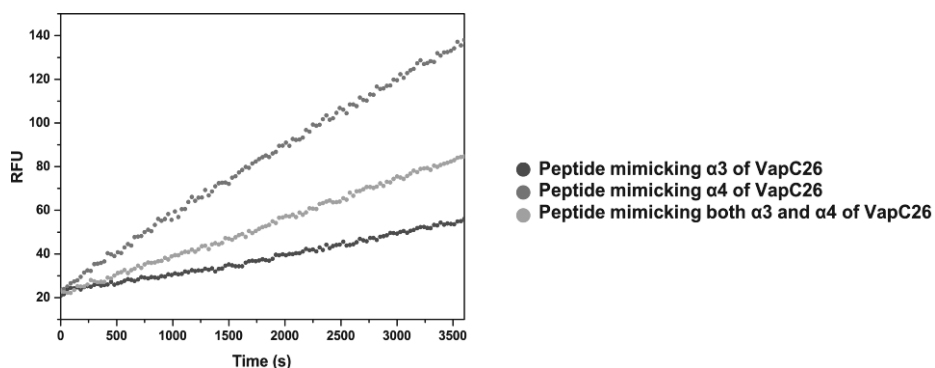


**Figure 17.** Initial test of the RNase activity of *M. tuberculosis* VapBC26 in the presence of toxin-mimicking peptides ( $\alpha 3$ ,  $\alpha 4$  and both  $\alpha 3$  and  $\alpha 4$ ). When a synthetic RNA containing a fluorophore-quencher pair binds to VapC26, the RNA is digested and the quenching is removed. The released fluorophore generates fluorescence. The test was performed approximately 10 times on a smaller scale than in the standard experiments described in the main text to identify the most effective peptide. As shown in the diagram, the peptide that mimics the  $\alpha 4$  helix has greater efficacy than the other two peptides.



**Table 4.** Residues used to create mimicking peptides

Residues (start - end)	Mimicked protein	Mimicked region
PPPRGGLYAGSEPIA (44-58)	VapB26	Coil between $\alpha 2$ and $\alpha 3$
VDELLAGF (61-68)	VapB26	$\alpha 3$
ALLAYFDAAEP (7-17)	VapC26	$\alpha 1$
PYVVAELDYLVATRVG (37-52)	VapC26	$\alpha 3$
DAELAVLRELAG (54-65)	VapC26	$\alpha 4$
YLVATRVGVDAELAV (45-59)	VapC26	Some moieties of $\alpha 3$ and $\alpha 4$
PYVVAELDYLVATRVGVDAELAVLRELAG (37-65)	VapC26	Whole $\alpha 3$ and $\alpha 4$

### 1.3.8 DNA-binding site of VapB26

In type II TA systems, the antitoxin alone or in complex with toxin typically interacts with its corresponding promoter DNA, repressing the transcription of the TA operon. Therefore, the DNA-binding properties of the antitoxin are important for the regulation of TA systems. We characterized the interactions between specific residues in VapB26 and the promoter DNA using NMR titration experiments.

We assigned the peaks to the VapB26 backbone, and 69 out of 71 cross-peaks (97.2%) observed in the  $^1\text{H}$ - $^{15}\text{N}$  heteronuclear single quantum correlation (HSQC) spectra were assigned to individual residues of VapB26, with the exception of

Pro44 and Pro45 in the proline bridge. Based on the assigned backbone  $^1\text{H}$  and  $^{15}\text{N}$  resonances, we monitored the residues showing changes in the chemical shifts or resonance broadenings upon binding to DNA. We compared the HSQC spectra of VapB26 (0.4 mM) in the absence and presence of increasing concentrations of promoter DNA (0.04 and 0.08 mM). DNA concentrations greater than 0.08 mM caused few additional changes in the chemical shifts of VapB26, suggesting that the DNA-binding site of the protein is saturated at concentrations above 0.08 mM. These comparative spectra are shown as an overlay in Figure 18C and D (dotted square in the center of the figure).

The shifts in the peaks observed in the spectra indicate that the VapB26-DNA interaction is achieved in a fast exchange on the NMR time scale, which is typically observed when molecules bind with a low to moderate affinity. We calculated the combined  $^1\text{H}$  and  $^{15}\text{N}$  chemical shift perturbation (CSP) values of VapB26 in the presence of 0.08 mM DNA using equation 1 shown in the Materials and Methods section to quantify the peak shifts. These values are plotted as a function of VapB26 residues (Figure 18A).

The CSP values of the residues belonging to the RHH DNA-binding domain were large. Residues belonging to the  $\alpha 1$  helix (Glu11, Leu12, Lys13, Ala14, and Ala15) showed an even distribution of CSP values. Some residues in the  $\alpha 2$  helix (Glu27, Ala28, Arg32, Ile35, and Val39) exhibited significant changes in their chemical shifts. Glu27, Ala28, Ile35 and Val39 located in the  $\alpha 2$  helix showed CSP values greater than 0.07. The average CSP value of  $\beta 1$  residues (Asp2-Tyr7) was less (0.021) than the CSP values of residues in the  $\alpha 1$  (0.038) and  $\alpha 2$  helices (0.045). Interestingly, moderate CSP values were observed for the residues corresponding to the  $\alpha 3$  helix in the C-terminal domain (average CSP: 0.023) in the structure of the

complex, which is involved in binding to the VapC26 toxin.

As shown in our fluorescence assay, the binding of DNA to VapBC26 did not disrupt binding of VapB26 and VapC26, when VapB26 and VapC26 were already bound. Based on the observed changes in the CSP values of the residues in the  $\alpha 3$  helix, it is estimated that DNA binds directly to the N-terminal domain of VapB26. However, the binding of DNA to VapB26 affects the conformation of the  $\alpha 3$  helix of VapB26, indicated by the moderate CSP values and the large peak intensity change. Because this region is a toxin-binding region, the binding of DNA to VapB26 might also have an effect on the binding of VapC26 to VapB26.

The results of the titration experiment were consistent with the ITC data. According to the  $K_d$  determined in the ITC experiment, the binding between VapB26 and DNA is not strong; thus, the binding mode between VapB26 and DNA is expected to show fast exchange. This result is highly consistent with the observed peak movements in the spectra of VapB26 titrated with DNA. Upon titration with DNA, the spectra of VapB26 showed peak broadening and a shift but not a peak split.

The secondary structure of VapB26 in solution was derived from the program TALOS+ (78) using the assigned chemical shift values (Table 5). VapB26 adopts a conformation that includes two  $\alpha$ -helices ( $\alpha 1$  and  $\alpha 2$ ) and one short  $\beta$ -strand; this is partially consistent with the structure of VapB26 in the VapBC26 complex. Val6 and Tyr7 at the N-terminus adopt a  $\beta$ -strand conformation. However, the presence of the  $\alpha 3$  helix (residues 60-67) in VapC26-bound VapB26 is not consistent with an unfolded structure of the corresponding region of VapB26 alone. Because this region participates in toxin binding, helix formation may be coupled to toxin binding.

In addition, the overall resonance broadenings of VapB26 residues may have occurred due to the formation of a transient complex between VapB26 and DNA, increasing the transverse relaxation rate of the protein. However, considerable resonance broadenings for specific residues are mainly attributable to their interaction with DNA in an intermediate exchange on the NMR time scale. The residues in the DNA-binding region showed low intensities and peak disappearance due to the decreased transverse relaxation. Changes in peak intensity ( $I$ ) upon DNA binding also indicate protein recognition (79). The ratios of peak intensities for DNA-bound and free VapB26 ( $I_{DNA}/I_0$ ) are plotted against the VapB26 residues to quantify the resonance broadening effect (Figure 18B). Severe resonance broadening upon binding to DNA is mainly observed for the  $\alpha 1$  and  $\alpha 2$  helices. In particular, four residues, namely Glu27, Ala28, Arg32 and Ile35, located in the  $\alpha 2$  helix show the largest reductions in peak intensities of up to approximately 95%, suggesting that these residues are key residues involved in the interaction between VapB26 and the promoter DNA. These results are in highly consistent with the CSP data showing that the  $\alpha 1$  and  $\alpha 2$  helices of VapB26 are involved in the interaction with DNA. Reduced peak intensities of several residues in the C-terminal region may be explained by changes in the dynamics from fast motion to intermediate motion when VapB26 binds to DNA.

NMR titration was also conducted using control DNA 'X'. In contrast to the results obtained using promoter DNA, the results showed almost no peak shifts. The ratios of peak intensities were well maintained with the addition of 'X' (Figure 19).

Based on these data and on the NMR results, we characterized the DNA-binding region of VapB26 and identified the changes in the VapB26 structure upon binding

to VapC26. The regions showing relatively high CSP values and peak intensity changes are mapped onto the surface representation of VapB26 in Figure 20.

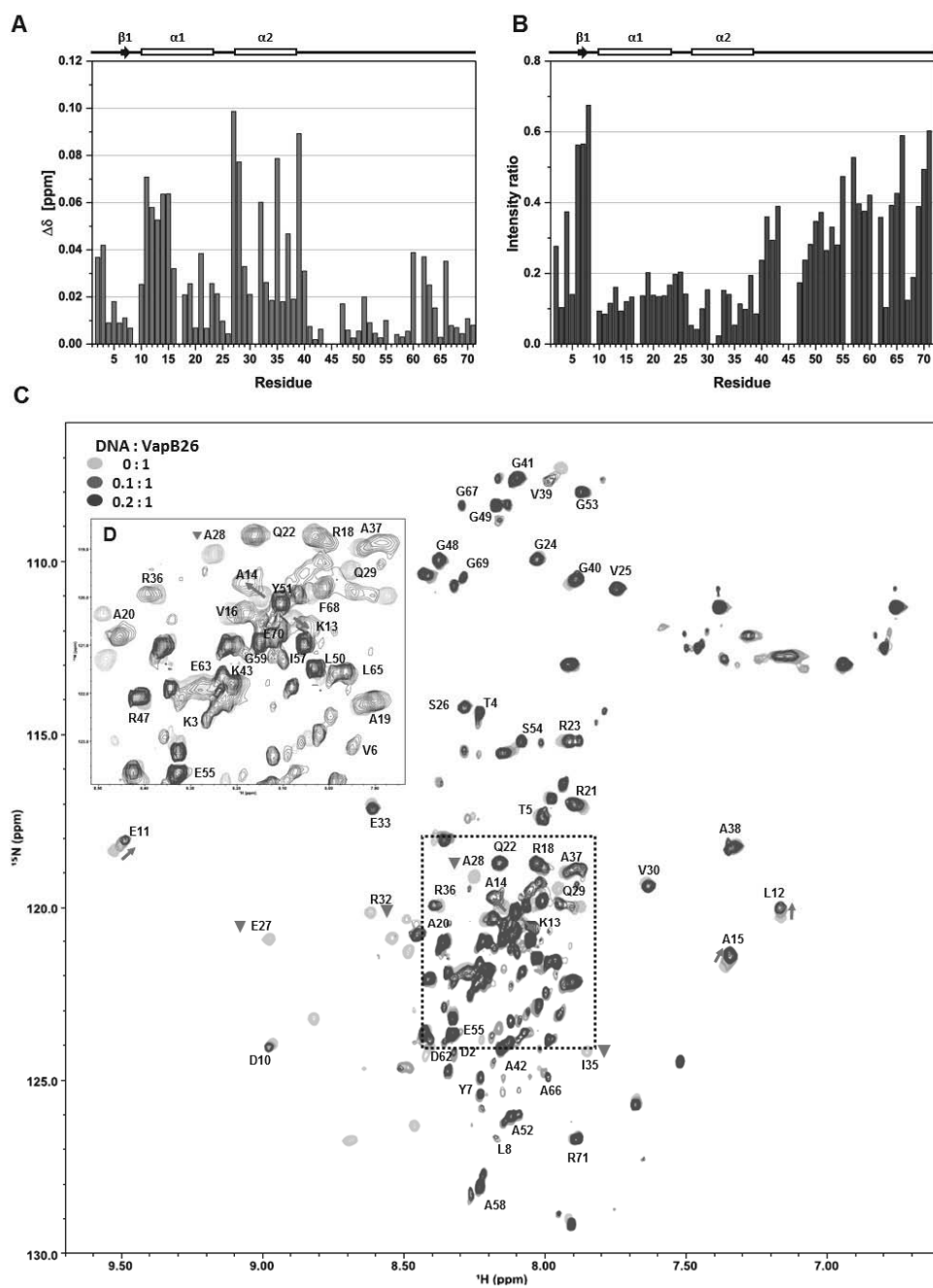


**Figure 18.** NMR titration of VapB26 and its promoter DNA. **(A and B)** Secondary structure elements based on the TALOS+ analysis are presented above the plots. **(A)** The chemical shift perturbation of each residue in the presence of 0.08 mM promoter DNA. The residues in the N-terminal RHH DNA-binding domain (Glu11, Leu12, Lys13, Ala14, Ala15, Glu27, Ala28, Arg32, Ile35 and Val39 in the  $\alpha$ 1 and  $\alpha$ 2 helices) show CSP values greater than 0.05 (blue dotted line). **(B)** Relative peak intensity compared to that of the DNA-free form. The peak intensities for Glu27, Ala28, Arg32, and Ile35 in the  $\alpha$ 2 helix exhibited the largest decreases of less than 5% compared to the peak intensity of the free form. **(C)** Overlay of 2D  $^1\text{H}$ - $^{15}\text{N}$  HSQC spectra of 0.4 mM VapB26 with increasing ratios of added DNA. VapB26 with no DNA is shown in light blue, VapB26 with 0.04 mM DNA is shown in medium blue, and VapB26 with 0.08 mM DNA is shown in dark blue. The red arrows show the peak shift direction. The Glu27, Ala28, Arg32, and Ile35 peaks disappeared during the interaction with DNA (inverted red triangle). The unassigned residues are not shown. **(D)** Expanded views of the peak overlap region highlighted with a black dotted square in **(C)**. The spectrum shows DNA/protein ratios of 0 and 0.2.

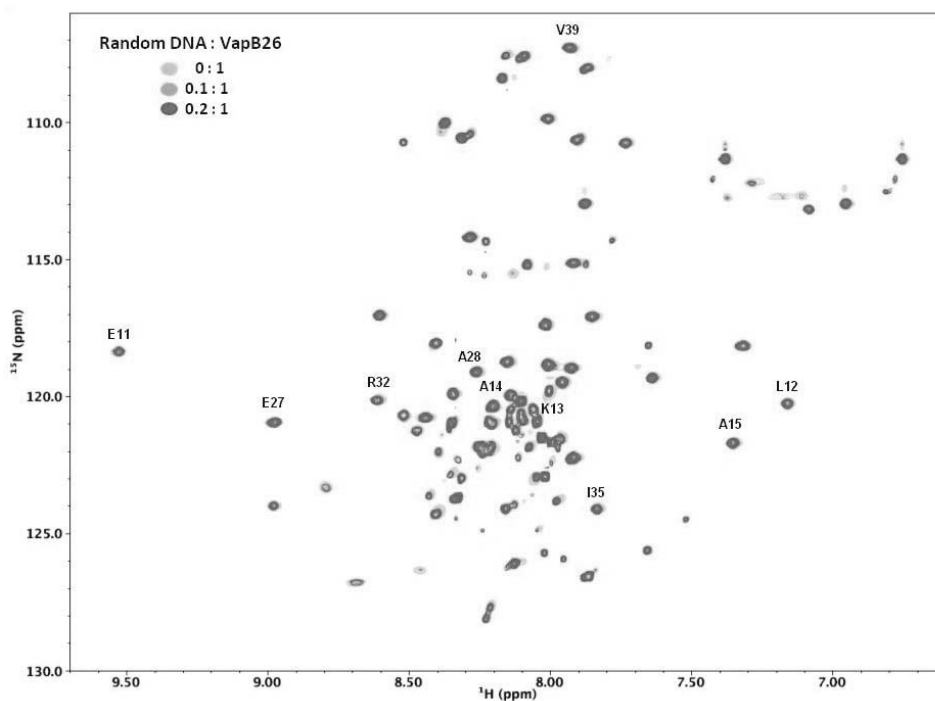


**Figure 19.** NMR titration experiment of VapB26 and control DNA ‘X’. Overlay of 2D  $^1\text{H}$ - $^{15}\text{N}$  HSQC spectra of 0.4 mM VapB26 with increasing ratios of added DNA ‘X’. VapB26 with no DNA ‘X’ is shown in light green, VapB26 with 0.04 mM DNA ‘X’ is shown in medium green, and VapB26 with 0.08 mM DNA ‘X’ is shown in dark green. The peaks that displayed distinct changes during the interaction of VapB26 with promoter DNA are indicated. None of the indicated peaks show distinct changes in both the peak shifts and the intensity ratio in this spectrum.



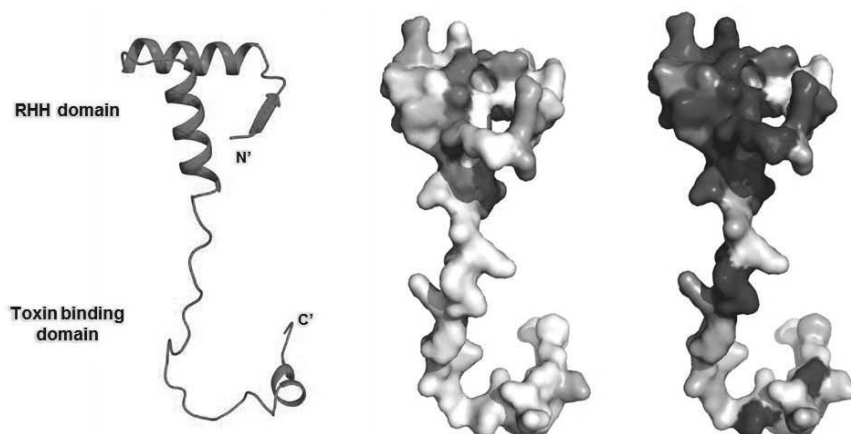


**Figure 20.** Schematic representation and surface representation of VapB26 mapped with CSP values (red) and intensity-related values (blue). The residues are colored with a gradient indicating their CSP values and intensity decrease upon the addition of promoter DNA. As predicted, large CSP values were observed for the residues belonging to the RHH DNA-binding domain, particularly residues in the  $\alpha 1$  and  $\alpha 2$  helices. Moreover, large decreases in peak intensities were observed for residues in the  $\alpha 1$  and  $\alpha 2$  helices. The  $\beta 1$  region in the crystal structure showed relatively low values for both parameters.

**Table 5.** Predicted secondary structures with confidence scores offered by Talos based on the backbone-assigned amino acid sequence of VapB26

Sequence										M	D	K	T	T	V	Y	L	P	D
Predicted secondary structure										L	L	L	L	L	E	E	L	L	H
Confidence score										0	3	8	9	6	5	7	5	8	7
E	L	K	A	A	V	K	R	A	A	R	Q	R	G	V	S	E	A	Q	V
H	H	H	H	H	H	H	H	H	H	H	H	H	L	L	L	H	H	H	H
9	9	9	9	9	9	9	9	9	9	9	8	2	7	5	7	8	9	9	9
I	R	E	S	I	R	A	A	V	G	G	A	K	P	P	P	R	G	G	L
H	H	H	H	H	H	H	H	L	L	L	L	L	X	X	L	L	L	L	L
9	9	9	9	9	9	9	5	4	8	8	8	9	0	0	9	9	8	7	4
Y	A	G	S	E	P	I	A	R	R	V	D	E	L	L	A	G	F	G	E
L	L	L	L	L	L	L	L	L	L	L	L	L	L	L	L	L	L	L	L
8	8	9	0	0	9	9	8	7	4	5	8	9	9	9	8	7	7	7	8
R																			
L																			
0																			

H = helix, E = strand, L = coil, X = unassigned two prolines.

Confidence is scored from 0 (low) to 9 (high).

## 1.4 Discussion

### 1.4.1 Insights into the unique structure of the VapBC26 complex

Based on the complete analysis of the VapBC26 structure, the binding affinities of VapB26 and VapC26 may be stronger than those of other VapBC structures. Due to their binding affinity for the toxin via the binding domain, the N-terminus-lacking structures of VapBC might have lower steric hindrance than the complete structure. The average binding interface area of VapBC30 (1,002.1 Å<sup>2</sup>) is considerably smaller than the average area of the complete chains of VapBC26 (1,255.05 Å<sup>2</sup>), and the average  $\Delta G$  (kcal/mol) for VapBC26 (-15.9) is considerably different from the values for VapBC5 (-12.0) and VapBC15 (-12.9), calculated by PISA server (64).

This binding force of VapBC26 is mainly attributed to hydrophobic interactions. The proportion of hydrophobic interactions in the total interactions is higher than that of other VapBC complexes. Ring-type amino acids, such as prolines and aromatic amino acids, including phenylalanine, tryptophan and tyrosine, comprise a large proportion of hydrophobic interactions. The abundant aromatic amino acids in VapBC26 may largely contribute to maintaining the structural integrity and proper function of the protein (80). The strong hydrophobic force derived from the ring results in strong binding (81). Pro44, Pro46, Tyr51, Pro56 and Phe68 of VapB26 and Tyr11, Phe12, Pro17, Tyr45 and Trp68 of VapC26 participate in the interaction between VapB26 and VapC26; together, these residues represent more than 30% (10/29) of the total number of amino acids that participate in the interaction between VapB26 and VapC26.

The proline bridge (Pro44, Pro45 and Pro46) in VapB26 plays a supporting role at the beginning of the toxin binding region. Proline is a strong disruptor of secondary structure in both  $\alpha$ -helices and  $\beta$ -strands due to its spatial hindrance, which can prevent the formation of secondary structure. Moreover, the proline bridge of VapB26 serves as a boundary for the DNA-binding and toxin-binding moieties, as it is located in the middle of the disordered region (82-85). Tyr45, Pro37 and Tyr38 of VapC26 participate in binding to the adjacent VapC26 protein. In addition, Tyr45 and Phe120 of VapC26 are involved in maintaining protein functions by stabilizing the active site of the VapC26 protein (86). Peptides, including Tyr45 in the  $\alpha$ 3 helix, show less activity than other peptides (Figure 17).

In the case of *Haemophilus influenza* VapC1, mutation of 17 amino acid residues in VapC1 showed that these residues do not play essential roles in the interaction of the protein with its cognate antitoxin (87). However, in our study, although single mutations of Pro46 and Tyr51 in VapB26 and of Leu46 in VapC26 did not totally disrupt the interaction required to form VapBC26, the slightly increased ribonuclease activity of the mutated VapBCs and decreased complex form of Y51E compared to native complex when of  $\alpha$ 4-mimicking peptide was added in size exclusion chromatography supports a role for these hydrophobic residues in forming the VapBC26 interface.

#### **1.4.2 DNA-binding mechanism of VapB26 and the ensuing conformational change**

According to studies of FitAB from *N. gonorrhoeae*, VapBC2 from *R. felis* and VapBC from *S. flexneri* (41,42,71), the  $\beta$ 1 residues of VapB26 mediate the contact

between VapB26 and DNA but do not directly participate in the binding interface. Upon binding to DNA, the conserved residues in  $\beta 1$  recognize DNA, key residues in the two helices directly contacting DNA, and residues in the  $\alpha 2$  helix bind to the phosphate backbone of DNA at the major groove (73). Alterations in the N-terminal region induced by the interaction with DNA are maintained by two flexible loops between  $\beta 1$  and  $\alpha 1$  as well as between  $\alpha 1$  and  $\alpha 2$ .

In our study, the notable chemical shift perturbation and decrease in the intensity of residues in the  $\alpha 1$  and  $\alpha 2$  helices revealed that the Glu27, Ala28, Arg32, Ile35 and Val39 residues are important for binding to DNA. In this interaction, the promoter site is located in close proximity to RNA polymerase, and transcription is repressed. Therefore, the normal biological functions of bacteria are blocked (88). Promoter DNA is bound by VapBC26 in an extracellular environment, but as *M. tuberculosis* enters epithelial cells, DNA is released and transcription is initiated (71). Our identification of the residues required for the interaction between VapB26 and promoter DNA will help elucidate the transcriptional repression mechanism and downstream biological actions.

VapB proteins with a  $\beta$ -barrel hairpin domain do not form antiparallel  $\beta$ -sheets until they bind to DNA. Upon interacting with DNA, the  $\beta$ -strands pack tightly to form a complete DNA-binding domain (42). Proteins, such as HU, have flexible  $\beta$ -arms and bend inward when binding to DNA (89). However, VapB26 naturally forms a homodimer in solution, as shown in our multi-angle light scattering (MALS) data (Figure 2), and the RHH domain of VapB26 was confirmed by analyzing the crystal structure of the DNA-free protein. Thus, VapB26 does not undergo dramatic conformational changes in the N-terminal region before and after DNA binding.

In contrast, the TALOS+ (78) secondary structure prediction showed that the binding of DNA to VapB26 generates conformational and dynamic changes in the  $\alpha 3$  helix of VapB26, unlike the VapC26-bound structure. VapC26 does not directly participate in the interaction with DNA. However, for FitAB, HipAB and MazEF, the binding affinity of VapB26 to DNA is increased when the antitoxins bind the toxins (71,90,91). VapC26 might thermodynamically contribute to the interaction between VapB26 and DNA by forming a complex with VapB26 and stabilizing the N-terminal-binding domain of VapB26 (92). Similarly, transcription factors undergo conformational changes that increase structural stability or substrate specificity by induced fit or local folding (93-95). Studies of the relationship between the conformational changes that occur in VapB26 and its binding to VapC26 or DNA would be interesting.

Although we were unable to calculate parameters for the interaction between VapBC26 and promoter DNA due to the poor stability of the protein under low salt conditions (Figures 13B and C), the C-terminal toxin-binding domain of VapB26 is affected by DNA binding according to our NMR data. Importantly, VapB26, VapC26 and DNA have a mutual relationship (96,97).

#### **1.4.3 Mechanism of the *in vitro* ribonuclease activity of VapC26**

According to our experimental data, the ribonuclease activity of VapC26 was only observed when VapC26 was released from VapB26. EDTA-treated VapC26 did not display ribonuclease activity. Thus,  $Mg^{2+}$  and  $Mn^{2+}$  are essential for VapC26 to block translation by degrading the RNA and inhibiting bacteria growth. Because  $Mg^{2+}$  is smaller than  $Mn^{2+}$ ,  $Mg^{2+}$  has a strong tendency to mediate water-mediated

interactions with the active site.  $Mg^{2+}$  activates the water molecule for nucleophilic attack and stabilizes the active site. This mechanism is shared by other nucleases and ribonucleases (98-100).

The C-terminal  $\alpha 3$  helix of VapB26 may affect the position of  $Mg^{2+}$  and  $Mn^{2+}$ , which are essential for ribonuclease activity. The  $\alpha 3$  helix of VapB26 precisely blocks the putative RNA-binding site of VapC26 and  $Mg^{2+}$  binding by covering the active site. When VapB26 is not bound to VapC26,  $Mg^{2+}$ , the RNA substrate and the active site of VapC26 form an active complex (37,39,44,87,101).

Although VapC toxins share structural similarity of active site, they could recognize different targets. VapCs from *S. flexneri*, *Salmonella typhimurium*, and *Leptospira interrogans* cleave tRNA in the anticodon stem loop (ASL) (49,102). In *M. tuberculosis*, VapC4, VapC11, VapC15, VapC25, VapC28, VapC29, VapC30, VapC32, VapC33, VapC37, and VapC39 cleave tRNA (49). VapC20 and VapC26 cut the 23S rRNA in the sarcin-ricin loop (SRL) (47,49). On the basis of previously suggested mechanism of two-metal ion (103), first metal ion in VapBC system can accommodate phosphate hydrolysis, whereas second metal ion seems to be required to stabilize the conformation of active site. In the structural comparison of active sites with reported VapC structures (Figure 14), second metal ion is coordinated by 4<sup>th</sup> conserved residue. Corresponding residues of the ASL enzymes, VapC toxin from *S. flexneri*, and VapC15 and VapC30 toxins from *M. tuberculosis* showed conservation of geometry. However, the VapC26 toxin from *M. tuberculosis*, SRL enzyme exhibited different position of the 4<sup>th</sup> conserved residue. These structural differences of VapC toxins would cause target specificity in spite of their structural similarity, resulting in the different function of ASL enzyme and SRL enzyme.

#### **1.4.4 Importance of the VapBC26 system as an antibiotic target**

VapBC systems are of great importance in the study of *M. tuberculosis* because they are present in quite small numbers in other mycobacteria, compared to *M. tuberculosis* (35). Furthermore, VapBC26 has great importance as a potential antibiotic target. First, in the hypoxic state, VapB26 expression varies greatly (35), suggesting the possible importance of VapB26 in the stress state. Second, VapC26 is a ribotoxin, cutting the SRL. SRL is the longest conserved sequence in 23s rRNA and is crucial for triggering of GTP hydrolysis and for the anchoring of the elongation factor during mRNA-tRNA translocation (50,104). In particular, sarcin and ricin, which actually targets the SRL, completely inactivate the ribosome. Third, strong growth arrest of *E. coli* occurs when *L. interrogans* VapC is expressed (105). Even more crucially, the expression of VapC26 strongly inhibits the growth of *M. smegmatis* (106,107).

In conclusion, VapC26 can exhibit growth inhibition effect of target cell and act as an effective translation inhibitor. Therefore, the VapBC26 system is expected to bring about new antibiotic target and peptide inhibitor of TA interaction could be a potential antibiotics.

#### **1.4.5 Artificial toxin activation by inhibition of the TA complex**

We designed several VapB26 mimetic peptides in an attempt to disrupt the VapBC26 complex. In *B. anthracis* PemIK, peptide inhibitors that mimic the C-terminal toxin-binding region of PemI influence the TA interaction (108). A peptide designed to mimic the backbone of MoxX also influences the TA



interaction (109). The active site of VapC26 interacts with the  $\alpha 3$  helix and the C-terminal region of VapB26, but the peptide mimicking the  $\alpha 3$  helix of VapB26 does not show any enzymatic activity. With respect to the disruption of the VapB30-VapC30 interaction by the designed peptides, VapB30 lacks the N-terminal residues from 1-46 unlike the complete form of VapB26 (40); this may weaken and prevent complete binding. However, the VapC26-mimicking peptides show great potential as antimicrobial agents. The toxin-mimicking peptides used in the present study interrupted the binding of VapB26 and VapC26 by approximately 80% or more at the highest peptide concentration. These data provide evidence suggesting that this peptide may represent novel pharmaceutical compound.

The development of antibiotic drugs based on the TA systems of pathogenic bacteria has attracted interest, and the artificial activation of toxins is a powerful antibacterial strategy. For this purpose, the inhibitor molecule must bind tightly to the TA interaction site to disrupt the TA interaction. The VapC26-mimicking peptide generated in the present study shows possibility as a bactericidal agent based on protein (antitoxin)-protein (toxin) interaction (PPI-approaches) (10,110,111). We may be able to obtain a more optimized inhibitor by applying bio-active techniques, such as stapled peptides. Stapled peptides are stabilized by a hydrocarbon cross-link to form a bioactive conformation and have enhanced membrane permeability (112). Attaching cell-penetrating peptides (CPPs) to the peptide inhibitors might be considered as a way of improving the delivery of antibiotic peptides to appropriate target tissues, and the limited side effects of these peptides *in vivo* and *in vitro* and their rapid penetration into bacterial cells of CPPs could enhance their efficiency (113,114). In addition, various modifications can be attached to peptide by conjugation strategies. Combination therapy and surface

modulation can increase antibacterial activity and membrane permeability (115). Furthermore, peptide nanoparticles are economical and biocompatible for therapeutic applications (116).

Adequate activation of toxins may induce trivial chronic infections by encouraging the formation of persister or dormant cells. Based on the experimental data obtained in this study, the peptide inhibitors described here may be a new antimicrobial agent.

## 1.5 Conclusion

Pathogenic bacteria, such as *M. tuberculosis*, utilize many toxin-antitoxin (TA) systems to survive. TA systems are strongly correlated with bacterial physiology, such as gene regulation, growth arrest, survival, and apoptosis. The VapBC TA family is one of the most widely distributed TA families. However, crystal structures have only been determined for the following six VapBC TA complexes to date. The VapC26 toxin damages a host cell by inducing RNA degradation or binding to topoisomerase or ribosome. The VapB26 antitoxin is an important cellular components for cell maintenance and viability because it neutralizes the detrimental activity of its cognate toxin. The VapB26 antitoxin acts as a repressors that auto-regulates the transcription of the TA operon. The VapC26 toxin exhibits ribonuclease activity toward cellular mRNAs.

In particular, we present the crystal structure of the VapBC26 complex from *M. tuberculosis* at a resolution of 2.653 Å. The structure revealed the important residues involved in binding to the promotor DNA and in the formation of the VapBC26 complex. The VapC26 toxin forms an overall  $\alpha/\beta/\alpha$  structure with four parallel  $\beta$  strands, and VapB26 adopts a ribbon-helix-helix (RHH) DNA-binding motif. The core residues in VapB26 that bind to DNA and the structural changes in VapB26 resulting from toxin binding were clarified by nuclear magnetic resonance (NMR). The catalytic site of VapC26 is composed of three conserved acidic residues that bind to  $Mg^{2+}$ , and the ribonuclease activity of VapC26 was confirmed in this study. Several peptides were designed as antibiotic candidates to mimic the binding interface of the VapBC26 complex and thereby suppress the TA

interaction. This approach may contribute to the development of novel, potent antibiotics that are effective treatments for antibiotic-resistant *M. tuberculosis*.

## **Chapter 2. Functional details of the *Streptococcus pneumoniae* HicBA toxin-antitoxin system**

### **2.1 Introduction**

*Streptococcus pneumoniae* is gram-positive, facultative anaerobic, and significant human pathogenic bacteria. This bacterium causes otitis media, sinusitis, pneumonia and meningitis. *S. pneumoniae* is usually inhaled by respiratory system and stays in pharynx and nasal cavity to generate diseases (117,118). Glycopeptide antibiotics vancomycin as well as penicillin is frequently used to eradicate bacteria and relieve symptoms (119,120). However, in worldwide, *S. pneumoniae* gathered outstanding remark of antibiotic resistance. Unfortunately, extensive drug-resistant *S. pneumoniae* has been appeared and it shows resistance to penicillin, cephalosporin, macrolide,  $\beta$ -lactam antibiotics fluoroquinolone and even to vancomycin and linezolid (121-123). Nowadays, antibiotics combination therapy is used to get synergism, but it cannot effectively suppress the drug-resistant bacteria (124-126). Therefore, the development of new antibiotic candidates to eradicate *S. pneumoniae* by exploiting new therapeutic strategies is urgently needed.

In the bacterial strain *S. pneumoniae* TIGR4, there are only six TA loci (three RelBE family, one phd-doc family, one HigBA family and one HicBA family) (33). There is a relatively small number of TA loci in *S. pneumoniae*, compared to other bacteria. For the example, *Mycobacterium tuberculosis* has more than 88 TA operons known. Action mechanisms of TA have been studied for ages but

physiological roles of TA have not yet been clearly elucidated (35,36,38). Furthermore, to date, crystal structure of HicBA TA complex has been determined for only one from *Yersinia pestis*, Protein Data Bank (PDB) code 4P78 (HicBA3), which lacks the C-terminal region of antitoxin (127).

HicB antitoxins consist of the two functional motifs: N-terminal region that binds to the toxin and thereby abolishes its toxicity, and the C-terminal region that binds to the promoter DNA of the TA operon that auto-regulates TA operon (51,52). DNA-binding domain of HicB (128) forms ribbon-helix-helix (RHH) (73) or helix-turn-helix (HTH) motives (72). HicA toxins contain double stranded RNA binding domain (DsRBD) (129) and exhibit ribonuclease activity (130). The active sites of HicA toxins contain conserved histidine residue (127,131).

Here, we present the crystal structure of the HicBA complex from *S. pneumoniae* TIGR4 at a resolution of 2.30 Å. The C-terminal DNA-binding domain of HicB antitoxins shows a considerable structural deviation and HicA toxin has contacts with a curved back of the HicB antitoxin. The structure revealed the important residues in the formation of the HicBA complex. The core residues in HicB that bind to DNA and properties of DNA binding domain were clarified by nuclear magnetic resonance (NMR). Binding interface mimicking peptides were designed as antibiotic candidates to be antimicrobial peptides (AMP) and thereby suppress the TA interaction. This approach may contribute to the development of novel, potent antibiotics that are effective treatments for antibiotic-resistant *S. pneumoniae*.

## 2.2 Experimental procedure

### 2.2.1 Cloning and transformation

The genes of HicB (SP1786) and HicA (SP1787) were amplified by using polymerase chain reaction (PCR). The primers used in PCR are HicB-F/HicB-R for HicB and HicA-F/HicA-R for HicA (Table 6). Restriction enzymes used for cloning were *NdeI* and *XhoI*. The PCR product of both HicB and HicA were double-cut by *NdeI* and *XhoI* and ligated to vectors which were cut by same enzymes. For structure determination and biological assay, HicB and HicA were ligated to pET21a without tag and pET28b, respectively. The pET28b N-terminal tag was added to HicA as an additional residual (MGSSHHHHHHSSGLVPRGSH) tag. For NMR experiments, residues of HicB containing DNA binding domain (HicB<sup>109-150</sup>) were cloned. The primer used in PCR are HicB<sup>109-150</sup>-F and HicB-R (Table 6). Enzyme cutting was conducted as same way and pET28b was used for ligation with same tag. For confirmation of residue essential in ribonuclease activity of HicA, His36 of HicA was mutated to Ala36 (HicA-H36A). The primers used in PCR are H36A-F/H36A-R (Table 6). Mutation was conducted by using EZchange™ Site-Directed Mutagenesis Kit (Enzynomics, Korea) and protocol was same with manufacturer's protocol.

**Table 6.** Primers used in experiment.

Primer	Sequence
HicB-F <sup>a</sup>	5'-GGAATT <u>CCATATG</u> ATGTTAGTTACGTATCC-3'
HicB-R <sup>b</sup>	5'-CCGCT <u>CGAG</u> CGGTTAGGCTTGAACCTTCTTATC-3'
HicA-F <sup>a</sup>	5'-GGAATT <u>CCATATG</u> ATGGTGTGTGTCAGGAGG-3'
HicA-R <sup>b</sup>	5'-CCGCT <u>CGAG</u> CGGTTACAACCCAGCTTGCTTTC-3'
HicB <sup>109-150</sup> -F <sup>a</sup>	5'-GGAATT <u>CCATATG</u> GGAAGTCAGGAACCCAT-3'
H36A-F <sup>a</sup>	5'-TAGAGGCGGTAAAGGCTCCGCTATTAATAATGGAAAAGCAAG-3'
H36A-R <sup>b</sup>	5'-CTTGCTTTTCCATTTTAATAGCGGAGCCTTTACCGCCTCTA-3'
F22A-F <sup>a</sup>	5'-GGAACAGAAGCGACTTATGCTGTCCATTTCCCAGATTTT-3'
F22A-R <sup>b</sup>	5'-AAAATCTGGGAAATGGACAGCATAAGTCGCTTCTGTTCC-3'
T33A-F <sup>a</sup>	5'-GATTTTGAATACTCAGCTACACAAGGAGAGGGGATTTCT-3'
T33A-R <sup>b</sup>	5'-AGAAATCCCCTCTCCTTGTGTAGCTGAGTATTCAAAATC-3'
Q34A-F <sup>a</sup>	5'-TTTGAATACTCAGCTACAGCAGGAGAGGGGATTTCTGAG-3'
Q34A-R <sup>b</sup>	5'-CTCAGAAATCCCCTCTCCTGCTGTAGCTGAGTATTCAAA-3'
E47A-F <sup>a</sup>	5'-GCTTTGGCTATGGGGTCGGCGTGGCTAGGGATAACTGTT-3'
E47A-R <sup>b</sup>	5'-AACAGTTATCCCTAGCCACGCCGACCCCATAGCCAAAGC-3'
F80A-F <sup>a</sup>	5'-TTAATTGATAATGATCCTGCTAAAGATGATGAAGATTTC-3'
F80A-R <sup>b</sup>	5'-GAAATCTTCATCATCTTTAGCAGGATCATTATCAATTAA-3'
T89A-F <sup>a</sup>	5'-GATGAAGATTTTCGTGTCAGCCTATGACCTTGATAAATCT-3'
T89A-R <sup>b</sup>	5'-AGATTTATCAAGGTCATAGGCTGACACGAAATCTTCATC-3'

<sup>a,b</sup> F and R represent forward and reverse respectively. Enzyme sites are underlined above.



### 2.2.2 Protein expression and purification

For crystallization, the cloned plasmids of HicB and HicA were co-transformed into *E. coli* Rosetta2 (DE3) pLyss competent cells. Cells were grown at 37°C in Luria broth (LB) until the OD<sub>600</sub> reached to 0.8. The protein overexpression was induced by the addition of 0.5 mM isopropyl 1-thio-B-D-galactopyranoside (IPTG) and further incubation was followed at 37 °C for 4h. Cultured cells were harvested at 11,355 x g at 4 °C by centrifugation and stored -80°C. Then, harvested cells were suspended in buffer A (20 mM Tris-HCl, pH 7.9, and 500 mM NaCl) with 5 % glycerol of total volume and lysed by using ultrasonication. After centrifugation for 1 h at 28,306 x g, supernatant containing soluble proteins was loaded to Ni<sup>2+</sup> affinity open column (Bio-Rad) which was equilibrated with buffer A in advance and washed by buffer A containing 50 mM imidazole. Then protein bound to Ni<sup>2+</sup> column was eluted by using imidazole gradient (100–700 mM) and TA complex of each fraction was identified by using Sodium Dodecyl Sulfate Polyacryl Amide Gel Electrophoresis (SDS–PAGE). Finally, the buffer containing TA complex was changed to buffer consisting of 20 mM Tris, pH 7.5 and 150 mM NaCl by size-exclusion chromatography on a HiLoad 16/600 Superdex 200 prep-grade column (GE Healthcare) and concentrated to 10mg/ml by using Amicon Ultra centrifugal filer unit (Millipore). The purity of TA protein complex was verified by SDS-PAGE. For Ribonuclease assay, HicA and HicA-H36A were expressed and purified by same procedure, except that HicA was incubated 2h after IPTC induction because of its toxicity to *E. coli*. HicBA complex displaced by selenomethionine (SeMet) was done by same procedure, except that cells, containing HicBA complex displaced by SeMet were grown in M9 medium containing extra essential amino

acids. For NMR experiments, the N-terminal (His)<sub>6</sub>-tagged HicB<sup>109-150</sup> protein was expressed in *E. coli* strain BL21(DE3) using M9 medium mixed with 1.0 g/l [U-<sup>13</sup>C] glucose and 1.0 g/l [<sup>15</sup>N] NH<sub>4</sub>Cl (Cambridge Isotopes Laboratory) as the sole carbon and nitrogen sources respectively. The purification steps of HicB<sup>109-150</sup> was same with that of TA complex and 100 units of thrombin from human plasma (Sigma-Aldrich) was added to 10 mg of purified protein and further incubated overnight at 20 °C to cleave the (His)<sub>6</sub> tag, prior to size exclusion chromatography in a buffer consisting of 20 mM sodium phosphate (Na Pi), pH 7, and 100 mM NaCl. VapC26 and VapC30 from *M. tuberculosis* were expressed and purified as reported previously (40,132).

### 2.2.3 Crystallization, data collection and processing

Initial crystal screening with purified HicBA complex protein was conducted using kits named crystal screening 1,2 and Index (Hampton Research) by mixing 1 µl of protein solution (at 10 mg/ml in 20 mM Tris, pH 7.5 and 150 mM NaCl) and 1 µl of reservoir solution. Crystals of HicBA complex were grown using sitting-drop vapor diffusion method at 4°C. The crystallization solution for HicBA was 0.1 M Tris, pH 8.5 and 2.0 M Ammonium sulfate. Cryoprotection for HicBA was achieved by adding 20% glycerol to the solution. Crystals were flash-cooled in liquid nitrogen before data collection. Data was collected using ADSC Quantum Q270r CCD detector at beamline 5C and 7A of Pohang Light Source, Republic of Korea. Crystals of HicBA complex belong to *orthorhombic* space group P2<sub>1</sub>2<sub>1</sub>2, with unit cell parameters of a = 106.263 Å, b = 116.541 Å, c = 42.490 Å, α = β = γ = 90.00° for native HicBA crystal and a = 106.926 Å, b = 116.602 Å, c = 42.680 Å,

$\alpha = \beta = \gamma = 90.00^\circ$  for SeMet-labeled ones. Calculated total mass of protein complex was 26349.7 Da including N-terminal histidine tag. All raw data were scaled and processed using the HKL2000 (55). The structure of HicBA complex from *S. pneumoniae* was determined at 2.80 Å resolution by single wavelength anomalous dispersion using SeMet. The final structure of HicBA was determined by molecular replacement. The data 2.30 Å of native crystal was used for structural analysis and SeMet data was used as model for native one. Two structures had almost same protein fold. Detailed statistic information is well described in Table 7. In SeMet structure, we determine the positions of 14 selenium sites out of total asymmetric unit. *PHENIX* (56) was first used to automatically build a total residues and the remaining residues were built in *Coot* (57) to provide the final model that was refined to  $R_{work}$  and  $R_{free}$  (58) of 20.2 and 24.0 % for SeMet one and 20.5 and 23.6 % for native one by using *REFMAC* and *Phenix* refinement (56,59), respectively. Overall geometry was validated using *Molprobit* (60), and 98.02 % of the residues were in the favored region of Ramachandran plot and additional 1.98 % were in the allowed region in the native structure. PyMOL was used to generate all figures (133). The electrostatic potential surfaces were calculated using Adaptive Poisson-Boltzmann solver (APBS) method (62). The quality of protein purification and manufactured crystals are described in Figure 21.

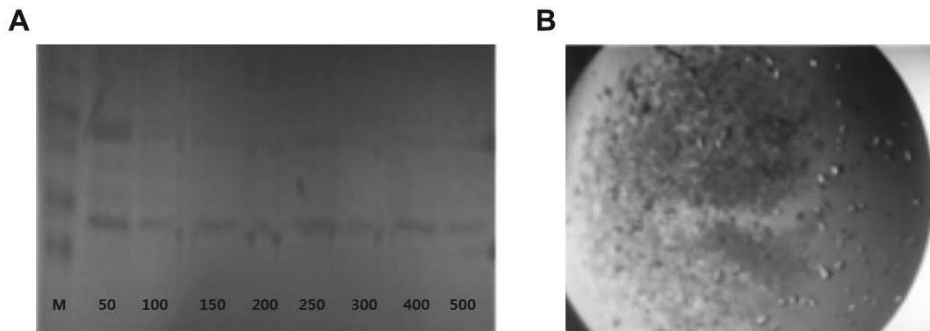


**Figure 21.** Purification and crystallization of HicBA from *S. pneumoniae*. **(A)** Column elution using engineered histidine tags. Concentration gradient is plotted at the bottom. **(B)** Generated crystals of HicBA from *S. pneumoniae*.

**Table 7.** Data-collection and refinement statistics for SeMet and native structures.

(a) Data collection details. Values in parentheses are for the highest resolution shell.

Data set	SeMet	Native
X-ray source	5C beamline of PLS, Korea	7A beamline of PLS, Korea
X-ray wavelength (Å)	0.9795	1.0000
Space group	P2 <sub>1</sub> 2 <sub>1</sub> 2	P2 <sub>1</sub> 2 <sub>1</sub> 2
Unit cell parameters		
a, b, c (Å)	106.879, 116.576, 42.666	106.926, 116.620, 42.680
$\alpha$ , $\beta$ , $\gamma$ (°)	90.0, 90.0, 90.0	90.0, 90.0, 90.0
Resolution range (Å)	50.0-2.80	50.0-2.30
Molecules per ASU	2 HicBA homodimers	2 HicBA homodimers
Observed reflections ( $>1\sigma$ )	294526	237881
Unique reflections	23545	24090
$\langle I/\sigma(I) \rangle$	50.69 (6.86) <sup>e</sup>	30.2 (5.27) <sup>e</sup>
Completeness (%)	96.2 (88.8) <sup>e</sup>	99.7 (97.5) <sup>e</sup>
Multiplicity <sup>a</sup>	22.9 (22.8) <sup>e</sup>	9.9 (10.1) <sup>e</sup>
$R_{\text{merge}}$ (%) <sup>b</sup>	11.0 (66.6) <sup>e</sup>	9.2 (53.7) <sup>e</sup>

(b) Refinement statistics

Data set	SeMet	Native
$R_{\text{work}}^{\text{c}}$ (%)	20.2	20.5
$R_{\text{free}}^{\text{d}}$ (%)	24.0	23.6
No. of atoms / average $B$ factor ( $\text{\AA}^2$ )		
Protein	3266 / 55.6	3354 / 40.4
Water oxygen	50 / 50.14	85 / 34.06
RMSD <sup>f</sup> from ideal geometry		
Bond distance ( $\text{\AA}$ )	0.007	0.005
Bond angle ( $^\circ$ )	1.314	0.963
Ramachandran statistics		
Most favoured regions (%)	96.3	98.0
Additional allowed regions (%)	3.2	2.0
Residues in disallowed regions (%)	0.5	0.0
MolProbity score	2.12 (98 <sup>th</sup> percentile)	1.66 (98 <sup>th</sup> percentile)
PDB accession code	-	5YRZ

$$^{\text{a}} N_{\text{obs}}/N_{\text{unique}}$$

$$^{\text{b}} R_{\text{merge}} = \Sigma (I - \langle I \rangle) / \Sigma \langle I \rangle$$

$$^{\text{c}} R_{\text{work}} = \Sigma_{hkl} ||F_{\text{obs}}| - k |F_{\text{calc}}|| / \Sigma_{hkl} |F_{\text{obs}}|$$

<sup>d</sup>  $R_{\text{free}}$  was calculated same way as  $R_{\text{work}}$ , but with the 5% of the reflections excluded from the refinement.

<sup>e</sup> Values in parentheses indicate the highest resolution shell.

<sup>f</sup> Root mean square deviation (RMSD) was calculated with REFMAC.

#### **2.2.4 Size exclusion chromatography coupled with multi-angle light scattering (SEC-MALS)**

MALS was performed to determine the oligomeric states of HicBA. Size-exclusion chromatography was conducted on a BioSep SEC-s3000 column (Phenomenex) on 1260 Infinity HPLC system (Agilent Technologies). The scattering data were obtained in a miniDAWN-TREOS line for emission at 657.4 nm (Wyatt Technology) and analyzed by ASTRA 6.0.1.10 software (Wyatt Technology). HicBA was used at 100  $\mu\text{M}$  in the experiment. HicBA was run in 20 mM Tris, pH 7.5 and 150 mM NaCl as the condition of crystallization. Experiments were performed at room temperature.

#### **2.2.5 Electrophoretic mobility shift assay**

To distinguish the binding affinity of HicB and HicBA to promoter DNA, electrophoretic mobility shift assay (EMSA) was conducted. 28-base pair DNA fragment from the upstream region (promoter DNA) of HicBA was added to proteins as a palindromic form. Palindromic sequence was selected as (forward - TAATAGAATAATAAGTATCACTCCTTTA, reverse - TAAAGGAGTGATACTTATTATTCTATTA) and the annealed dsDNA was

purchased from Bioneer Innovation (<http://www.bioneer.co.kr/>). dsDNA and proteins were prepared in a binding buffer consisting of 20 mM Tris pH 7.5 and 150 mM NaCl. Varying amounts of HicB and HicBA protein were mixed with DNA to give a final volume of 10  $\mu$ l and incubated for 20 min at 4°C. The total binding solutions were loaded onto 0.8% agarose gels in 0.5 x TBE (45 mM Tris-borate, 1 mM EDTA) buffer and the results were visualized using a Gel Doc (Bio-Rad).

### **2.2.6 Isothermal titration calorimetry (ITC) measurements**

ITC experiments were performed using a MicroCal 200 (GE Healthcare) at 25°C. The HicB, HicBA and promoter dsDNA were prepared in a buffer consisting of 20 mM Tris, pH 7.5 and 150 mM NaCl. dsDNA fragment from the upstream region (promoter DNA) of HicBA was added to proteins. Affinity measurement was conducted with the protein solution (0.1 mM, 320  $\mu$ l) in the cell and the promoter dsDNA solution (2 mM) as the injected titrant. 180 s intervals for a total of 19 injections were used for data collection. The MicroCal Origin software was used for curve fitting to calculate the binding affinity ( $K_d$ ), enthalpy of binding ( $\Delta H$ ) and entropy of binding ( $\Delta S$ ) and molar ratio. The raw data were fitted with one-site binding. The Gibbs free energies ( $\Delta G$ ) were calculated by using the standard equation  $\Delta G = \Delta H - T\Delta S$ .

### **2.2.7 NMR study on HicB<sup>109-150</sup> and DNA titration**

NMR spectra of HicB antitoxin were measured through Bruker AVANCE DRX



800 spectrometer. All of experiments were done at 298K and samples were prepared in a buffer of 20 mM Na Pi, pH 7, and 100 mM NaCl containing 10% D<sub>2</sub>O of total volume. Data was processed using NMRPipe / nmrDraw (68) and further analyzed by NMRviewJ (69). The data of carbonyl carbon was obtained through spectrum HNCO and HNCACO, and those of  $\alpha/\beta$  carbon were acquired through the spectrum HNCACB and CBCACONH. Also, to understand the structural transition occurred in specific RHH domain of HicB binding to DNA, promoter DNA was added to HicB<sup>109-150</sup>. DNA titration was conducted four times in the measurement of <sup>1</sup>H, <sup>15</sup>N-HSQC HSQC spectrum. The concentration of HicB was maintained as 1 mM but DNA concentration was varied from 0 to 0.3mM which was 30% of protein concentration. The chemical shift perturbation (CSP) was calculated by nmrViewJ. The average CSP values of <sup>15</sup>N and <sup>1</sup>H were calculated from Equation 1:  $\Delta\delta_N$  and  $\Delta\delta_H$  account for the CSP values of the amide nitrogen and proton.

$$\Delta\delta_{\text{avg}} = [(0.2 \times \Delta\delta_N^2 + \Delta\delta_H^2) / 2]^{1/2} \quad (1)$$

### 2.2.8 *In silico* HicBA-DNA docking

*In silico* molecular docking for the interaction between promoter DNA and HicBA was performed using High Ambiguity Driven protein-protein Docking algorithm (HADDOCK) (134) due to difficulty of having a DNA bound crystal of HicBA. The coordinates for a 28-base pair promoter DNA were modeled using 3D-DART server (135), and coordinates for the HicBA were taken from our crystal structure. The *in silico* chimera models of HicBA hetero-octamer and HicB tetramer were obtained by performing a rigid-body fitting onto the model of HicBA and HicB

structures in *Y. pestis* (PDB code 4P78 and 4C26) (127). The residues of DNA binding domain, inferred from CSP values and two symmetrical grooves of the DNA were defined as ‘active residues’, to generate interface contact. Passive residues were defined automatically as residues around active residues.

### **2.2.9 *In vitro* ribonuclease assay for the addition of peptide mimicking binding region**

Ribonuclease activity of HicA was confirmed using an RNase Alert kit (IDT). Fluorescence quenching assay was carried out following the manufacturer’s protocol. In this system, a fluorophore is covalently attached to one end of a synthetic RNA strand and quenched by a quencher group at the other end. If synthetic RNA containing fluorophore-quencher pair interacts with ribonuclease, synthetic RNA is digested and quencher gets off. Released fluorophore makes fluorescence at 520 nm upon excitation at 490 nm by a fluorometer. The resulting fluorescence (RFU) was observed on a SPECTRAmax GEMINI XS spectrofluorometer. Various concentration range of HicA was examined to prove the ribonuclease activity of HicA and reaction limits. HicA-H36A was examined in same method as HicA to prove indispensability of His36 in ribonuclease activity. Several short peptides that mimic binding region of HicA were designed and purchased from ANYZEN (<http://www.anygen.com>). Peptides were added to HicBA complex to release free HicA (Table 8). The peptide used for regular experiment was ‘ELNKYTERGIRKQAG’. Theoretically, mimicking peptides compete with original protein for binding and if peptides occupy binding, toxin is freely released and makes fluorescence in fluorescence quenching assay (67).

Proteins and peptide used in ribonuclease assay were prepared in 20 mM Tris, pH 7.5 and 150 mM NaCl. The HicBA complex with peptide was incubated at 37°C for 30 minutes before measuring the fluorescence.

**Table 8.** Residues used to create mimicking peptides

Residues (start - end)	Peptide length	Molecular weight
ELNKYTERGIRKQAG (53-67)	15	1,763
GELNKYTERGIRKQAG (52-67)	16	1,820
ELNKYTERGIRKQAGL (53-68)	16	1,876
GELNKYTERGIRKQAGL (52-68)	17	1,933

#### **2.2.10 *In vivo* cell growth assay**

For cell growth assay, the plasmids delivering HicBA, HicA and HicA-H36A were transformed into *E. coli* strain BL21(DE3). Transformed cells from single colonies grown on 0.1 % glucose containing-M9 medium plates were grown overnight and diluted to OD<sub>600</sub> 0.1. Diluted cells were further grown to OD<sub>600</sub> reached 0.4 and 0.5 mM IPTG was added to express proteins. Each cell was incubated at 37°C for 8h after induced by IPTG and monitored at every 1h.

### **2.2.11 *In vivo* HicB neutralization assay**

For the neutralization assay by HicB, mutational approaches toward binding interface of HicBA were conducted. Six residues of HicB (Phe22, Thr33, Gln34, Glu47, Phe80 and Thr89) were mutated to alanine (Table 1). The resulting mutant proteins were designated F22A, T33A, Q34A, E47A, F80A and T89A. Mutations were conducted in same method as HicA-H36A and mutated HicBA complexes were expressed using the same procedures as native HicBA complex. The primers used to create these mutations are described in Table 1. pET28b-HicA along with pET21a-HicB or pET21a-HicB mutants were co-transformed to *E. coli* strain BL21(DE3). Transformed cells were grown in LB plate containing 0.5 mM IPTG. The plates were incubated 37°C for 18h.

### **2.2.12 Circular dichroism (CD) spectroscopy**

CD measurement of 25  $\mu$ M peptides dissolved in 20 mM Tris, pH 7.5 and 150 mM NaCl was performed in Chirascan plus spectropolarimeter (Applied photophysics Ltd) at 20°C, using a 1 mm light path cell. CD scans were taken from 260 nm to 190 nm, with 1 nm bandwidth, and a scan speed of 100 nm/min. Three scans were averaged, followed by subtraction of the solvent signal.

### **2.2.13 Antimicrobial activity test**

Antimicrobial activity was evaluated by serial dilution method measuring Minimum Inhibitory Concentration (MIC) values. The activity of peptide was tested against three strains of Gram-positive (*Bacillus subtilis* ATCC 6633,

*Staphylococcus aureus* ATCC 6538p, *Staphylococcus epidermis* ATCC 12228) and five strains of Gram-negative (*E. coli* ATCC 25922, *Shigella dysenteriae* ATCC 9752, *Salmonella typhimurium* ATCC 14028, *Klebsiella pneumoniae* ATCC 10031, *Pseudomonas aeruginosa* ATCC 27853) bacteria. Each cell strains was grown overnight and incubated with various concentrations of peptide (0.4–100  $\mu$ M). MIC was defined as the lowest peptide concentration that completely inhibits the cell growth. Test was conducted in duplicate.

## 2.3 Results

### 2.3.1 Overall structure of the HicBA complex

The asymmetric unit of the crystal structure of HicBA complex contains two hetero-dimeric HicBA complexes. Two HicB antitoxins and two HicA toxins form a hetero-tetrameric assembly (Figure 22A). However, the calculated molecular weight of HicBA from SEC-MALS was  $105 \pm 0.1$  kDa, which matched the theoretical molecular weight of the hetero-octameric model of HicBA (105.4 kDa) (Figure 23A). By these result, the real oligomeric state in solution is hetero-octamer and inconsistency with crystallographic form might be due to the unit cell length of unique space group. *In silico* model of hetero-octameric assembly of HicBA contains dimeric interfaces of HicB (Figure 22A and Figure 23A). Secondary structure analysis was conducted using 2Struc server (63).

The *S. pneumoniae* HicB antitoxin contains three  $\alpha$ -helices, three  $3_{10}$ -helices ( $\eta$ ) and four  $\beta$ -strands in the following order:  $\beta$ 1 (residues 2–11),  $\beta$ 2 (residues 21–24),  $\beta$ 3 (residues 33–35),  $\alpha$ 1 (residues 38–58),  $\eta$ 1 (residues 69–71),  $\eta$ 2 (residues 92–94),  $\beta$ 4 (residues 96–103),  $\eta$ 3 (residues 104–106),  $\alpha$ 2 (residues 122–130), and  $\alpha$ 3 (residues 135–146). Two antiparallel  $\beta$ -sheets ( $\beta$ 4- $\beta$ 1- $\beta$ 2- $\beta$ 3) wrap the  $\alpha$ 1 helix and the  $\alpha$ 2 and  $\alpha$ 3 helices are followed by long loop after  $\eta$ 3 helix (Figure 22B).

The *S. pneumoniae* HicA toxin contains two  $\alpha$ -helices and three  $\beta$ -strands with a topology of  $\alpha$ - $\beta$ - $\beta$ - $\beta$ - $\alpha$  dsRBD fold. The five secondary structure elements correspond to followings:  $\alpha$ 1 (residues 14–23),  $\beta$ 1 (residues 27–28),  $\beta$ 2 (residues 36–40),  $\beta$ 3 (residues 47–50), and  $\alpha$ 2 (residues 56–66). The  $\beta$ 2,  $\beta$ 3, and  $\alpha$ 2 of the HicA toxin have contacts with a curved back of the HicB antitoxin, made up of  $\beta$ 2,

$\beta 3$ , and  $\alpha 1$  of the HicB antitoxin. (Figure 22B).

In comparison to the structure of *Y. pestis* HicBA complex (127), *S. pneumoniae* HicBA complex structure contains an additional long and flexible loop between  $\eta 1$  and  $\eta 2$  of HicB that the *Y. pestis* HicBA complex does not show (Figure 24D). This loop covers more than 20 residues of the HicB (Figure 22B). In particular, the structure C-terminal region of HicB is missing in the structure of *Y. pestis* HicBA complex, which is expected to be DNA-binding domain (128) (Figure 22C). Structural topologies of two HicBA complex is described in Figure 25A–B. DNA binding domain of Type II antitoxin is important in auto-regulation of TA operon (52). Furthermore, DNA binding domain of the HicBA system was determined as RHH by NMR studies. In summary, the structure of *S. pneumoniae* HicBA complex is the first structure showing entire conformation of the HicBA TA system, which can show biological meaning of the HicBA system.

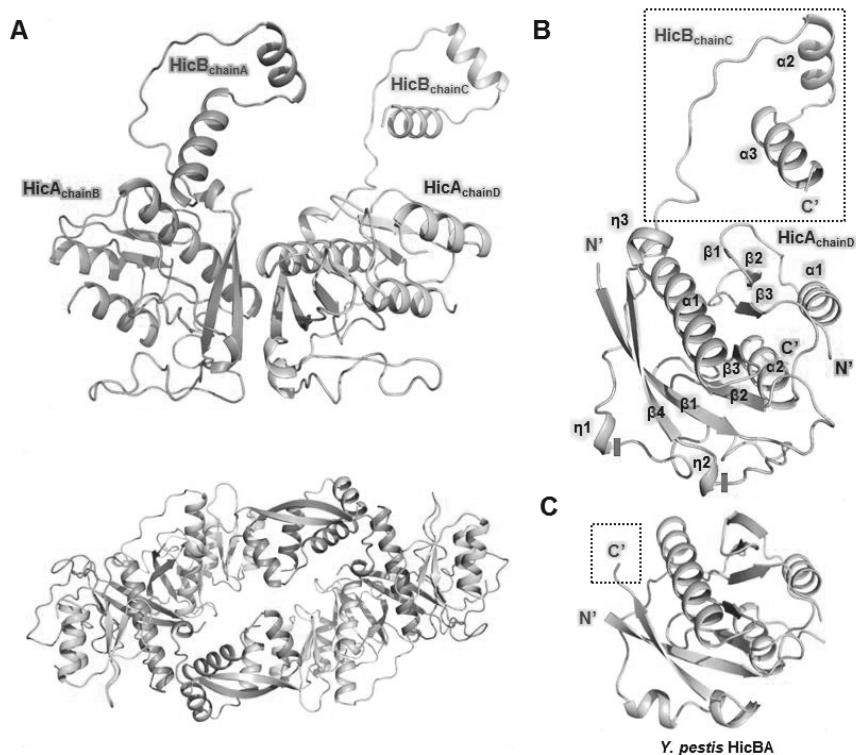


**Figure 22.** Overall structures of HicBA. (A) Upper: Ribbon representation of the HicBA hetero-tetramer. Chains A and C of HicB are shown in purple and chains B and D of HicA are shown in cyan, respectively. Lower: *In silico* model of HicBA hetero-octamer. The model contains dimeric interfaces of HicBs. (B) Structure of the HicBA heterodimer. Start and end of long and flexible loop between  $\eta 1$  and  $\eta 2$  of HicB are marked as red color bar. (C) The structure of *Y. pestis* HicBA complex. (B and C) Entire DNA binding region of C-terminus of HicB is only observed in the structure of *S. pneumoniae* HicBA complex in the black dotted square. The structure of *Y. pestis* HicBA complex lacks C-terminal region of HicB.



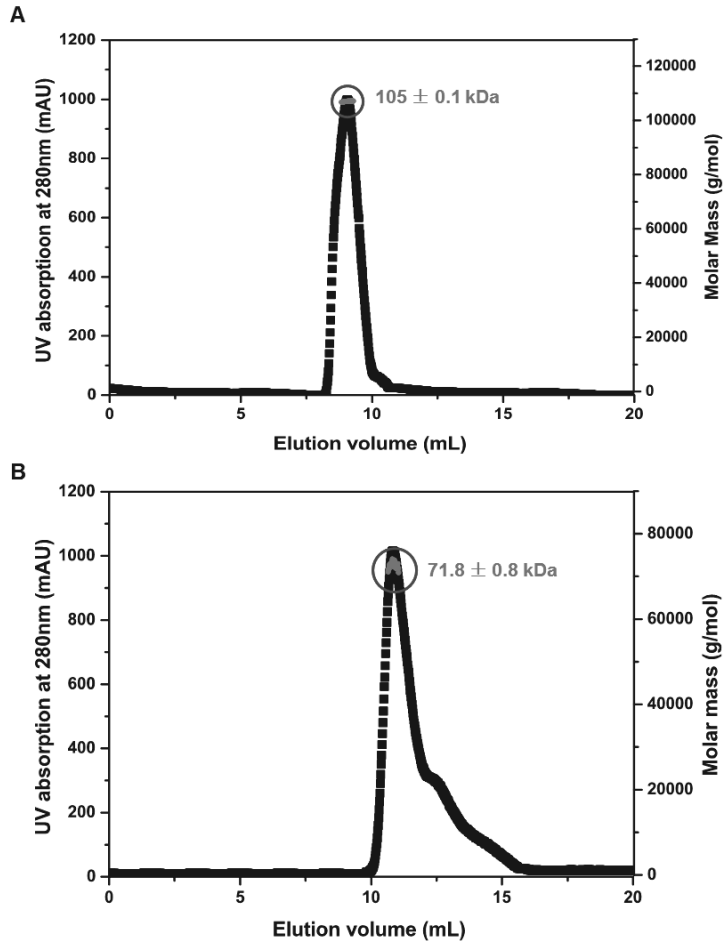


**Figure 23.** Size-exclusion chromatography (SEC)-MALS chromatograms showing the oligomeric states of HicBA and HicB in solution. The UV absorption at 280 nm (left axis, black line) and the calculated molecular weight (right axis, red line) are plotted as a function of the elution volume. The numbers next to the blue circled peak indicate the average molecular weight obtained using MALS. **(A)** HicBA was anticipated to exist as hetero-octamer and **(B)** HicB was anticipated to exist as a tetramer in solution. **Figure 22A** and **Figure 24B** show the *in silico* model of these results.

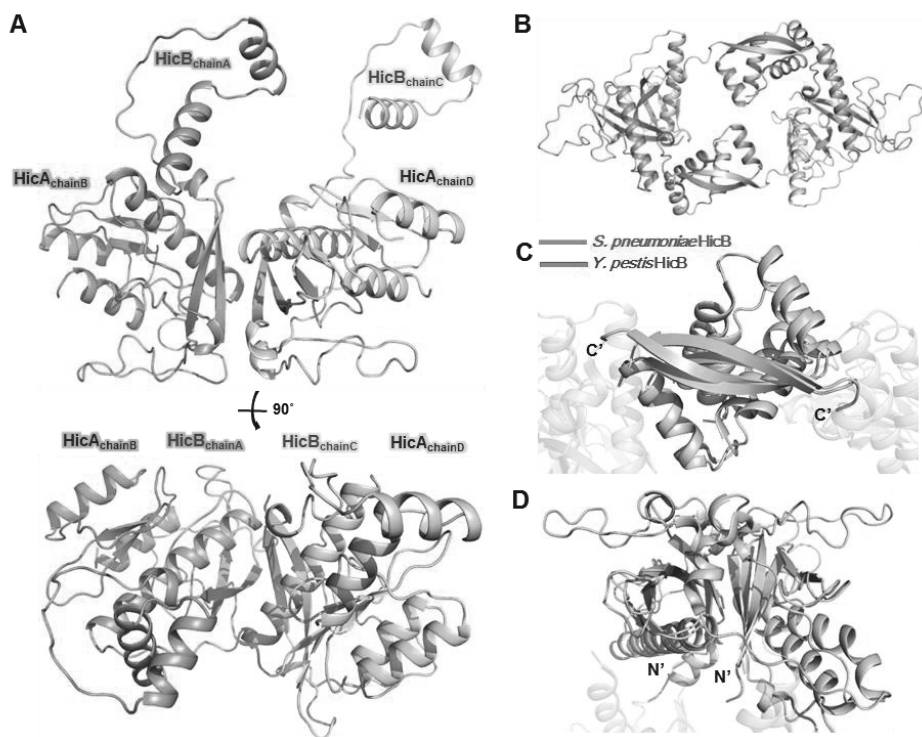


**Figure 24.** (A–B) Overall structures of HicBA and HicB. (A) Ribbon representation of the HicBA hetero-tetramer and 90° rotated diagram. Chains A and C of HicB are shown in purple and chains B and D of HicA are shown in cyan, respectively. (B) *In silico* model of HicB tetramer. The model contains two different dimeric interfaces in N terminus and C terminus. (C–D) Structural comparisons between tetrameric structures of *S. pneumoniae* HicB (magenta) and *Y. pestis* HicB (green). (C) C-terminal dimerization interface. (D) N-terminal dimerization interface. The N-terminal interface of *S. pneumoniae* HicB revealed a flexible loop that does not exist in *Y. pestis* HicB.

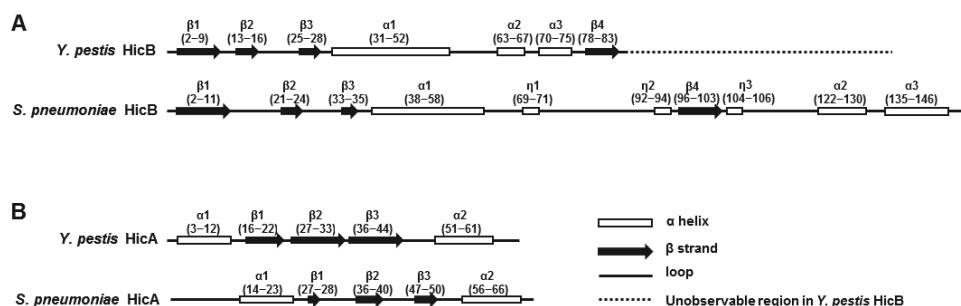


**Figure 25.** Secondary structure topologies of *Y. pestis* HicBA (PDB code 4P78) and *S. pneumoniae* HicBA. **(A)** Secondary structure topologies of HicBs. *S. pneumoniae* HicB contains an additional long and flexible loop between  $\eta 1$  and  $\eta 2$  of HicB that the *Y. pestis* HicBA complex does not show. The structure of *Y. pestis* HicB lacks C-terminal region of HicB, which is expected to be DNA-binding domain. **(B)** Secondary structure topologies of HicAs. They adopt  $\alpha$ - $\beta$ - $\beta$ - $\beta$ - $\alpha$  dsRBD fold.

### 2.3.2 The structural distinctions of HicB antitoxin

Two HicB antitoxins form a homodimer through their N-terminal domain, mainly by  $\beta 1$ ,  $\alpha 1$ , and  $\beta 4$  from each HicB monomer. However, the calculated molecular weight of HicB from SEC-MALS was  $71.8 \pm 0.8$  kDa, which matched the theoretical molecular weight of the tetramer model of HicB (71.3 kDa) (Figure 23B). *In silico* model of HicB tetramer contains additional C-terminal dimeric interface as well as N-terminal interface. (Figure 24B–C). The average area of the N-terminal dimeric interfaces is 601.9 Å<sup>2</sup>. Interface area was calculated using PISA server (64). This binding is achieved through both hydrophobic interactions and

hydrogen bonding networks. Hydrophobic interactions are mediated by seven residues: Leu2 on  $\beta$ 1, Ile38/Leu42/Ala43 on  $\alpha$ 1, Ile69 on  $\eta$ 1, and Phe96/Met99 on  $\beta$ 4. Met99 participates in multiple hydrophobic interactions with Ile38, Leu42, and Phe96 (Figure 26A).

In addition, hydrogen bonding networks are mediated by another seven residues: Thr4 on  $\beta$ 1, Ser39 on  $\alpha$ 1, Asn70 on  $\eta$ 1, Asp93 on  $\eta$ 2, Ser95 on the loop connecting  $\eta$ 2 and  $\beta$ 4, and Ser98/Met99 on  $\beta$ 4. The main chain O atoms of Asp93 and Ser95 act as an acceptor for hydrogen bonding with the N $\delta_2$  atom of Asn70 in the  $\eta$ 1 helix. The side chain O $\gamma$  atom of Ser98 accepts proton from N atom of Met99 and equivalent residue of proximal antitoxin. Thr4 and Ser39 also form hydrogen bond through their side chain atom O $\gamma_1$  and O $\gamma$  (Figure 26A). Met99 supports dimerization by both hydrophobic interactions and hydrogen bonding networks.

Interestingly, there is a considerable structural deviation in the C-terminal domain of two HicB antitoxins, chain A and chain C. The HicB antitoxin consists of N-terminal fixed domain (residues 3–106), bending region (residues 107–112), and C-terminal moving domain (residues 113–145). The rotation angle of two moving domains of the chain A and chain C is 151.3°. The root mean square deviation (r.m.s. deviation) value of two fixed domains was 0.81, but 10.63 for whole proteins, because of the flexibility of moving domains. The fixed, bending and moving domains, rotation angle, and r.m.s deviation values were identified by the *DynDom* database (136) (Figure 26B). The r.m.s deviation of moving domains of Chain A and C was 0.51. These two moving domains show the difference orientation because of domain rearrangement. As the binding interfaces of HicB and HicA from chain A and C are almost same, it can be described that these moving domains have close relation with oligomeric state of HicBA in solution achieved by

dimerization of HicB. Notably, the region of expected DNA-binding domain and flexible moving domain are matched. This shows that flexible nature is crucial in their role in DNA binding (89).

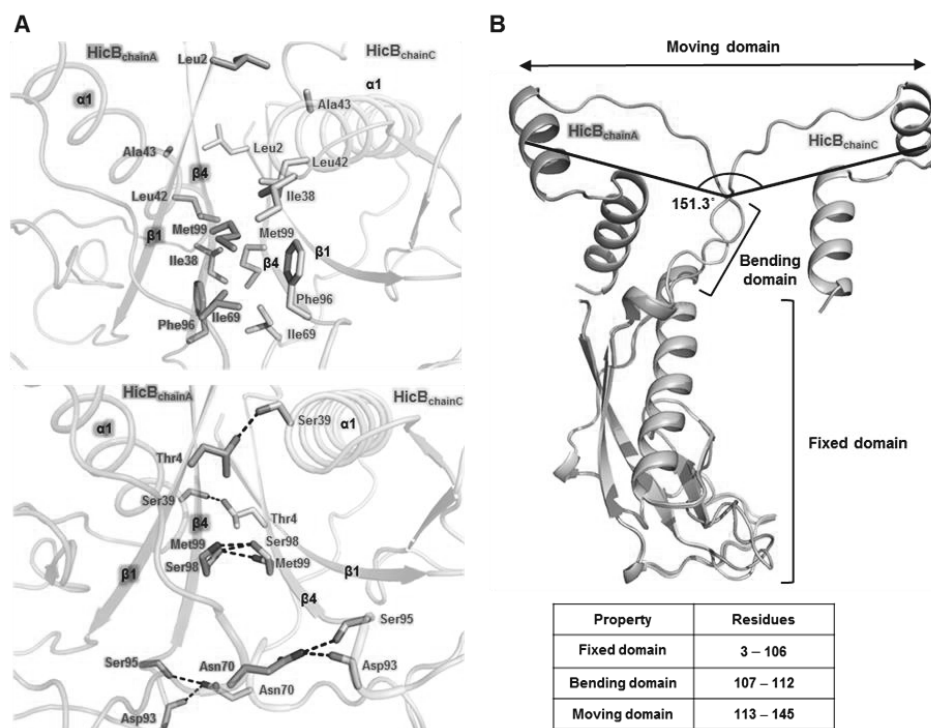


**Figure 26.** Structural features of the HicB dimer. **(A)** Details of the homodimeric interface of the HicB antitoxin between chains A and C. Upper: the residues involved in hydrophobic interactions. Residues participating in hydrophobic interactions are shown as stick models. Lower: the residues involved in hydrophilic interactions. Hydrogen bonds are shown as black dotted lines. **(B)** Structural deviation in the C' terminal domain of two HicB antitoxins. The fixed, bending and moving domains, and rotation angle are indicated.

### 2.3.3 Characterization of the interaction with promoter DNA

To confirm the DNA-binding properties of HicB and HicBA, EMSA experiment was conducted. Although we could not obtain the dissociation constant by EMSA experiment, the binding-preference magnitudes of HicB and HicBA were identified based on the results. The concentration of DNA was fixed at 0.01 mM and the concentration of proteins was increased from 0 to 0.8 mM. As DNA binds to large amount of proteins gradually, the bands of DNA-protein complex shifted upward. (Figure 27A). EMSA shows that DNA binds to both HicB antitoxin and HicBA complex, exhibiting slight better affinity with HicBA than HicB.

Isothermal titration calorimetry (ITC) experiments were used to estimate the binding affinity of HicB and HicBA for the promoter DNA (Figure 27B). The promoter DNA-binding reaction of HicB is endothermic and entropically driven, with thermodynamic parameters of  $4.30 \pm 0.39 \text{ kcal mol}^{-1}$  ( $\Delta H$ ) and  $33.3 \text{ cal mol}^{-1} \text{ deg}^{-1}$  ( $\Delta S$ ), and the equilibrium dissociation constant ( $K_d$ ) was measured as  $8.82 \pm 1.06 \text{ }\mu\text{M}$  for the binding of HicB to DNA. The binding stoichiometry ( $n$ ) is  $0.51 \pm 0.02$  for one HicB dimer per DNA duplex. Experimental values show that HicB tetramer interacts with dsDNA. The promoter DNA-binding reaction of HicBA is endothermic and entropically driven, with thermodynamic parameters of  $6.54 \pm 0.46 \text{ kcal mol}^{-1}$  ( $\Delta H$ ) and  $44.6 \text{ cal mol}^{-1} \text{ deg}^{-1}$  ( $\Delta S$ ), and the equilibrium dissociation constant ( $K_d$ ) was measured as  $4.18 \pm 0.44 \text{ }\mu\text{M}$  for the binding of HicBA to DNA. The binding stoichiometry ( $n$ ) is  $0.47 \pm 0.03$  for one HicBA hetero-tetramer per DNA duplex. Experimental values show that HicBA hetero-octamer interacts with dsDNA. The results show that HicBA complex has better affinity with DNA than HicB based on  $K_d$  values. Calorimetric trials were also performed in the absence of

proteins under the same experimental conditions. No change in heat was observed in the injections throughout the experiment.

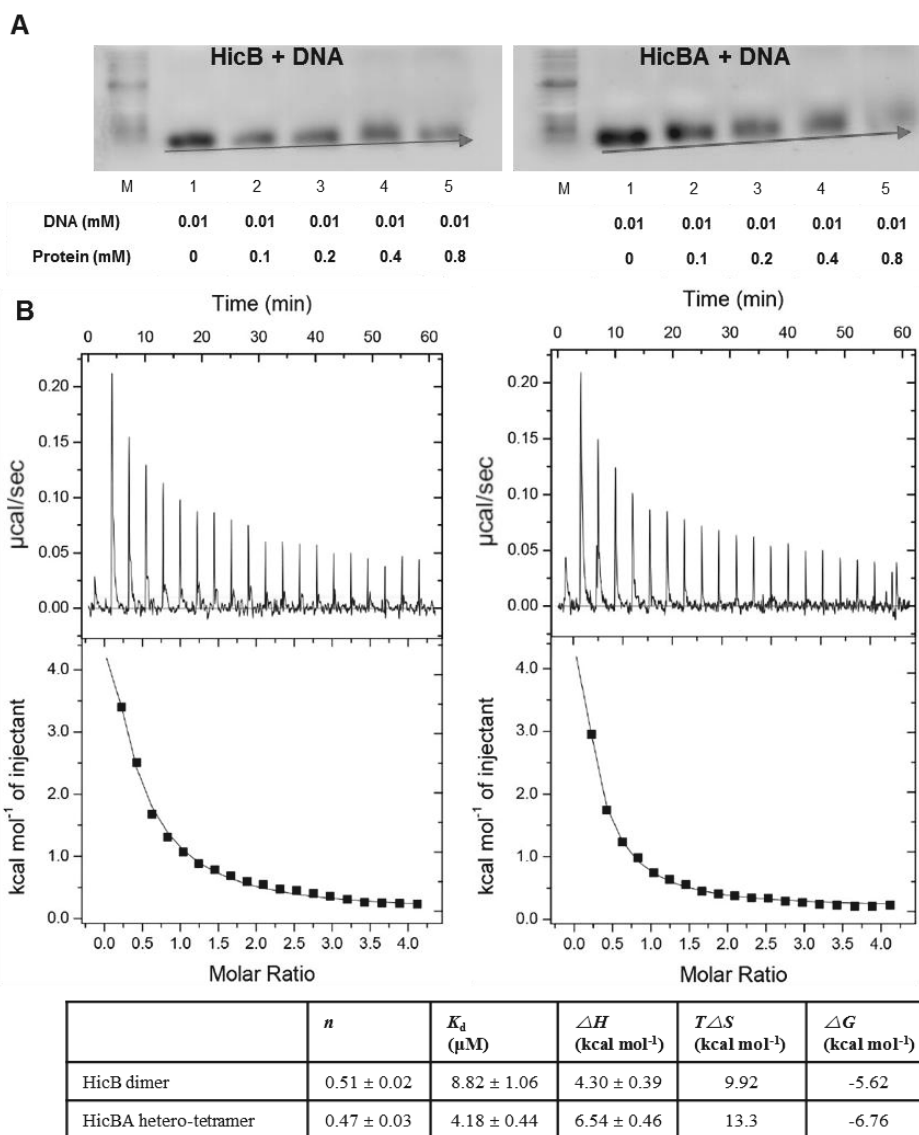


**Figure 27.** DNA binding properties determined from EMSA and ITC assay. **(A)** Left: EMSA experiment between HicB and DNA. Light: EMSA experiment between HicB and DNA. The details of the concentrations of protein and DNA in the lanes are indicated. The red arrows indicate gradual creation of DNA-protein complex at various ratios. As DNA binds to large amount of proteins gradually, the bands of DNA-protein complex move upward. **(B)** ITC assay of HicB (left) and HicBA (right) with the promoter DNA. The binding curve of titration indicates that HicB and HicBA are capable of binding to its upstream promoter DNA. Binding parameters are described in table (lower).

### 2.3.4 DNA-binding domain of HicB

In type II TA systems, the antitoxin alone or in complex with toxin typically interacts with its corresponding promoter DNA, repressing the transcription of the TA operon (52). Therefore, the DNA-binding properties of the antitoxin are important for the regulation of TA systems. We characterized the interactions between specific residues in HicB and the promoter DNA using NMR titration experiments. For this experiment, HicB<sup>109-150</sup> was used because of poor spectrum quality of full length of HicB (Figure 28A).

We predicted the possible DNA-binding domain of HicB and conducted backbone assignment of the HicB<sup>109-150</sup> except for Pro113 and Pro121. The secondary structure of HicB<sup>109-150</sup> in solution was derived from the program TALOS+ (78) using the assigned chemical shift values (Table 9). Predicted conformation of HicB<sup>109-150</sup> includes one  $\beta$ -strand and two  $\alpha$ -helices in the following order:  $\beta$ 1 (residues 114–119),  $\alpha$ 1 (residues 122–130),  $\alpha$ 2 (residues 135–145). This is highly consistent with that of the structure of HicB in the HicBA



complex. The oligomeric state of HicB<sup>109-150</sup> seems likely to be dimer because of lacking N-terminal dimerization domain.

We compared the HSQC spectra of HicB<sup>109-150</sup> (1 mM) in the absence and presence of increasing concentrations of promoter DNA (0 to 0.3 mM). These comparative spectra are shown as an overlay in Figure 29A. Upon titration with DNA, the spectra of HicB<sup>109-150</sup> showed peak shift. The peak shifts observed in the spectra indicate that the HicB<sup>109-150</sup>-DNA interaction is achieved in a fast exchange on the NMR time scale, which is typically observed when molecules bind with a low to moderate affinity. The results of the titration experiment were consistent with the ITC data. According to the  $K_d$  determined in the ITC experiment, the binding between HicB and DNA is not strong; thus, the binding mode between HicB<sup>109-150</sup> and DNA is expected to show fast exchange. This result is highly consistent with the observed peak movements in the spectra of HicB<sup>109-150</sup> titrated with DNA.

Based on the assigned backbone <sup>1</sup>H and <sup>15</sup>N resonances, we monitored the residues showing changes in the chemical shifts upon binding to DNA. We calculated the combined <sup>1</sup>H and <sup>15</sup>N chemical shift perturbation (CSP) values of HicB<sup>109-150</sup> in the presence of 0.3 mM DNA using equation 1 shown in the Materials and Methods section to quantify the peak shifts. These values are plotted as a function of HicB<sup>109-150</sup> residues (Figure 29B). The CSP values of the residues belonging to the  $\alpha$ 2 helix and C-terminus were large. Residues in the N-terminus of the  $\alpha$ 2 helix (Phe135 and Gln137) and C-terminus (Val148 and Gln149) exhibited significant changes in their chemical shifts. Residues in the  $\beta$ 1 strand showed relatively small CSP values than other secondary structure component because hydrogen bonds between  $\beta$  strands of HicB dimer hinder the large conformational

changes (137). Based on these CSP data, we characterized the DNA-binding region of HicB<sup>109-150</sup> as RHH motif. The regions showing relatively large CSP values are mapped onto the surface representation of HicB<sup>109-150</sup> in Figure 29C. Additionally, as a result of additional titration,  $K_d$  for the binding of HicBA<sup>109-150</sup> to DNA was measured as  $4.54 \pm 1.13 \mu\text{M}$ , which is comparable to the value of  $K_d$  calculated from ITC (Figure 28B).

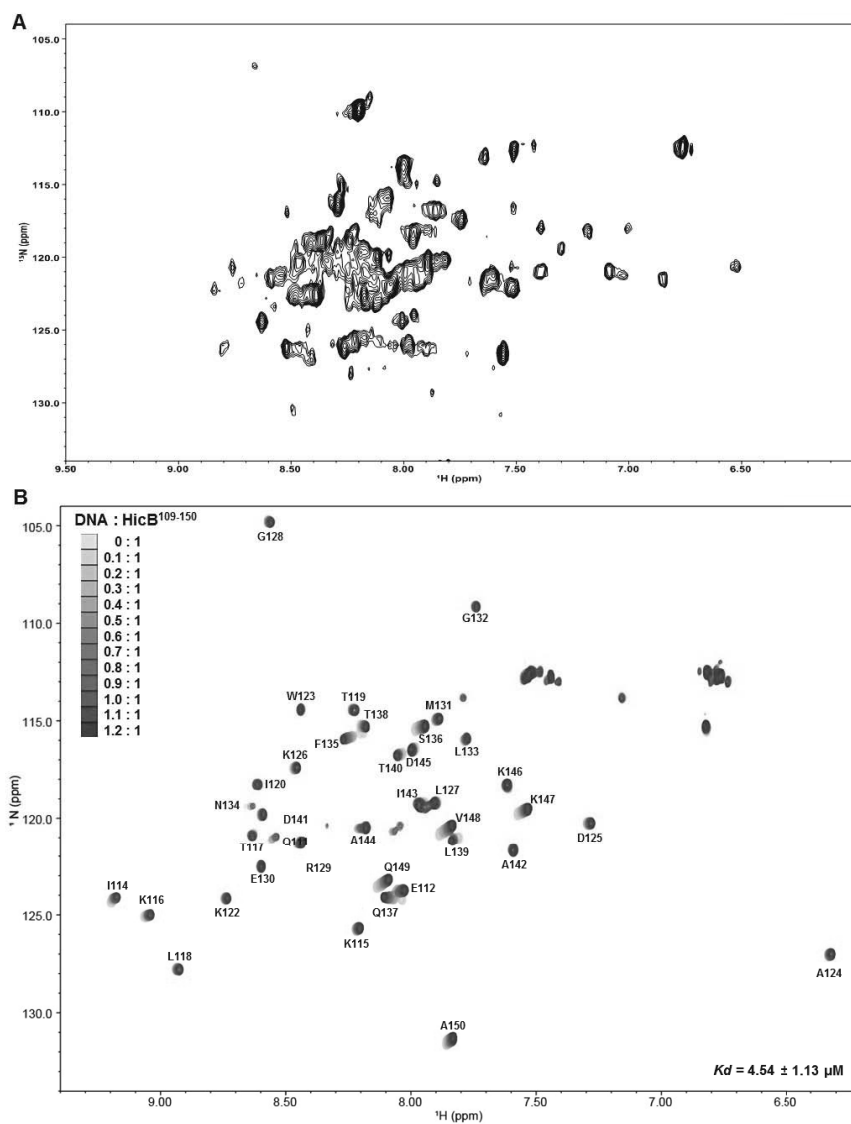


**Figure 28.** (A) 2D  $^1\text{H}$ - $^{15}\text{N}$  HSQC spectrum of full-length HicB. Buffer condition and concentration of protein were same as HicB<sup>109-150</sup>. (B) The superposition of HicA homologs. Each molecule is marked with different colors as described in right. The residues essential in activity are highlighted in yellow circle.

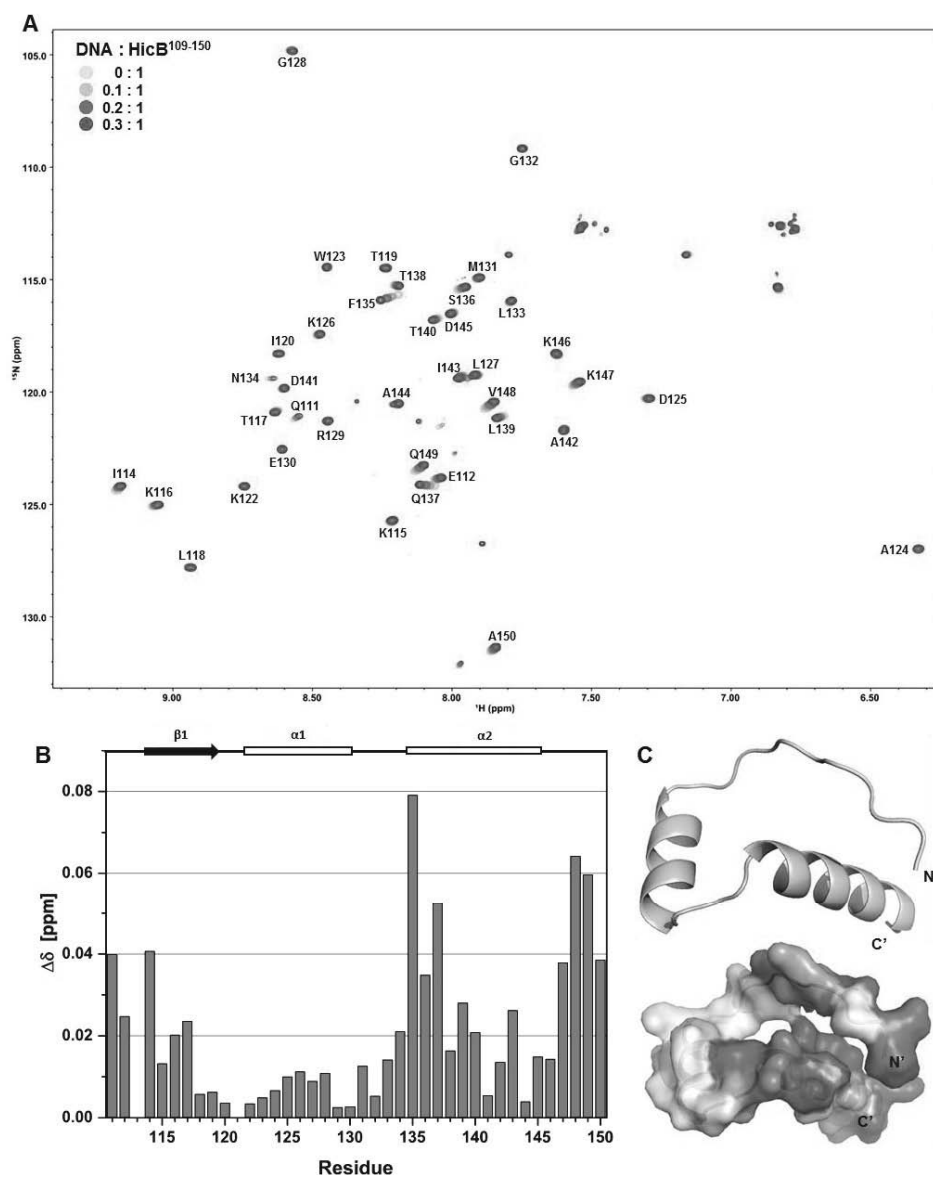


**Figure 29.** NMR titration of HicB<sup>109-150</sup> and its promoter DNA. **(A)** Overlay of 2D <sup>1</sup>H-<sup>15</sup>N HSQC spectra of 1 mM HicB<sup>109-150</sup> with increasing ratios of added DNA. The peaks are colored with a gradient indicating the addition of DNA. **(B)** The chemical shift perturbation of each residue in the presence of 0.3 mM promoter DNA. **(C)** Upper: The structure of HicB<sup>109-150</sup> in the HicBA complex. Lower: Surface representation of HicB<sup>109-150</sup> mapped with CSP values. The residues are colored with getting darker in color indicating their CSP values.

**Table 9.** Predicted secondary structures with confidence scores offered by Talos based on the backbone-assigned amino acid sequence of HicB<sup>109-150</sup>

Sequence										G	S	Q	E	P	I	K	K	T	L
Predicted secondary structure										X	L	L	L	L	E	E	E	E	E
Confidence score										0	0	7	8	6	4	7	7	8	7
T	I	P	K	W	A	D	K	L	G	R	E	M	G	L	N	F	S	Q	T
E	L	L	H	H	H	H	H	H	H	H	H	L	L	L	L	H	H	H	H
4	6	7	3	4	2	7	8	7	7	8	6	4	9	9	8	3	8	8	9
L	T	D	A	I	A	D	K	K	V	Q	A								
H	H	H	H	H	H	H	L	L	L	L	L								
9	9	9	9	9	8	2	6	8	5	1	0								

H = helix, E = strand, L = coil, X = unassigned residues.

Confidence is scored from 0 (low) to 9 (high).

### 2.3.5 The active site of the HicA and ribonuclease activity dependent on His36

The type II toxins usually show ribonucleic activity and require essential residues to organize an active sites in the VapBC, RelBE, MazEF, and PezAT systems (138). To clarify the active site of the HicBA system, Sequence alignment were performed using Clustal Omega 1.2.1 (65) and visualized using ESPript 3.0 (66) (Figure 30). The sequence of *S. pneumoniae* HicA was aligned with the hypothetical protein from *Thermus thermophiles*, the HicA toxin from *Y. pestis*, the HicA toxin from *Burkholderia pseudomallei*, and the HicA toxin from *Escherichia coli*. The results show that highly conserved histidine residue in the  $\beta 2$  strand and Glycine residue in the loop between  $\beta 1$  and  $\beta 2$ , corresponding hydrogen bonded turn. For a detailed comparison, the structural similarity of proteins was analyzed using DALI (70), except *E. coli* HicA, of which structure has not been reported.

The structural homologues include (i) the hypothetical protein from *T. thermophiles* [PDB code 1WHZ (chains A) with an r.m.s. deviation of 1.5 Å, Z-scores of 9.0 and a sequence identity of 29%], (ii) the HicA toxin from *Y. pestis* (127) [PDB code 4P78 (chains C and D) with r.m.s. deviations of 1.6-1.7 Å, Z-scores of 7.7-8.6 and a sequence identity of 34%], and (iii) the HicA toxin from *B. pseudomallei* (131) [PDB code 4C26 (chains A) with r.m.s. deviations of 2.3 Å, Z-scores of 5.7 and sequence identities of 28%] (Figure 31).

In the active site of the *S. pneumoniae* HicA, the key residue His36 closely interacts with Thr33 and Glu47 of the HicB antitoxin. The O $\eta_1$  atom of Thr33 and the O $\epsilon_1$  atom of Glu47 form hydrogen bond with the N $\epsilon_2$  atom and N atom of key residue. In addition, O $\epsilon_1$  atom of the Glu47 highly stabilizes the active site by

forming salt bridge with the N $\delta_1$  atom of key residue. Intra-protein hydrogen bond is also observed between N atom of key residue and the O atom of Lys33 in the HicA (Figure 32).

The *S. pneumoniae* HicA forms dsRBD (129) to bind to RNA substrates. The HicA not only binds to RNA substrates, but also cleaves the RNA substrates as ribonuclease toxin (130). We performed RNA activity assays for HicA using fluorescent RNA substrates. If the substrates are cleaved, they emit fluorescence in proportion to the amount of the substrate cleaved by HicA. The ribonuclease activity of the *S. pneumoniae* HicA is confirmed by the increase of RFU as a function of the increasing concentration of protein from 1  $\mu$ M to 8  $\mu$ M (Figure 32B). At the concentration greater than 8  $\mu$ M, reaction is saturated. HicA-H36A does not show any ribonuclease activity due to the loss of key residue. When compared to other toxin molecules having ribonuclease activity (VapC26 and VapC30 from *M. tuberculosis*), HicA showed the highest activity (Figure 32C).

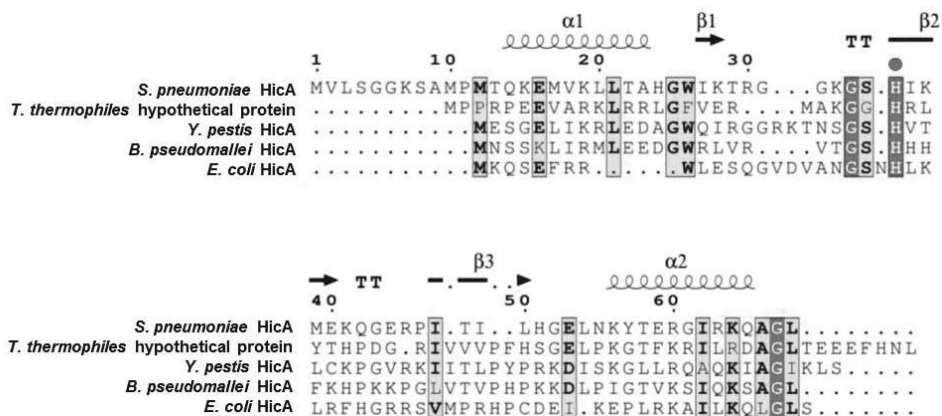


**Figure 30.** Sequence alignment of the *S. pneumoniae* HicA with sequence homologs. Proteins are listed in order of structural homology with *S. pneumoniae* HicA. The known secondary structure elements of the proteins are shown above the alignment. Identical and similar residues are highlighted in red and yellow, respectively. Conserved residue, which is essential for ribonucleic activity is indicated by a red circle.



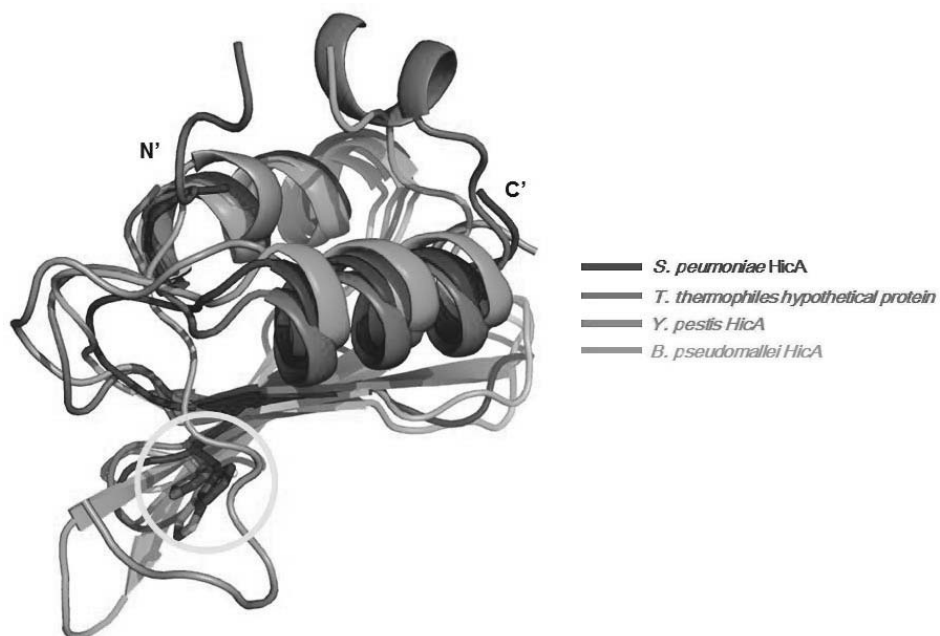


**Figure 31.** The superposition of HicA homologs. Each molecule is marked with different colors as described in right. The residues essential in activity are highlighted in yellow circle.

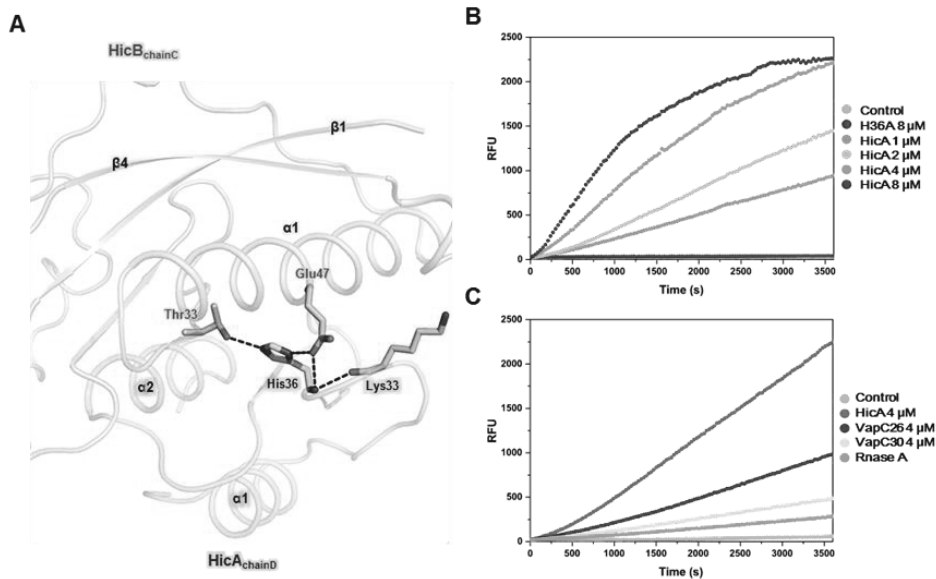


**Figure 32.** Active site structure of *S. pneumoniae* HicA and *in vitro* ribonuclease activity assay. **(A)** Active site with nearby interacting residues. Hydrogen bonds and salt bridge are shown as black dotted lines. **(B)** Upper: Fluorescence measurements, as a function of time, increasing addition of the HicA. Various concentrations of the HicA were prepared and at the concentration greater than 8 μM, reaction was saturated. The proteins having alanine mutated from histidine (H36A) showed negligible activity on the cleavage of the RNA molecule compared to HicA. **(C)** Ribonuclease activity comparison of *S. pneumoniae* HicA with other toxin molecules and RNase A. **(B and C)** 40 units of RiboLock™ (Thermo Scientific) RNase inhibitor were used to prevent contamination. The control contained 20 mM Tris, pH 7.5 and 150 mM NaCl, and 40 units of RiboLock™ (Thermo Scientific) RNase inhibitor. Each experiment was performed in triplicate.  $3 \times 10^{-5}$  units of RNase A was also used in comparison.

### 2.3.6 Intermolecular interactions between HicB and HicA related to toxicity

The HicB antitoxin blocks the enzymatic function of the HicA toxin by forming toxin-antitoxin protein complex. The HicB covers 1,183 Å<sup>2</sup> of the HicA to neutralize the toxicity of HicA. Approximately, 43 % residues of whole HicA toxin chain D participate in this interaction and interface area occupies about 28 % of total surface area of HicA.

In this interface area, hydrophobic interactions are contributed by Phe22, Met44, Phe80, Phe86, and Tyr90 of the HicB, and Leu50 and Tyr57 of the HicA. Aromatic interactions derived from Tyr57 of the HicA are major in hydrophobic interaction (Figure 33A). The residues involved in hydrophilic interactions in the HicB are Asp12/Ala19/Tyr30/Thr33/Gln34/Glu47/Thr89/Glu106/Gln111, which interact with Arg30/Lys33/Ser35/His36/Lys38/Glu53/Asn55/Lys56/Tyr57/Thr58/Gln65 in the HicA. Additional salt bridges are formed by Asp12, Glu47, Asp55, and Asp83 of the HicB, and His36, Lys38, Lys56, and Lys64 of the HicA (Figure 33B). The whole hydrophilic networks are presented in schematic diagram.

To verify the key binding residues that are essential for the interaction between HicB and HicA, six residues of HicB were mutated to alanine based on interaction analysis in Figure 33A–B. Four residues occupying hydrophilic interaction with multiple counterparts of HicA (Thr33, Gln34, Glu47 and Thr89) and the other two residues involved in hydrophobic interaction (Phe22 and Phe80) were selected. Among the mutated HicBA complex, HicA complexed with HicB-E47A showed decreased growth of *E. coli*, suggesting that mutation of Glu47 resulted in a loss of interaction between HicB and HicA. The *E.coli* cells containing HicA-HicB-E47A

produced far less colonies than *E.coli* cells containing native HicBA complex (Figure 33C).

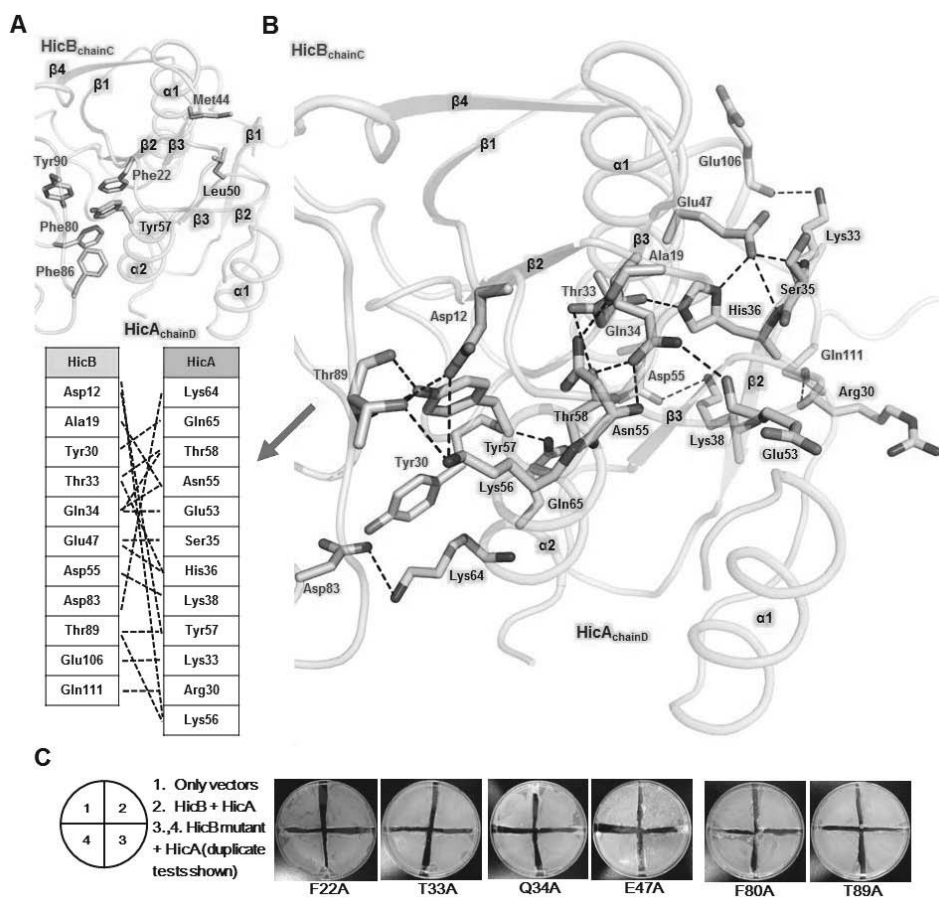


**Figure 33.** Heterodimeric interface of HicB and HicA, and mutations affecting toxicity. **(A)** Range of hydrophobic forces mainly contributed by Tyr57 of the HicA. **(B)** The residues involved in hydrophilic interactions. Hydrogen bonds and salt bridges are shown as black dotted lines. Schematic diagrams of the hydrophilic

interactions, indicated by red arrow from **Figure 33B** are presented. **(C)** Effects of mutations of interacting residues between HicB and HicA to *E. coli* cells growth. Mutated complexes were induced by IPTG to identify the toxicity to *E. coli* cells. Upper two quadrants indicate the empty vectors and native HicBA complex. Decreased colonies at lower quadrants indicates revived activity of mutated HicBA complex.

### **2.3.7 Artificial toxin activation and cell growth inhibition by HicA**

We designed mimicking peptides as inhibitors of the interaction between HicB and HicA. The peptide mimics the binding interface of HicA. Theoretically, these mimicking peptides compete with the HicA, thus hindering the formation of the TA complex. If the peptide shows high affinity to the HicB, free HicA would be more predominant, resulting in increased RNase activity (67). The data for regular figure was taken from the peptide 'ELNKYTERGIRKQAG', based on activity comparison with other candidates (Figure 34A–B). Chosen peptide contains 11 residues of the  $\alpha 2$  helix of HicA (KYTERGIRKQA) and 11 residues of interface residues of HicA and HicB underlined. Peptides mimicking the helix are preferred because of its resistance against proteolytic degradation (139). Modeled helix should not be divided because of the membrane affinity and selectivity. Also, optimal length of helix should be modeled to prevent loss of selectivity and self-aggregation (140). Circular dichroism spectra of peptides were collected and the peptide 'ELNKYTERGIRKQAG' showed highest degree of helicity (39.84%). The helical content of each peptide was quantitatively measured based on the mean residue ellipticity,  $[\theta]_{222}$  (141) (Figure 34C).

Designed mimicking peptide includes the whole  $\alpha 2$  helix of HicA and contains

seven residues (Glu53, Asn55, Lys56, Tyr57, Thr58, Lys64, Gln65) engaged in interactions with HicB. In the results, peptide disrupts the interaction of HicBA complex, up to 80 % (Figure 35A and B). RFU for peptide concentration greater than 16  $\mu$ M did not show a remarkable difference from that of 16  $\mu$ M.

Cell growth assay demonstrated growth arrest ability of HicA and toxicity loss of HicA-H36A (Figure 35C). *E. coli* cells expressing HicA showed decreased OD<sub>600</sub>, after 2h from induction. Cells expressing HicA-H36A grew in same rate as control cells.

Antimicrobial activity of mimicking peptide is summarized in Figure 35D. The peptide exhibited detectable activities against certain bacterial species. The strongest activities against both Gram-positive and Gram-negative bacteria were smallest MIC value of 6.3  $\mu$ M.

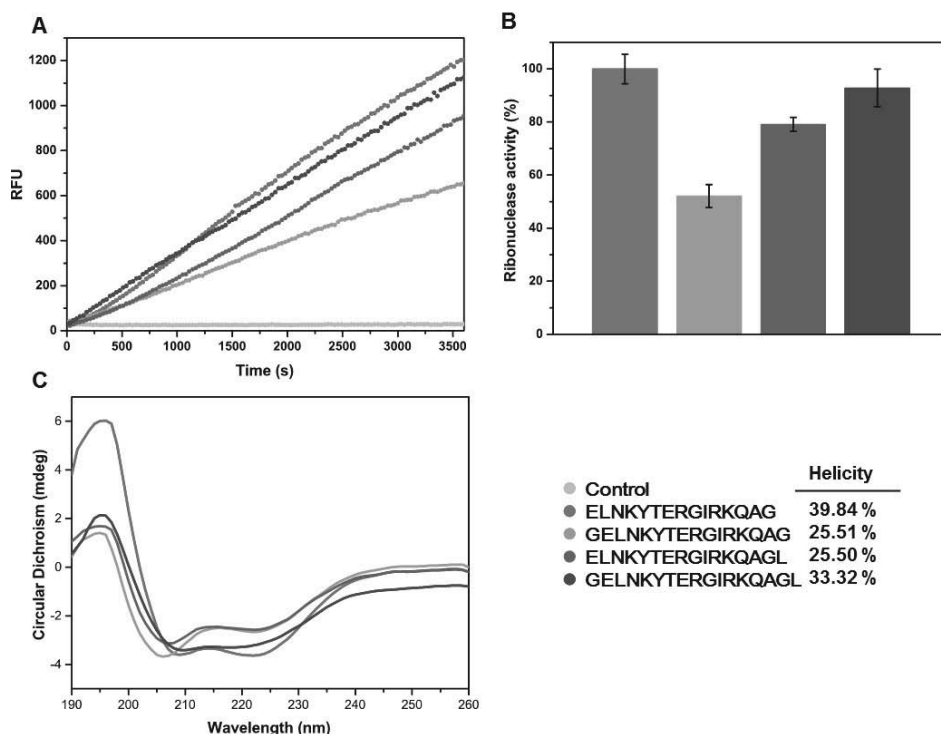


**Figure 34.** Several initial tests of peptides. The colors of lines and bars in this figure are corresponding to index of lower right quadrant. **(A)** The test of the RNase activity of *S. pneumoniae* HicBA in the presence of four peptides. 4  $\mu$ M of peptides were added to the 4  $\mu$ M of HicBA. The control contained 20 mM Tris, pH 7.5 and 150 mM NaCl , and 40 units of RiboLock™ (Thermo Scientific) RNase inhibitor. Each experiment was performed in triplicate. **(B)** Statistical representation of **Figure 34A**. RFU obtained by the 4  $\mu$ M HicAB + 4  $\mu$ M ‘ELNKYTERGIRKQAG’ was taken as 100%. Error bars represent the standard deviation of three replicate reactions. **(C)** Circular dichroism spectra of the peptides in a 20 mM Tris, pH 7.5 and 150 mM NaCl at 20 °C. Helicities of peptides are expressed next to the peptide index.

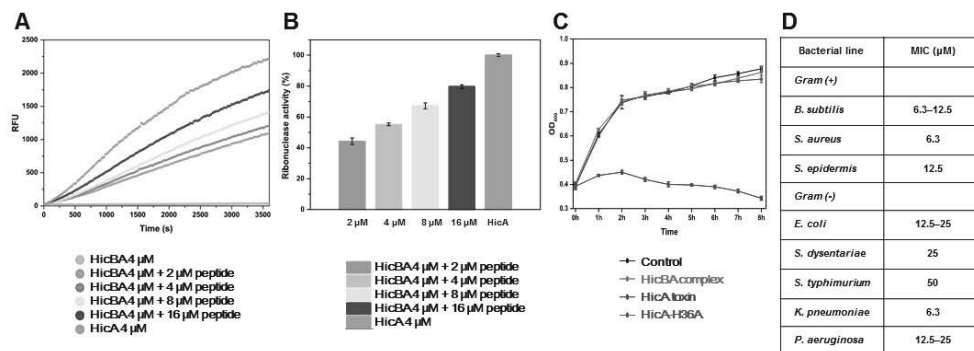


**Figure 35.** Ribonuclease activity of *S. pneumoniae* HicBA measured using a HicA  $\alpha 2$ -mimicking peptide and Cell growth inhibition activity of HicA toxin and mimicking peptide. **(A)** The concentration of HicBA was fixed at 4  $\mu\text{M}$ , and the concentration of peptide increased from 2  $\mu\text{M}$  to 16  $\mu\text{M}$ . The peptide inhibited the binding of HicB to HicA by approximately 80% at 16  $\mu\text{M}$ . 40 units of RiboLock<sup>TM</sup> (Thermo Scientific) RNase inhibitor were used to prevent contamination. Each experiment was performed in triplicate. **(B)** Statistical representation of **Figure 35A**. RFU obtained by the 4  $\mu\text{M}$  HicA was taken as 100%, and 4  $\mu\text{M}$  HicBA was taken as 0%. The X axis indicates the concentration of added peptide. Error bars represent the standard deviation of three replicate reactions. **(C)** *In vivo* assay of HicA toxicity. Each curves of cells is represented as different colors and the data (OD<sub>600</sub>) is result of the average of triplicate, with standard deviations indicated by error bars. **(D)** Antimicrobial activities of mimicking peptide against various bacteria. Minimum inhibitory concentration was defined as the lowest peptide concentration ( $\mu\text{M}$ ) that completely inhibits the cell growth after 24 h of incubation at 37°C. The experiment was performed in duplicate.



## **2.4 Discussion**

### **2.4.1 Structural uniqueness of the HicBA complex**

The HicBA structure derived from *S. pneumoniae* is the first structure, showing complete conformation of HicBA TA system. Assembling mechanism of HicBA complex is two dimerization strategies of HicB via its N-terminus and C-terminus. Interface of HicBA was studied earlier from *Y. pestis* (127), but structural and functional characteristics of flexible DNA-binding domain of HicB are revealed by our study. Based on NMR assignments, it was confirmed that C-terminal DNA-binding motif of HicB is RHH (73). DNA-binding domain is corresponds to flexible moving domain, therefore, unveiling flexible nature of HicBA is meaningful to give supplementary explanation to many flexible-domain-lacking TA complexes (138,142). In addition, because intrinsically disordered toxin-neutralizing domain modulates the affinity between antitoxin and DNA, further study of relationship between protein flexibility and disorder would give crucial insights into reversibility of TA action including folding-upon binding (143)

### **2.4.2 Insights into the DNA binding mechanism of the HicB**

In the structural analysis, HicB from *S. pneumoniae* is composed of three domains: fixed domain, bending domain and moving domain. Bending domain is formed from flexible hinge from residues 107–112. The flexibility of substrate binding region of protein is significantly associated with the specificity of its substrate. Thus conformational flexibility of binding site largely influences DNA binding specificity (144). Based on our study, flexible nature of HicB would play a crucial

role in their regulatory dynamics toward its target DNA (145). As a transcription regulator, flexible form of HicB is essential for the bacterial cell life and death. These flexible domains undergo folding transition upon binding to toxins or DNA to exert important regulatory function. In other words, this intrinsic flexibility of HicB can offer functional advantages and makes HicB to bind its target easily (146,147).

Similarly, these stabilization-upon-binding logics might be another evidence for better binding affinity of HicBA-DNA than HicB-DNA. HicA contributes to binding affinity and structural stability of HicB and DNA thermodynamically (91,92). This mechanical process of binding between HicBA and DNA can be understood by analyzing their interaction in atomic level (Figure 36A–B). In our model, two antiparallel  $\beta$ -sheets binds to the major groove of the DNA and electrostatically positive portion of the two  $\alpha$ -helices anchor the DNA, facing the phosphates of the DNA backbone. These binding characteristics of HicBA-DNA interaction is mediated by stabilization-upon binding mechanism, which increases substrate specificity by undergoing conformation changes upon bindings of three binding partners, HicB, HicA and DNA (93,95).

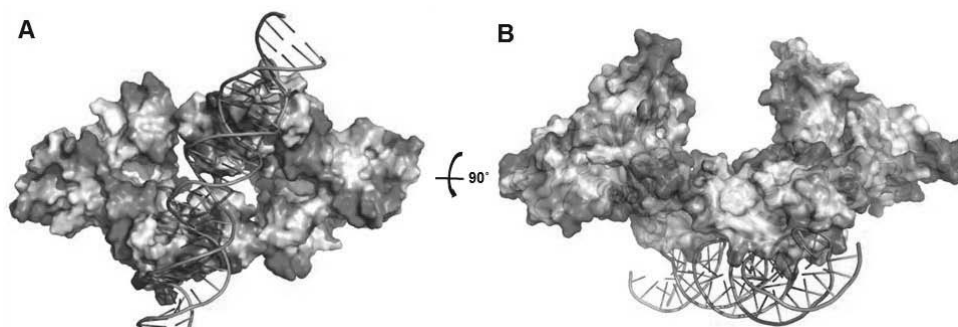


**Figure 36.** *In silico* docking model of the HicBA-DNA complex, showing the electrostatic potential surface. Multiple solutions were clustered automatically and resulted in the best single cluster of docking results: The best solution showed the score of  $-128.8 \pm 12.1$ , the smallest r.m.s. deviation ( $1.6 \text{ \AA} \pm 1.0 \text{ \AA}$ ), and the largest buried surface areas ( $2201.5 \pm 82.8 \text{ \AA}^2$ ). **(A)** Electrostatically positive portion of the two  $\alpha$ -helices anchor the DNA and **(B)** two antiparallel  $\beta$ -sheets binds to the major groove of the DNA.

#### 2.4.3 New opinions engaged in active site of HicA

The active sites of the toxins from VapBC or RelBE family are composed of three to four conserved residues or more residues (44,148). These residues, comprising active site are counteracted by binding of their cognate antitoxins. For HicBA family, however, there is only one conserved histidine in reported HicA toxins, which is likely to contribute to toxic activity of toxin (Figure 32A). Mutational study also confirmed that His36 is a critical source of its activity (Figure 32B). Furthermore, HicA toxins are smaller than MazF, RelE and VapC in their size and their active site do not form any charged pocket, cluster or cavity (132,149,150) (Figure 37). Conserved glycine and serine near the His36 might

support the structural integrity of the active site.

On the other hand, there are interesting structural discovery in mechanism of blocking the active site in *Y. pestis* (127) and *S. pneumonia* HicBA. In *S. pneumonia* HicBA, His36 is protruded in HicA, but inhibited by Thr33 and Glu47 of HicB. By this interaction, these three residues construct catalytic triad (151) (Figure 38). Catalytic triad consists of acid, base and nucleophile. This triad is also found in *Y. pestis* HicBA. The amino acids, taking charge of acid and base are same for two structures as glutamate and histidine but residue acting as a nucleophile is different as threonine and asparagine (152). Catalytic triad is usually located in the active site of protease (153), but Type II toxin HicA is ribonuclease and has His36 for its ribonucleic activity. So it is rationally suggested that the ribonucleic activity of HicA is inhibited by folding triad that cannot cut RNA, via binding with HicB. This is consistent with mutational study in HicB neutralization assay, showing HicA-HicB-E47A (HicBA complex having E47A mutation in HicB) re-generated toxicity of HicA to cells (Figure 33C). It is estimated that the role of acid is more important than variable nucleophiles because HicA-HicB-T33A did not show toxicity to cells.

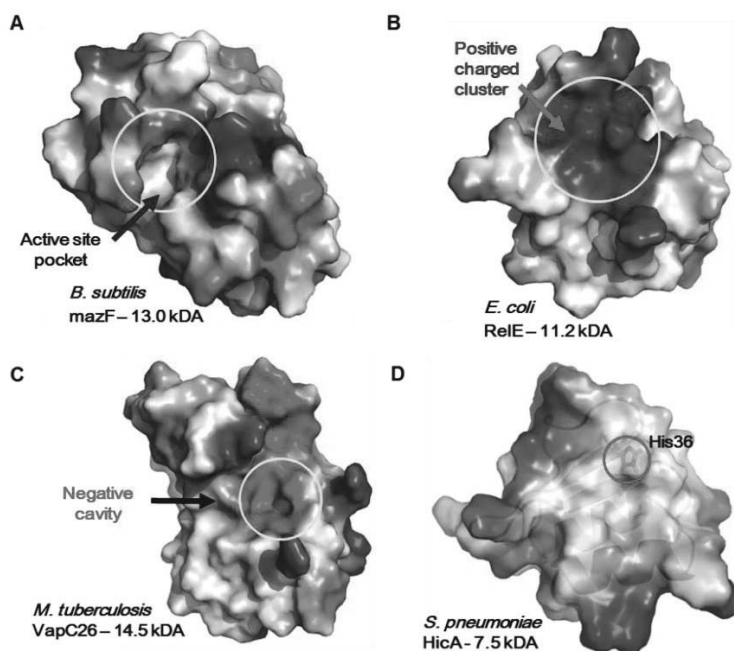


**Figure 37.** Surfaces of active sites of various toxins. **(A)** MazF (PDB code 4ME7) from *B. subtilis*. **(B)** RelE (PDB code 4FXI) from *E. coli*. **(C)** VapC26 (PDB code 5X3T) from *M. tuberculosis*. **(D)** HicA (PDB code 5YRZ) from *S. pneumoniae*.

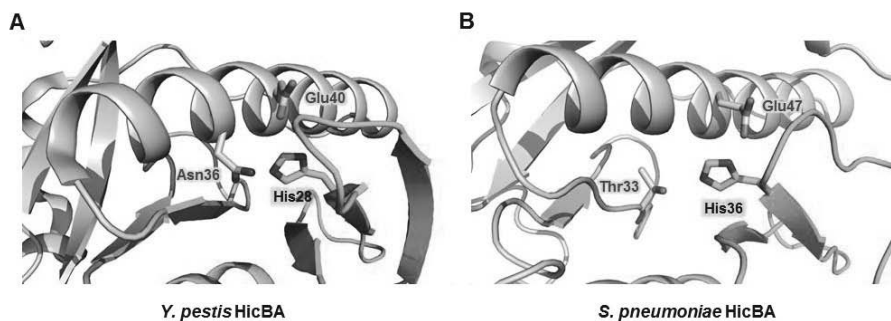


**Figure 38.** Catalytic triads of *Y. pestis* HicBA **(A)** and *S. pneumoniae* HicBA **(B)**. Catalytic triad consists of acid, base and nucleophile. The amino acids, taking charge of acid and base are same for two structures as glutamate and histidine but residue acting as a nucleophile is different as threonine and asparagine.

#### **2.4.4 Artificial activation of the HicA by mimicking peptide as an antibacterial strategy**

According to shown toxicity of HicA in our study (Figure 35C), our peptide inhibitors can be a new antimicrobial agent by liberating HicA from HicBA complex. HicBA interface mimetic peptides have greatest ability to inhibit the interaction between toxin and antitoxin independent on the concentration of peptide, compared with other TA complex mimetic peptides (40,109,132). Furthermore, MIC could also be obtained via antimicrobial activity test, despite the relative high value than other highly engineered antimicrobial peptides (139,154). Because antimicrobial activity was more effective at higher contents of  $\alpha$ -helix and better folding, (Figure 34C) we may be able to obtain a more optimized inhibitor by modifying the peptide by conjugation strategies and surface modulation, such as stapling the peptides via hydrocarbon cross linking to obtain better permeability and structural folding (112,115).

The expression of HicA protein in *E. coli* severely reduced translation rate (155) and expression level of HicA in *B. pseudomallei* was associated with modulation of the formation of persister cells (131). In conclusion, based on the experimental data obtained in this study, peptide inducing adequate activation of HicA may be a new structure based antimicrobial agent.

## 2.5 Conclusion

*S. pneumoniae* utilizes many toxin-antitoxin (TA) systems to survive. TA systems are strongly correlated with bacterial physiology, such as gene regulation, growth arrest, survival, and apoptosis. The HicBA TA family is one of the most valuable TA families. However, crystal structures have only been determined for the one incomplete HicBA TA complexes to date. The HicA toxin damages a host cell by inducing RNA degradation. The HicB antitoxin is an important cellular components for cell maintenance and viability because it neutralizes the detrimental activity of its cognate toxin. The HicB antitoxin acts as a repressors that auto-regulates the transcription of the TA operon. The HicA toxin exhibits ribonuclease activity toward cellular mRNAs.

In particular, we present the crystal structure of the HicBA complex from *S. pneumoniae* at a resolution of 2.30 Å. The structure revealed the important residues involved in binding to the promotor DNA and in the formation of the HicBA complex. The HicA toxin forms double-stranded RNA binding domain (dsRBD), and HicB adopts a ribbon-helix-helix (RHH) DNA-binding motif. The core residues in HicB that bind to DNA and the structural changes in HicB resulting from toxin binding were clarified by nuclear magnetic resonance (NMR). The catalytic site of HicA is composed of histidine residue and the ribonuclease activity of HicA was confirmed in this study. Several peptides were designed as antibiotic candidates to mimic the binding interface of the HicBA complex and thereby suppress the TA interaction. This approach may contribute to the development of novel, potent antibiotics that are effective treatments for antibiotic-resistant *S. pneumoniae*.

## References

1. Buts, L., Lah, J., Dao-Thi, M.H., Wyns, L. and Loris, R. (2005) Toxin-antitoxin modules as bacterial metabolic stress managers. *Trends in biochemical sciences*, **30**, 672-679.
2. Gerdes, K., Christensen, S.K. and Lobner-Olesen, A. (2005) Prokaryotic toxin-antitoxin stress response loci. *Nature reviews. Microbiology*, **3**, 371-382.
3. Van Melderren, L. (2010) Toxin-antitoxin systems: why so many, what for? *Current opinion in microbiology*, **13**, 781-785.
4. Hayes, F. and Van Melderren, L. (2011) Toxins-antitoxins: diversity, evolution and function. *Crit Rev Biochem Mol Biol*, **46**, 386-408.
5. Long, Q.X., He, Y. and Xie, J.P. (2012) [The molecular physiological and genetic mechanisms underlying the superb efficacy of quinolones]. *Yao Xue Xue Bao*, **47**, 969-977.
6. Ogura, T. and Hiraga, S. (1983) Mini-F plasmid genes that couple host cell division to plasmid proliferation. *Proc Natl Acad Sci U S A*, **80**, 4784-4788.
7. Magnuson, R.D. (2007) Hypothetical functions of toxin-antitoxin systems. *J Bacteriol*, **189**, 6089-6092.
8. Monti, M.C., Hernandez-Arriaga, A.M., Kamphuis, M.B., Lopez-Villarejo, J., Heck, A.J., Boelens, R., Diaz-Orejas, R. and van den Heuvel, R.H. (2007) Interactions of Kid-Kis toxin-antitoxin complexes with the parD operator-promoter region of plasmid R1 are piloted by the Kis antitoxin and tuned by the stoichiometry of Kid-Kis oligomers. *Nucleic Acids Res*, **35**, 1737-1749.
9. Hayes, F. (2003) Toxins-antitoxins: plasmid maintenance, programmed cell death, and cell cycle arrest. *Science*, **301**, 1496-1499.
10. Chan, W.T., Balsa, D. and Espinosa, M. (2015) One cannot rule them all: Are bacterial toxins-antitoxins druggable? *FEMS Microbiol Rev*, **39**, 522-540.



11. Wang, X. and Wood, T.K. (2011) Toxin-antitoxin systems influence biofilm and persister cell formation and the general stress response. *Appl Environ Microbiol*, **77**, 5577-5583.
12. Vazquez-Laslop, N., Lee, H. and Neyfakh, A.A. (2006) Increased persistence in *Escherichia coli* caused by controlled expression of toxins or other unrelated proteins. *J Bacteriol*, **188**, 3494-3497.
13. Korch, S.B. and Hill, T.M. (2006) Ectopic overexpression of wild-type and mutant *hipA* genes in *Escherichia coli*: effects on macromolecular synthesis and persister formation. *J Bacteriol*, **188**, 3826-3836.
14. Yamaguchi, Y., Park, J.H. and Inouye, M. (2011) Toxin-antitoxin systems in bacteria and archaea. *Annu Rev Genet*, **45**, 61-79.
15. Zhu, L., Zhang, Y., Teh, J.S., Zhang, J., Connell, N., Rubin, H. and Inouye, M. (2006) Characterization of mRNA interferases from *Mycobacterium tuberculosis*. *J Biol Chem*, **281**, 18638-18643.
16. Dao-Thi, M.H., Van Melderren, L., De Genst, E., Afif, H., Buts, L., Wyns, L. and Loris, R. (2005) Molecular basis of gyrase poisoning by the addiction toxin CcdB. *J Mol Biol*, **348**, 1091-1102.
17. Christensen, S.K. and Gerdes, K. (2003) RelE toxins from bacteria and Archaea cleave mRNAs on translating ribosomes, which are rescued by tmRNA. *Molecular microbiology*, **48**, 1389-1400.
18. Ramisetty, B.C. and Santhosh, R.S. (2016) Horizontal gene transfer of chromosomal Type II toxin-antitoxin systems of *Escherichia coli*. *FEMS Microbiol Lett*, **363**.
19. Fiedoruk, K., Daniluk, T., Swiecicka, I., Sciepuk, M. and Leszczynska, K. (2015) Type II toxin-antitoxin systems are unevenly distributed among *Escherichia coli* phylogroups. *Microbiology*, **161**, 158-167.

20. Aakre, C.D., Phung, T.N., Huang, D. and Laub, M.T. (2013) A bacterial toxin inhibits DNA replication elongation through a direct interaction with the beta sliding clamp. *Mol Cell*, **52**, 617-628.
21. Janssen, B.D., Garza-Sanchez, F. and Hayes, C.S. (2015) YoeB toxin is activated during thermal stress. *Microbiologyopen*, **4**, 682-697.
22. Kedzierska, B. and Hayes, F. (2016) Emerging Roles of Toxin-Antitoxin Modules in Bacterial Pathogenesis. *Molecules*, **21**.
23. Schuster, C.F. and Bertram, R. (2016) Toxin-Antitoxin Systems of Staphylococcus aureus. *Toxins (Basel)*, **8**.
24. Brzozowska, I. and Zielenkiewicz, U. (2013) Regulation of toxin-antitoxin systems by proteolysis. *Plasmid*, **70**, 33-41.
25. Nieto, C., Cherny, I., Khoo, S.K., de Lacoba, M.G., Chan, W.T., Yeo, C.C., Gazit, E. and Espinosa, M. (2007) The yefM-yoeB toxin-antitoxin systems of Escherichia coli and Streptococcus pneumoniae: functional and structural correlation. *Journal of bacteriology*, **189**, 1266-1278.
26. HersHKovitz, I., Donoghue, H.D., Minnikin, D.E., May, H., Lee, O.Y., Feldman, M., Galili, E., Spigelman, M., Rothschild, B.M. and Bar-Gal, G.K. (2015) Tuberculosis origin: The Neolithic scenario. *Tuberculosis (Edinb)*, **95 Suppl 1**, S122-126.
27. Fu, L.M. and Fu-Liu, C.S. (2002) Is Mycobacterium tuberculosis a closer relative to Gram-positive or Gram-negative bacterial pathogens? *Tuberculosis (Edinb)*, **82**, 85-90.
28. Pollock, C. (2012) Mycobacterial infection in the ferret. *Vet Clin North Am Exot Anim Pract*, **15**, 121-129, vii.
29. Lunn, J.A., Martin, P., Zaki, S. and Malik, R. (2005) Pneumonia due to Mycobacterium abscessus in two domestic ferrets (Mustelo putorius furo). *Australian Veterinary Journal*, **83**, 542-546.

30. Keri, R.S., Chand, K., Ramakrishnappa, T. and Nagaraja, B.M. (2015) Recent progress on pyrazole scaffold-based antimycobacterial agents. *Arch Pharm (Weinheim)*, **348**, 299-314.
31. Comolet, T. (2015) Multidrug-resistant tuberculosis: challenges of a global emergence. *Bull Soc Pathol Exot*, **108**, 290-298.
32. Pechalrieu, D. and Lopez, M. (2015) Compounds for use in the treatment of mycobacterial infections: a patent evaluation (WO2014049107A1). *Expert Opin Ther Pat*, **25**, 729-735.
33. Shao, Y., Harrison, E.M., Bi, D., Tai, C., He, X., Ou, H.Y., Rajakumar, K. and Deng, Z. (2011) TADB: a web-based resource for Type 2 toxin-antitoxin loci in bacteria and archaea. *Nucleic Acids Res*, **39**, D606-611.
34. Pandey, D.P. and Gerdes, K. (2005) Toxin-antitoxin loci are highly abundant in free-living but lost from host-associated prokaryotes. *Nucleic Acids Res*, **33**, 966-976.
35. Ramage, H.R., Connolly, L.E. and Cox, J.S. (2009) Comprehensive functional analysis of Mycobacterium tuberculosis toxin-antitoxin systems: implications for pathogenesis, stress responses, and evolution. *PLoS Genet*, **5**, e1000767.
36. Sala, A., Bordes, P. and Genevaux, P. (2014) Multiple toxin-antitoxin systems in Mycobacterium tuberculosis. *Toxins (Basel)*, **6**, 1002-1020.
37. Min, A.B., Miallau, L., Sawaya, M.R., Habel, J., Cascio, D. and Eisenberg, D. (2012) The crystal structure of the Rv0301-Rv0300 VapBC-3 toxin-antitoxin complex from M. tuberculosis reveals a Mg(2)(+) ion in the active site and a putative RNA-binding site. *Protein Sci*, **21**, 1754-1767.
38. Miallau, L., Faller, M., Chiang, J., Arbing, M., Guo, F., Cascio, D. and Eisenberg, D. (2009) Structure and proposed activity of a member of the VapBC family of toxin-antitoxin systems. VapBC-5 from Mycobacterium tuberculosis. *J Biol Chem*, **284**, 276-283.

39. Das, U., Pogenberg, V., Subhramanyam, U.K., Wilmanns, M., Gourinath, S. and Srinivasan, A. (2014) Crystal structure of the VapBC-15 complex from *Mycobacterium tuberculosis* reveals a two-metal ion dependent PIN-domain ribonuclease and a variable mode of toxin-antitoxin assembly. *J Struct Biol*, **188**, 249-258.
40. Lee, I.G., Lee, S.J., Chae, S., Lee, K.Y., Kim, J.H. and Lee, B.J. (2015) Structural and functional studies of the *Mycobacterium tuberculosis* VapBC30 toxin-antitoxin system: implications for the design of novel antimicrobial peptides. *Nucleic Acids Res*, **43**, 7624-7637.
41. Mate, M.J., Vincentelli, R., Foos, N., Raoult, D., Cambillau, C. and Ortiz-Lombardia, M. (2012) Crystal structure of the DNA-bound VapBC2 antitoxin/toxin pair from *Rickettsia felis*. *Nucleic Acids Res*, **40**, 3245-3258.
42. Dienemann, C., Boggild, A., Winther, K.S., Gerdes, K. and Brodersen, D.E. (2011) Crystal structure of the VapBC toxin-antitoxin complex from *Shigella flexneri* reveals a hetero-octameric DNA-binding assembly. *J Mol Biol*, **414**, 713-722.
43. Arcus, V.L., Rainey, P.B. and Turner, S.J. (2005) The PIN-domain toxin-antitoxin array in mycobacteria. *Trends Microbiol*, **13**, 360-365.
44. Arcus, V.L., McKenzie, J.L., Robson, J. and Cook, G.M. (2011) The PIN-domain ribonucleases and the prokaryotic VapBC toxin-antitoxin array. *Protein Eng Des Sel*, **24**, 33-40.
45. Winther, K.S. and Gerdes, K. (2011) Enteric virulence associated protein VapC inhibits translation by cleavage of initiator tRNA. *Proc Natl Acad Sci U S A*, **108**, 7403-7407.
46. Ahidjo, B.A., Kuhnert, D., McKenzie, J.L., Machowski, E.E., Gordhan, B.G., Arcus, V., Abrahams, G.L. and Mizrahi, V. (2011) VapC toxins from *Mycobacterium tuberculosis* are ribonucleases that differentially inhibit growth and are neutralized by cognate VapB antitoxins. *PLoS One*, **6**, e21738.

47. Winther, K.S., Brodersen, D.E., Brown, A.K. and Gerdes, K. (2013) VapC20 of *Mycobacterium tuberculosis* cleaves the sarcin-ricin loop of 23S rRNA. *Nat Commun*, **4**, 2796.
48. McKenzie, J.L., Duyvestyn, J.M., Smith, T., Bendak, K., Mackay, J., Cursons, R., Cook, G.M. and Arcus, V.L. (2012) Determination of ribonuclease sequence-specificity using Pentaprobates and mass spectrometry. *RNA*, **18**, 1267-1278.
49. Winther, K., Tree, J.J., Tollervey, D. and Gerdes, K. (2016) VapCs of *Mycobacterium tuberculosis* cleave RNAs essential for translation. *Nucleic Acids Res*, **44**, 9860-9871.
50. Shi, X., Khade, P.K., Sanbonmatsu, K.Y. and Joseph, S. (2012) Functional role of the sarcin-ricin loop of the 23S rRNA in the elongation cycle of protein synthesis. *J Mol Biol*, **419**, 125-138.
51. Goeders, N. and Van Melderren, L. (2014) Toxin-antitoxin systems as multilevel interaction systems. *Toxins (Basel)*, **6**, 304-324.
52. Bukowski, M., Rojowska, A. and Wladyka, B. (2011) Prokaryotic toxin-antitoxin systems--the role in bacterial physiology and application in molecular biology. *Acta Biochim Pol*, **58**, 1-9.
53. Lioy, V.S., Rey, O., Balsa, D., Pellicer, T. and Alonso, J.C. (2010) A toxin-antitoxin module as a target for antimicrobial development. *Plasmid*, **63**, 31-39.
54. Gao, Y.Z., Xu, H.H., Ju, T.T. and Zhao, X.H. (2013) The effect of limited proteolysis by different proteases on the formation of whey protein fibrils. *J Dairy Sci*, **96**, 7383-7392.
55. Otwinowski, Z. and Minor, W. (1997) Processing of X-ray diffraction data collected in oscillation mode. *Macromolecular Crystallography, Pt A*, **276**, 307-326.
56. Adams, P.D., Afonine, P.V., Bunkoczi, G., Chen, V.B., Davis, I.W., Echols, N., Headd, J.J., Hung, L.W., Kapral, G.J., Grosse-Kunstleve, R.W. *et al.* (2010)

- PHENIX: a comprehensive Python-based system for macromolecular structure solution. *Acta Crystallogr D Biol Crystallogr*, **66**, 213-221.
57. Emsley, P., Lohkamp, B., Scott, W.G. and Cowtan, K. (2010) Features and development of Coot. *Acta Crystallogr D Biol Crystallogr*, **66**, 486-501.
  58. Brunger, A.T. (1992) Free R value: a novel statistical quantity for assessing the accuracy of crystal structures. *Nature*, **355**, 472-475.
  59. Murshudov, G.N., Skubak, P., Lebedev, A.A., Pannu, N.S., Steiner, R.A., Nicholls, R.A., Winn, M.D., Long, F. and Vagin, A.A. (2011) REFMAC5 for the refinement of macromolecular crystal structures. *Acta Crystallogr D Biol Crystallogr*, **67**, 355-367.
  60. Chen, V.B., Arendall, W.B., 3rd, Headd, J.J., Keedy, D.A., Immormino, R.M., Kapral, G.J., Murray, L.W., Richardson, J.S. and Richardson, D.C. (2010) MolProbity: all-atom structure validation for macromolecular crystallography. *Acta Crystallogr D Biol Crystallogr*, **66**, 12-21.
  61. DeLano, W.L. and Lam, J.W. (2005) PyMOL: A communications tool for computational models. *Abstr Pap Am Chem S*, **230**, U1371-U1372.
  62. Baker, N.A., Sept, D., Joseph, S., Holst, M.J. and McCammon, J.A. (2001) Electrostatics of nanosystems: application to microtubules and the ribosome. *Proc Natl Acad Sci U S A*, **98**, 10037-10041.
  63. Klose, D.P., Wallace, B.A. and Janes, R.W. (2010) 2Struc: the secondary structure server. *Bioinformatics*, **26**, 2624-2625.
  64. Krissinel, E. and Henrick, K. (2007) Inference of macromolecular assemblies from crystalline state. *J Mol Biol*, **372**, 774-797.
  65. McWilliam, H., Li, W., Uludag, M., Squizzato, S., Park, Y.M., Buso, N., Cowley, A.P. and Lopez, R. (2013) Analysis Tool Web Services from the EMBL-EBI. *Nucleic Acids Res*, **41**, W597-600.

66. Robert, X. and Gouet, P. (2014) Deciphering key features in protein structures with the new ENDscript server. *Nucleic Acids Res*, **42**, W320-324.
67. Verma, S., Kumar, S., Gupta, V.P., Gourinath, S., Bhatnagar, S. and Bhatnagar, R. (2015) Structural basis of Bacillus anthracis MoxXT disruption and the modulation of MoxT ribonuclease activity by rationally designed peptides. *J Biomol Struct Dyn*, **33**, 606-624.
68. Delaglio, F., Grzesiek, S., Vuister, G.W., Zhu, G., Pfeifer, J. and Bax, A. (1995) NMRPipe: a multidimensional spectral processing system based on UNIX pipes. *J Biomol NMR*, **6**, 277-293.
69. Johnson, B.A. (2004) Using NMRView to visualize and analyze the NMR spectra of macromolecules. *Methods Mol Biol*, **278**, 313-352.
70. Holm, L. and Rosenstrom, P. (2010) Dali server: conservation mapping in 3D. *Nucleic Acids Res*, **38**, W545-549.
71. Mattison, K., Wilbur, J.S., So, M. and Brennan, R.G. (2006) Structure of FitAB from Neisseria gonorrhoeae bound to DNA reveals a tetramer of toxin-antitoxin heterodimers containing pin domains and ribbon-helix-helix motifs. *J Biol Chem*, **281**, 37942-37951.
72. Xiong, W., Li, T., Chen, K. and Tang, K. (2009) Local combinational variables: an approach used in DNA-binding helix-turn-helix motif prediction with sequence information. *Nucleic Acids Res*, **37**, 5632-5640.
73. Schreiter, E.R. and Drennan, C.L. (2007) Ribbon-helix-helix transcription factors: variations on a theme. *Nat Rev Microbiol*, **5**, 710-720.
74. Coles, M., Djuranovic, S., Soding, J., Frickey, T., Koretke, K., Truffault, V., Martin, J. and Lupas, A.N. (2005) AbrB-like transcription factors assume a swapped hairpin fold that is evolutionarily related to double-psi beta barrels. *Structure*, **13**, 919-928.

75. Kumar, P., Issac, B., Dodson, E.J., Turkenburg, J.P. and Mande, S.C. (2008) Crystal structure of Mycobacterium tuberculosis YefM antitoxin reveals that it is not an intrinsically unstructured protein. *J Mol Biol*, **383**, 482-493.
76. Gomis-Ruth, F.X., Sola, M., Acebo, P., Parraga, A., Guasch, A., Eritja, R., Gonzalez, A., Espinosa, M., del Solar, G. and Coll, M. (1998) The structure of plasmid-encoded transcriptional repressor CopG unliganded and bound to its operator. *EMBO J*, **17**, 7404-7415.
77. Setny, P., Baron, R. and McCammon, J.A. (2010) How Can Hydrophobic Association Be Enthalpy Driven? *Journal of Chemical Theory and Computation*, **6**, 2866-2871.
78. Shen, Y., Delaglio, F., Cornilescu, G. and Bax, A. (2009) TALOS+: a hybrid method for predicting protein backbone torsion angles from NMR chemical shifts. *J Biomol NMR*, **44**, 213-223.
79. de Paula, V.S., Razzera, G., Barreto-Bergter, E., Almeida, F.C. and Valente, A.P. (2011) Portrayal of complex dynamic properties of sugarcane defensin 5 by NMR: multiple motions associated with membrane interaction. *Structure*, **19**, 26-36.
80. Anjana, R., Vaishnavi, M.K., Sherlin, D., Kumar, S.P., Naveen, K., Kanth, P.S. and Sekar, K. (2012) Aromatic-aromatic interactions in structures of proteins and protein-DNA complexes: a study based on orientation and distance. *Bioinformation*, **8**, 1220-1224.
81. Meyer, E.A., Castellano, R.K. and Diederich, F. (2003) Interactions with aromatic rings in chemical and biological recognition. *Angewandte Chemie-International Edition*, **42**, 1210-1250.
82. Chou, P.Y. and Fasman, G.D. (1974) Conformational parameters for amino acids in helical, beta-sheet, and random coil regions calculated from proteins. *Biochemistry*, **13**, 211-222.



83. Chou, P.Y. and Fasman, G.D. (1977) Secondary Structural Prediction of Proteins from Their Amino-Acid Sequence. *Trends in Biochemical Sciences*, **2**, 128-131.
84. Eisenhaber, F., Persson, B. and Argos, P. (1995) Protein-Structure Prediction - Recognition of Primary, Secondary, and Tertiary Structural Features from Amino-Acid-Sequence. *Critical Reviews in Biochemistry and Molecular Biology*, **30**, 1-94.
85. Malkov, S.N., Zivkovic, M.V., Beljanski, M.V., Stojanovic, S.D. and Zaric, S.D. (2009) A Reexamination of Correlations of Amino Acids with Particular Secondary Structures. *Protein Journal*, **28**, 74-86.
86. Serrano, L., Bycroft, M. and Fersht, A.R. (1991) Aromatic-aromatic interactions and protein stability. Investigation by double-mutant cycles. *J Mol Biol*, **218**, 465-475.
87. Hamilton, B., Manzella, A., Schmidt, K., DiMarco, V. and Butler, J.S. (2014) Analysis of non-typeable Haemophilus influenzae VapC1 mutations reveals structural features required for toxicity and flexibility in the active site. *PLoS One*, **9**, e112921.
88. Christensen, S.K., Maenhaut-Michel, G., Mine, N., Gottesman, S., Gerdes, K. and Van Melderen, L. (2004) Overproduction of the Lon protease triggers inhibition of translation in Escherichia coli: involvement of the yefM-yoeB toxin-antitoxin system. *Mol Microbiol*, **51**, 1705-1717.
89. Kim do, H., Im, H., Jee, J.G., Jang, S.B., Yoon, H.J., Kwon, A.R., Kang, S.M. and Lee, B.J. (2014) beta-Arm flexibility of HU from Staphylococcus aureus dictates the DNA-binding and recognition mechanism. *Acta Crystallogr D Biol Crystallogr*, **70**, 3273-3289.
90. Black, D.S., Kelly, A.J., Mardis, M.J. and Moyed, H.S. (1991) Structure and Organization of Hip, an Operon That Affects Lethality Due to Inhibition of Peptidoglycan or DNA-Synthesis. *Journal of Bacteriology*, **173**, 5732-5739.

91. Marianovsky, I., Aizenman, E., Engelberg-Kulka, H. and Glaser, G. (2001) The regulation of the *Escherichia coli* mazEF promoter involves an unusual alternating palindrome. *J Biol Chem*, **276**, 5975-5984.
92. Ahmad, S., Keskin, O., Sarai, A. and Nussinov, R. (2008) Protein-DNA interactions: structural, thermodynamic and clustering patterns of conserved residues in DNA-binding proteins. *Nucleic Acids Res*, **36**, 5922-5932.
93. Andrabi, M., Mizuguchi, K. and Ahmad, S. (2014) Conformational changes in DNA-binding proteins: relationships with precomplex features and contributions to specificity and stability. *Proteins*, **82**, 841-857.
94. Petty, T.J., Emamzadah, S., Costantino, L., Petkova, I., Stavridi, E.S., Saven, J.G., Vauthey, E. and Halazonetis, T.D. (2011) An induced fit mechanism regulates p53 DNA binding kinetics to confer sequence specificity. *EMBO J*, **30**, 2167-2176.
95. Spolar, R.S. and Record, M.T., Jr. (1994) Coupling of local folding to site-specific binding of proteins to DNA. *Science*, **263**, 777-784.
96. Johnson, E.P., Strom, A.R. and Helinski, D.R. (1996) Plasmid RK2 toxin protein ParE: Purification and interaction with the ParD antitoxin protein. *Journal of Bacteriology*, **178**, 1420-1429.
97. Afif, H., Allali, N., Couturier, M. and Van Melder, L. (2001) The ratio between CcdA and CcdB modulates the transcriptional repression of the ccd poison-antidote system. *Molecular Microbiology*, **41**, 73-82.
98. Nowotny, M. and Yang, W. (2006) Stepwise analyses of metal ions in RNase H catalysis from substrate destabilization to product release. *EMBO J*, **25**, 1924-1933.
99. Nowotny, M., Gaidamakov, S.A., Crouch, R.J. and Yang, W. (2005) Crystal structures of RNase H bound to an RNA/DNA hybrid: substrate specificity and metal-dependent catalysis. *Cell*, **121**, 1005-1016.
100. Zhao, H., Lin, Z., Lynn, A.Y., Varnado, B., Beutler, J.A., Murelli, R.P., Le Grice, S.F. and Tang, L. (2015) Two distinct modes of metal ion binding in the nuclease

- active site of a viral DNA-packaging terminase: insight into the two-metal-ion catalytic mechanism. *Nucleic Acids Res*, **43**, 11003-11016.
101. Xu, K., Dedic, E., Cob-Cantal, P., Dienemann, C., Boggild, A., Winther, K.S., Gerdes, K. and Brodersen, D.E. (2013) Protein expression, crystallization and preliminary X-ray crystallographic analysis of the isolated *Shigella flexneri* VapC toxin. *Acta Crystallogr Sect F Struct Biol Cryst Commun*, **69**, 762-765.
  102. Cruz, J.W., Sharp, J.D., Hoffer, E.D., Maehigashi, T., Vvedenskaya, I.O., Konkimalla, A., Husson, R.N., Nickels, B.E., Dunham, C.M. and Woychik, N.A. (2015) Growth-regulating *Mycobacterium tuberculosis* VapC-mt4 toxin is an isoacceptor-specific tRNase. *Nat Commun*, **6**, 7480.
  103. Hwang, K.Y., Baek, K., Kim, H.Y. and Cho, Y. (1998) The crystal structure of flap endonuclease-1 from *Methanococcus jannaschii*. *Nat Struct Biol*, **5**, 707-713.
  104. Garcia-Ortega, L., Masip, M., Mancheno, J.M., Onaderra, M., Lizarbe, M.A., Garcia-Mayoral, M.F., Bruix, M., Martinez del Pozo, A. and Gavilanes, J.G. (2002) Deletion of the NH<sub>2</sub>-terminal beta-hairpin of the ribotoxin alpha-sarcin produces a nontoxic but active ribonuclease. *J Biol Chem*, **277**, 18632-18639.
  105. Lopes, A.P., Lopes, L.M., Fraga, T.R., Chura-Chambi, R.M., Sanson, A.L., Cheng, E., Nakajima, E., Morganti, L. and Martins, E.A. (2014) VapC from the leptospiral VapBC toxin-antitoxin module displays ribonuclease activity on the initiator tRNA. *PLoS One*, **9**, e101678.
  106. Zaychikova, M.V., Zakharevich, N.V., Sagaidak, M.O., Bogolubova, N.A., Smirnova, T.G., Andreevskaya, S.N., Larionova, E.E., Alekseeva, M.G., Chernousova, L.N. and Danilenko, V.N. (2015) *Mycobacterium tuberculosis* Type II Toxin-Antitoxin Systems: Genetic Polymorphisms and Functional Properties and the Possibility of Their Use for Genotyping. *PLoS One*, **10**, e0143682.

107. Demidenok, O.I., Kaprelyants, A.S. and Goncharenko, A.V. (2014) Toxin-antitoxin vapBC locus participates in formation of the dormant state in *Mycobacterium smegmatis*. *FEMS Microbiol Lett*, **352**, 69-77.
108. Agarwal, S., Mishra, N.K., Bhatnagar, S. and Bhatnagar, R. (2010) PemK Toxin of *Bacillus anthracis* Is a Ribonuclease AN INSIGHT INTO ITS ACTIVE SITE, STRUCTURE, AND FUNCTION. *Journal of Biological Chemistry*, **285**, 7254-7270.
109. Chopra, N., Agarwal, S., Verma, S., Bhatnagar, S. and Bhatnagar, R. (2011) Modeling of the structure and interactions of the *B. anthracis* antitoxin, MoxX: deletion mutant studies highlight its modular structure and repressor function. *J Comput Aided Mol Des*, **25**, 275-291.
110. Williams, J.J. and Hergenrother, P.J. (2012) Artificial activation of toxin-antitoxin systems as an antibacterial strategy. *Trends Microbiol*, **20**, 291-298.
111. Labbe, C.M., Laconde, G., Kuenemann, M.A., Villoutreix, B.O. and Sperandio, O. (2013) iPPI-DB: a manually curated and interactive database of small non-peptide inhibitors of protein-protein interactions. *Drug Discov Today*, **18**, 958-968.
112. Kim, Y.W., Grossmann, T.N. and Verdine, G.L. (2011) Synthesis of all-hydrocarbon stapled alpha-helical peptides by ring-closing olefin metathesis. *Nat Protoc*, **6**, 761-771.
113. Wagstaff, K.M. and Jans, D.A. (2006) Protein transduction: cell penetrating peptides and their therapeutic applications. *Curr Med Chem*, **13**, 1371-1387.
114. Zorko, M. and Langel, U. (2005) Cell-penetrating peptides: mechanism and kinetics of cargo delivery. *Adv Drug Deliv Rev*, **57**, 529-545.
115. Reinhardt, A. and Neundorff, I. (2016) Design and Application of Antimicrobial Peptide Conjugates. *Int J Mol Sci*, **17**.

116. Zaman, M., Ahmad, E., Qadeer, A., Rabbani, G. and Khan, R.H. (2014) Nanoparticles in relation to peptide and protein aggregation. *Int J Nanomedicine*, **9**, 899-912.
117. Jacobs, M.R. (2004) Streptococcus pneumoniae: epidemiology and patterns of resistance. *Am J Med*, **117 Suppl 3A**, 3S-15S.
118. Kaplan, S.L. (1995) The emergence of resistant pneumococcus as a pathogen in childhood upper respiratory tract infections. *Semin Respir Infect*, **10**, 31-36.
119. Ge, M., Chen, Z., Onishi, H.R., Kohler, J., Silver, L.L., Kerns, R., Fukuzawa, S., Thompson, C. and Kahne, D. (1999) Vancomycin derivatives that inhibit peptidoglycan biosynthesis without binding D-Ala-D-Ala. *Science*, **284**, 507-511.
120. Chambers, H.F. (1999) Penicillin-binding protein-mediated resistance in pneumococci and staphylococci. *J Infect Dis*, **179 Suppl 2**, S353-359.
121. Croucher, N.J., Chewapreecha, C., Hanage, W.P., Harris, S.R., McGee, L., van der Linden, M., Song, J.H., Ko, K.S., de Lencastre, H., Turner, C. *et al.* (2014) Evidence for soft selective sweeps in the evolution of pneumococcal multidrug resistance and vaccine escape. *Genome Biol Evol*, **6**, 1589-1602.
122. Dagan, R. (2009) Impact of pneumococcal conjugate vaccine on infections caused by antibiotic-resistant Streptococcus pneumoniae. *Clin Microbiol Infect*, **15 Suppl 3**, 16-20.
123. Rivera, A.M. and Boucher, H.W. (2011) Current concepts in antimicrobial therapy against select gram-positive organisms: methicillin-resistant Staphylococcus aureus, penicillin-resistant pneumococci, and vancomycin-resistant enterococci. *Mayo Clin Proc*, **86**, 1230-1243.
124. Fernandes, P. (2006) Antibacterial discovery and development--the failure of success? *Nat Biotechnol*, **24**, 1497-1503.
125. Spiegel, C.A. (1988) Laboratory detection of high-level aminoglycoside-aminocyclitol resistance in Enterococcus spp. *J Clin Microbiol*, **26**, 2270-2274.

126. Bliziotis, I.A., Samonis, G., Vardakas, K.Z., Chrysanthopoulou, S. and Falagas, M.E. (2005) Effect of aminoglycoside and beta-lactam combination therapy versus beta-lactam monotherapy on the emergence of antimicrobial resistance: a meta-analysis of randomized, controlled trials. *Clin Infect Dis*, **41**, 149-158.
127. Bibi-Triki, S., Li de la Sierra-Gallay, I., Lazar, N., Leroy, A., Van Tilbeurgh, H., Sebbane, F. and Pradel, E. (2014) Functional and structural analysis of HicA3-HicB3, a novel toxin-antitoxin system of *Yersinia pestis*. *J Bacteriol*, **196**, 3712-3723.
128. Makarova, K.S., Grishin, N.V. and Koonin, E.V. (2006) The HicAB cassette, a putative novel, RNA-targeting toxin-antitoxin system in archaea and bacteria. *Bioinformatics*, **22**, 2581-2584.
129. Masliah, G., Barraud, P. and Allain, F.H. (2013) RNA recognition by double-stranded RNA binding domains: a matter of shape and sequence. *Cell Mol Life Sci*, **70**, 1875-1895.
130. Unterholzner, S.J., Poppenberger, B. and Rozhon, W. (2013) Toxin-antitoxin systems: Biology, identification, and application. *Mob Genet Elements*, **3**, e26219.
131. Butt, A., Higman, V.A., Williams, C., Crump, M.P., Hemsley, C.M., Harmer, N. and Titball, R.W. (2014) The HicA toxin from *Burkholderia pseudomallei* has a role in persister cell formation. *Biochem J*, **459**, 333-344.
132. Kang, S.M., Kim, D.H., Lee, K.Y., Park, S.J., Yoon, H.J., Lee, S.J., Im, H. and Lee, B.J. (2017) Functional details of the *Mycobacterium tuberculosis* VapBC26 toxin-antitoxin system based on a structural study: insights into unique binding and antibiotic peptides. *Nucleic Acids Res*, **45**, 8564-8580.
133. Delano, W.L. (2002) The PyMOL Molecular Graphics System., DeLano Scientific, San Carlos, CA.

134. Dominguez, C., Boelens, R. and Bonvin, A.M. (2003) HADDOCK: a protein-protein docking approach based on biochemical or biophysical information. *J Am Chem Soc*, **125**, 1731-1737.
135. van Dijk, M. and Bonvin, A.M. (2009) 3D-DART: a DNA structure modelling server. *Nucleic Acids Res*, **37**, W235-239.
136. Lee, R.A., Razaz, M. and Hayward, S. (2003) The DynDom database of protein domain motions. *Bioinformatics*, **19**, 1290-1291.
137. Kim, D.H., Kang, S.J., Lee, K.Y., Jang, S.B., Kang, S.M. and Lee, B.J. (2017) Structure and dynamics study of translation initiation factor 1 from *Staphylococcus aureus* suggests its RNA binding mode. *Biochim Biophys Acta*, **1865**, 65-75.
138. Park, S.J., Son, W.S. and Lee, B.J. (2013) Structural overview of toxin-antitoxin systems in infectious bacteria: a target for developing antimicrobial agents. *Biochim Biophys Acta*, **1834**, 1155-1167.
139. Pham, T.K., Kim, D.H., Lee, B.J. and Kim, Y.W. (2013) Truncated and constrained helical analogs of antimicrobial esculentin-2EM. *Bioorg Med Chem Lett*, **23**, 6717-6720.
140. Uggerhoj, L.E., Poulsen, T.J., Munk, J.K., Fredborg, M., Sondergaard, T.E., Frimodt-Moller, N., Hansen, P.R. and Wimmer, R. (2015) Rational design of alpha-helical antimicrobial peptides: do's and don'ts. *Chembiochem*, **16**, 242-253.
141. Chen, Y.H., Yang, J.T. and Martinez, H.M. (1972) Determination of the secondary structures of proteins by circular dichroism and optical rotatory dispersion. *Biochemistry*, **11**, 4120-4131.
142. Lee, K.Y. and Lee, B.J. (2016) Structure, Biology, and Therapeutic Application of Toxin-Antitoxin Systems in Pathogenic Bacteria. *Toxins (Basel)*, **8**.
143. Loris, R. and Garcia-Pino, A. (2014) Disorder- and dynamics-based regulatory mechanisms in toxin-antitoxin modules. *Chem Rev*, **114**, 6933-6947.

144. Luscombe, N.M., Laskowski, R.A. and Thornton, J.M. (2001) Amino acid-base interactions: a three-dimensional analysis of protein-DNA interactions at an atomic level. *Nucleic Acids Res*, **29**, 2860-2874.
145. Dey, D., Nagaraja, V. and Ramakumar, S. (2017) Structural and evolutionary analyses reveal determinants of DNA binding specificities of nucleoid-associated proteins HU and IHF. *Mol Phylogenet Evol*, **107**, 356-366.
146. Cherny, I. and Gazit, E. (2004) The YefM antitoxin defines a family of natively unfolded proteins: implications as a novel antibacterial target. *J Biol Chem*, **279**, 8252-8261.
147. Lah, J., Simic, M., Vesnaver, G., Marianovsky, I., Glaser, G., Engelberg-Kulka, H. and Loris, R. (2005) Energetics of structural transitions of the addiction antitoxin MazE: is a programmed bacterial cell death dependent on the intrinsically flexible nature of the antitoxins? *J Biol Chem*, **280**, 17397-17407.
148. Kamphuis, M.B., Monti, M.C., van den Heuvel, R.H., Lopez-Villarejo, J., Diaz-Orejas, R. and Boelens, R. (2007) Structure and function of bacterial kid-kis and related toxin-antitoxin systems. *Protein Pept Lett*, **14**, 113-124.
149. Simanshu, D.K., Yamaguchi, Y., Park, J.H., Inouye, M. and Patel, D.J. (2013) Structural basis of mRNA recognition and cleavage by toxin MazF and its regulation by antitoxin MazE in *Bacillus subtilis*. *Mol Cell*, **52**, 447-458.
150. Boggild, A., Sofos, N., Andersen, K.R., Feddersen, A., Easter, A.D., Passmore, L.A. and Brodersen, D.E. (2012) The crystal structure of the intact *E. coli* RelBE toxin-antitoxin complex provides the structural basis for conditional cooperativity. *Structure*, **20**, 1641-1648.
151. Dodson, G. and Wlodawer, A. (1998) Catalytic triads and their relatives. *Trends in biochemical sciences*, **23**, 347-352.



152. Buller, A.R. and Townsend, C.A. (2013) Intrinsic evolutionary constraints on protease structure, enzyme acylation, and the identity of the catalytic triad. *Proc Natl Acad Sci U S A*, **110**, E653-661.
153. Ekici, O.D., Paetzel, M. and Dalbey, R.E. (2008) Unconventional serine proteases: variations on the catalytic Ser/His/Asp triad configuration. *Protein Sci*, **17**, 2023-2037.
154. Dinh, T.T., Kim, D.H., Luong, H.X., Lee, B.J. and Kim, Y.W. (2015) Antimicrobial activity of doubly-stapled alanine/lysine-based peptides. *Bioorg Med Chem Lett*, **25**, 4016-4019.
155. Jorgensen, M.G., Pandey, D.P., Jaskolska, M. and Gerdes, K. (2009) HicA of *Escherichia coli* defines a novel family of translation-independent mRNA interferases in bacteria and archaea. *J Bacteriol*, **191**, 1191-1199.

## 국문초록

독소-항독소 (TA) 시스템은 스트레스가 많은 환경에서 박테리아의 생존에 필수적이다. 특히, 결핵균은 안정한 VapC 독소 및 불안정한 VapB 항독소를 코딩하는 VapBC TA 유전자를 발현한다. 정상 조건 하에서, 이들 단백질은 상호 작용하여 비 독성 TA 복합체를 형성하지만, 독소는 나쁜 조건에서는 항독소로부터의 방출에 의해 활성화된다. 우리는 *Mycobacterium tuberculosis* VapBC26의 결정 구조를 제시하고 VapC26 독소가 리보뉴클레아제 활성화에 필수적인 PIN 도메인을 포함하는 것을 보였다. VapB26 항독소로서 N 말단의 리본-헬릭스-헬릭스 (RHH) DNA 결합 모티프를 가진다. VapC26의 활성 부위는 VapB26의 유연한 C-말단 영역에 의해 입체적으로 차단된다. VapB26의 C-말단 영역은 이차구조를 형성하지 않지만 VapC26에 결합 시 나선을 형성한다. RNase 활성 분석의 결과는  $Mg^{2+}$  및  $Mn^{2+}$ 가 VapC26의 리보뉴클레아제 활성화에 필수적임을 나타낸다. 핵자기공명 (NMR) 스펙트럼에 나타난 바와 같이, VapB26의 몇몇 잔기는 VapBC26 오페론의 프로모터 영역에 대한 특이적 결합에 관여한다. 또한, TA 복합체 형성을 억제하여 독소 활성을 증가시키는 독소 모방 펩타이드가 설계되어 새로운 항생제의 개발에 대한 새로운 접근법을 제공한다.

염증성 폐 질환인 폐렴은 *Streptococcus pneumoniae*에 의해 유발되며, 기존의 항생제에 대한 내성으로 인해 주목을 받고 있다. *S. pneumoniae*

TIGR4는 영양 부족, 항생제 치료와 같은 스트레스 조건에 대한 박테리아 지속성에 필수적인 6 종의 독소 - 항독소 쌍을 함유하고 있다. 특히, *S. pneumoniae*는 안정한 HicA 독소 및 불안정한 HicB 항 독소를 암호화하는 HicBA TA 유전자를 발현한다. 이러한 단백질은 정상적인 조건에서 비 독성 TA 복합체를 형성하기 위해 상호 작용하지만 바람직하지 않은 성장 조건에 대한 반응으로 항독소의 방출로 독소가 활성화된다. 우리는 HicA 독소가 RNA 인식에 필수적인 이중 가닥 RNA 결합 도메인 (dsRBD)를 함유하고 있음을 밝히면서 *S. pneumoniae*의 HicBA 복합체의 전체 형태를 보여주는 첫 번째 결정 구조를 제시한다. HicB 항독소는 C-말단에 리본-헬릭스-헬릭스 (RHH) DNA 결합 모티프를 가지고 HicA의 활성 부위는 HicB의 N-말단 부위에 의해 입체적으로 차단된다. RNase 활성 분석에 따르면 His36은 HicA의 리보뉴클레아 제 활성화에 필수적이다. 핵 자기 공명 (NMR) 스펙트럼에 나타난 바와 같이, HicB의 몇몇 잔기는 HicBA 오페론의 프로모터 DNA에 특이적인 결합에 관여한다. 또한, 독소 모방 펩타이드는 TA 복합체 형성을 억제하여 독소 활성을 증가 시키도록 설계되어 새로운 항생제 개발을 위한 새로운 접근법을 제공한다.

.....

주요어: toxin-antitoxin system, VapBC, HicBA, NMR, X-ray crystallography

학 번: 2012-21557